Simulation Study of CO2-Reactive Aprotic Heterocyclic Anion Ionic Liquids: Water Interactions, Liquid Structure, and CO2 Solubility

Quintin Ross Sheridan

Publication Date

18-04-2017

SIMULATION STUDY OF CO_2-REACTIVE APROTIC HETEROCYCLIC ANION IONIC LIQUIDS: WATER INTERACTIONS, LIQUID STRUCTURE, AND CO_2 SOLUBILITY

A Dissertation

Submitted to the Graduate School
of the University of Notre Dame
in Partial Fulfillment of the Requirements
for the Degree of

Doctor of Philosophy

by

Quintin Ross Sheridan

Edward J. Maginn, Co-Director

William F. Schneider, Co-Director

Graduate Program in Chemical and Biomolecular Engineering
Notre Dame, Indiana

April 2017

SIMULATION STUDY OF CO_2-REACTIVE APROTIC HETEROCYCLIC ANION IONIC LIQUIDS: WATER INTERACTIONS, LIQUID STRUCTURE, AND CO_2 SOLUBILITY

Abstract

by

Quintin Ross Sheridan

Aprotic heterocyclic anion (AHA) ionic liquids (ILs) that are capable of chemically binding CO_2 have gained increased interest from the scientific community in recent years as solvents that might be able to outperform current amine technologies in CO_2 separations. These ILs are of particular research interest due to the fact that the physical and chemical properties of the ILs can be tuned through proper pairing of cations and anions. This ability to tune the physical and chemical properties of the ILs simultaneously through functionalization of the ions presents both a great opportunity and a difficult challenge to design optimal ILs for CO_2 separations. ILs have a very large design space, and as such, it is extremely difficult to predict how changes in ionic structure will affect the liquid properties. Furthermore it is a difficult and time consuming process to synthesize a newly proposed IL.

Molecular simulations provide a convenient platform whereby IL properties can be investigated and understood in terms of molecular interactions. Classical molecular dynamics (CMD) are aptly suited to study liquid structure and to relate it to calculated bulk transport properties. This analysis lends itself to experimental design by providing an understanding of the origins of liquid properties. Likewise, quantum chemical calculations provide an efficient means to assess chemical reactivity.

The focus of this dissertation is to explore how CMD simulations and *ab initio* calculations can be used to further the current understanding of AHA IL systems. The dissertation starts with a review of the development of CO_2-reactive ILs and the role that simulations played in advancing their design. CMD simulations are used to examine the liquid structure and dynamics of both pure ILs and IL-water mixtures. The water solubility and the observed changes in dynamics from the addition of water are explained through structural analysis of hydrogen bonds formed between water and the anions. The liquid structure is examined through comparison of measured and computed structure functions for a series of ILs with different combinations of cations and anions. The fact that the liquid structure functions do not change appreciably upon reaction with CO_2 is used to explain why viscosities of AHA ILs do not change much upon reaction with CO_2. A method is presented for calculating CO_2 solubilities in AHA ILs using the Gibbs free energy of reaction. The method is able to predict isotherms with the characteristic shapes of experimental isotherms, but the predicted isotherms are highly sensitive to the calculated model parameters. The methods used in this dissertation provide a means to compare different ILs within the same family, and to select ILs with promising properties prior to synthesis.

To my parents, Michael P. Sheridan and Hallie J. Sheridan

CONTENTS

FIGURES

TABLES

ACKNOWLEDGMENTS

At a young age, my parents pushed me to excel in science and mathematics topics. My grandfather, Frank Frandsen, played a special role in my education by teaching me trigonometry and helping me to advance beyond the basic material taught in junior high. During the summer, he would drive me to Denver University to attend an extracurricular geology course which sparked my interest in science. Without the time and effort of my family members, I probably never would have taken advanced courses in high school, and continued to engineering school.

My mother always wanted me to have the best education possible, and she convinced me to join the International Baccalaureate program offered at Lakewood High School. The top notch education I received there made the transition to engineering school seem like things were getting easier, when most students had the opposite experience their freshman year. The many great teachers I had in high school transformed me into a well rounded individual. Not only did I get prepared for college science and mathematics courses, but I learned to take an objective approach to viewing the information presented to me, and to question what I truly know. My chemistry, physics, and mathematics teachers played an important role to develop my skills as a scientist and engineer. I am especially grateful to my high school chemistry teachers, Ms. Holloway and Mrs. Mclung, as well as my high school physics teacher Mr. Moore. The material I learned in their high school courses still helps me today in my PhD studies. Additionally, my high school calculus teacher, Mr. Gabaldon, helped me learn to always do my best and continue to push myself. He would tell us time and time again that to get a PhD, you needed to understand what it stood for:

Pride, Heart, and Desire.

After graduating from high school, I decided to follow in my fathers footsteps and study engineering at the Colorado School of Mines. Once again, I received a world-class education from some of the smartest and kindest individuals I have ever met. I am particularly grateful to Professor Rachel Morrish, whose passion for teaching made me want to get a PhD, and to Professor Thomas Furtak and Professor Reuben Collins, for teaching me the process of conducting scientific research during my senior design project. I feel that I was fortunate to have some of the best teachers ever, so many that I can not name them each individually, and that their preparation gave me the confidence to apply to graduate school for a PhD in chemical engineering.

My friends and family here at Notre Dame have provided endless encouragement when times were tough. Anytime I needed help understanding complex material, my labmates were willing to take time out of their days to discuss my issues and help me resolve them. I have received excellent guidance from the postdocs who mentored me, Taebum Lee and Ryan Mullen, and I am thankful for all of the research advice they offered me. Discussions with Dr. Samuel Seo were extremely useful in understanding the behavior of ionic liquids and helped guide my research efforts. I am thankful to both of my advisors, Professor Edward J. Maginn and Professor William F. Schneider, for their excellent research guidance and for all of the opportunities that they provided. I am especially grateful for the support of my girlfriend, Christina Horr. During the ups and downs of research, she was always there to encourage me not to give up and to work hard even when things didn't go the way I planned. I can not imagine my journey through the PhD program without her.

I would like to acknowledge the funding agencies that sponsered my research, the Air Force Office of Scientific Research under AFOSR Award No. FA9550-14-1-0306 and the Stanford Global Climate and Energy Program under Award No. 106644-A. I would also like to thank the Notre Dame Center for Research Computing for

providing computing resources.

All men are shaped by the people around them, and I am fortunate to have had so many great people in my life to help me become the man I am today.

CHAPTER 1

INTRODUCTION

In recent decades, the scientific community has identified CO_2 emissions as a significant contribution to anthropogenic global warming. If CO_2 emissions continue uncurbed at current rates, it could have adverse effects on global climate. Climate change has several negative externalities including negative economic effects, health effects, and the displacement of millions of people from coastal cities. It is therefore necessary to implement new technologies to mitigate CO_2 emissions.

One promising option to reduce CO_2 emissions is to perform post combustion CO_2 capture at point source emitters such as coal fired power plants. However, the current amine technology that can be implemented in industrial scale stripper absorber columns is too energy intensive for economical CO_2 capture. Amine CO_2 separations are not only energy intensive, but the amine solutions are also corrosive and volatile. It is therefore necessary to design new and improved processes for CO_2 capture in order to reduce the economic burden.

Ionic liquids (ILs) have been identified as solvents that may be able to outperform current amine technologies in CO_2 capture. They have several unique properties such as low volatility, high thermostability, and chemical tunability that may enable them to outperform amines. Recently, a class of aprotic heterocyclic anion (AHA) ILs was designed to absorb CO_2 through chemical bonding with the anions, thereby significantly increasing the CO_2 solubility. These ILs are of particular interest because both the physical and chemical properties of AHA ILs can be tuned by modifying the ion functional groups. The ability to tune the properties presents both an opportunity

and a challenge in designing ILs. The large design space of pairing different ions makes it difficult to identify optimal ILs for a given process. Computer simulations provide a convenient platform to assess IL properties and to provide an understanding of the molecular origin of observed properties. The goal of this dissertation is to use computational chemistry to improve the current understanding of AHA ILs.

In the second chapter of this thesis, a review is presented discussing the historical development of CO_2-reactive ILs. This chapter highlights the role that molecular simulations played in advancing the development of CO_2-reactive ILs. Different simulation methodologies are discussed and analyzed in terms of the insights they can provide. Finally this chapter provides a discussion of future opportunities where simulations might aid in IL design. In the third chapter of this thesis the methods used to develop molecular models for AHA ILs are discussed.

In the fourth chapter of this thesis, the interactions between water and various AHA ILs are investigated using classical molecular dynamics CMD simulations. Water will be present in flue gas streams where ILs could be used to perform CO_2 separations. Understanding the interactions between water and AHA ILs is crucial because water could significantly alter the IL performance. Therefore, we investigate how water affects both the IL structure and dynamics to draw conclusions on the dominant interactions between these species. Additionally, water solubility is investigated for ILs with the same cation and different anions.

In the fifth chapter of this dissertation, IL structure is investigated using a combination of x-ray scattering experiments and CMD simulations. This study helps further the current understanding of microheterogeneities within ILs. The simulations are useful because they allow further information to be extracted from liquid structure functions that could otherwise remain hidden to experimentalists. This work tests how both ion substitution and CO_2 reaction cause changes in the liquid structure.

In the sixth chapter of this dissertation a method is presented to predict how much CO_2 will absorb into an AHA IL at a given temperature and CO_2 pressure. Being able to predict CO_2 absorption capacities is useful as it allows researchers to assess IL reactivity prior to synthesis in order to select optimal candidates while saving time and money. Due to the large IL design space, it is necessary to focus experimental synthesis efforts on only the most promising candidate ILs. The different interactions that give rise to the CO_2 absorption capacities are assessed in a quantitative manner. This assessment helps identify which assumptions can be used to evaluate reactivity and compare different ILs. The methods used in this work can also help in the development of future models that seek to assess the reaction of gaseous species in reactive liquid solvents. Finally, this dissertation concludes with a summary of the the results found and a reflection on how these works have advanced our current understanding of AHA ILs.

CHAPTER 2

ROLE OF SIMULATIONS IN THE DEVELOPMENT OF CO_2-REACTIVE ILS

2.1 Introduction

In recent decades a tremendous research effort has aimed to improve current CO_2 separation technologies. To this end, several researchers have examined diverse technologies including metal organic frameworks, membranes, electrochemical catalytic reduction, solid sorbents, and reactive liquid solvents [17–25]. Part of this effort is motivated by the fact that CO_2 separations are commonplace in oil and natural gas processing, and therefore, improving the separation will have a significant economic benefits to minimize utilities costs within the energy industry. Additionally, the advancement of CO_2 separations is of fundamental importance to mitigating CO_2 emissions, which are widely regarded to be the primary cause of anthropogenic global warming [17, 26–28]. The continuation of current emission rates may have adverse effects on global climate, leading to serious social and economic consequences [29, 30], and therefore, efforts must be taken to curb the emission rates. In the short term, a promising way to reduce CO_2 emissions is to perform carbon capture at point source emitters such as coal fired power plants, which are estimated to contribute approximately 30% of total CO_2 emissions in the US [31, 32].

Absorber/stripper units are the most developed technology that could be implemented for industrial scale CO_2 separations. Amine absorption towers, which have been applied in natural gas processing to remove CO_2 and H_2S sour gases, are the best currently available technology for performing post combustion CO_2 capture

from coal fired power plants [32]. Large scale CO_2 capture using amines hasn't been widely applied at coal fire power plants, however, due to the high energy cost of the separation. It is estimated that industrial CO_2 capture using amines would require approximately 30% of the energy produced by coal fired power plants, which is far above the theoretical minimum of 10% [33, 34]. Therefore, amine technologies do not adequately meet criteria set forth by the Department of Energy to capture 90% of the emitted CO_2 with the increased cost of electricity below 35% [35]. There are two main reasons why amine units are energy intensive: 1) reaction of CO_2 with amines occurs according to a 1:2 CO_2/amine reaction stoichiometry [36–38], 2) amines are mixed with 70 wt % water causing a significant parasitic energy loss in the regenerator [39–41]. Besides the high energy requirements, amines have several other problems that add to the cost of the separation. Amines can undergo thermal degradation and oxidation reactions [42–45] and they are volatile, which increases operating costs from necessary solvent replacement or recovery processes and results in harmful chemical emissions [46–49]. Additionally, amines react to form corrosive bicarbonate species, which adds significant capital costs from the need to use corrosion resistant materials in absorber/stripper units that may eventually require replacement due to corrosion damage [50–52].

Over the last few decades, ionic liquids (ILs) have gained considerable attention as designer solvents capable of outperforming current amine technologies in conventional absorber/stripper separation units. Research into CO_2 capture ILs was sparked by the fact that ILs tend to selectively absorb CO_2 in the presence of other flue gas species [53–58]. In addition to their naturally high CO_2 affinities, ILs have several unique properties that provide practical advantage over amines. They have negligible vapor pressures, which reduce harmful atmospheric emissions and costs from solvent replacement or recovery processes [59]. ILs typically have high thermal stabilities, which improves their solvent lifetime and allows for a large temperature range of

operation [60]. Although certain ILs are corrosive towards some metals at high temperature [61, 62] or in the presence of water [63], many are noncorrosive [61, 64]. The most attractive feature of ILs is the ability to tune their physical and chemical properties through proper pairing of anions and cations [65–73]. Furthermore, the fact that many ILs do not need to be mixed with water to absorb CO_2 reduces parasitic energy loss during regeneration [34]. All of these properties make ILs promising solvents for CO_2 separations.

In the present chapter, a review of the advancement of ILs which chemically bind CO_2 is presented while emphasizing the role of computer simulations in understanding experimental results and extending experimental discoveries. The remainder of the chapter is organized as follows: Section 2 discusses the historical developments made on reactive ILs highlighting the interplay between simulation and experiment with respect to CO_2 absorption, Section 3 discusses advantages simulations offer regarding other design criteria, Section 4 provides a perspective on outstanding issues where simulations might aid in understanding IL behavior, Section 5 concludes with an outlook of the role of simulations in advancing CO_2-reactive ILs, and Section 6 lists the abbreviations used for the different ions discussed in this chapter. This chapter focuses on the computational work done on CO_2-reactive ILs which react with CO_2 up to a 1:1 CO_2/IL reaction stoichiometry. A complete review of CO_2 capture using ILs is beyond the scope of the present work. For further reading on ILs developed to cooperatively bind CO_2 beyond a 1:1 CO_2/IL reaction stoichiometry through multiple-site cooperation, interested readers may want to read a recent review by Cui *et al.* [74]. For additional information on the development of ILs for CO_2 capture, the reader maybe be interested in several additional review papers on the topic [53, 65, 66, 68–70, 72, 73].

2.2 Historical Development of CO_2-Reactive ILs

2.2.1 Amine Functionalized Cation ILs

Early research on applying ILs to CO_2 capture focused on physisorption systems where CO_2 will interact strongly with the cations and anions, but it will not react to form chemical bonds [54, 57, 75, 76]. While these systems were able to selectively absorb CO_2 in the presence of other species, the low absorption capacities of these ILs makes it infeasible to use them in post combustion CO_2 capture due to the low partial pressure of CO_2. Owing to this limitation, improving the CO_2 absorption capacities of ILs became one of the main focuses of researchers in the IL community.

In 2002, Bates *et al.* [77] introduced the concept of the task specific IL (TSIL) by introducing amine functionality to the imidizolium cation, which allowed it to react with CO_2 in a 1:2 CO_2/IL stoichiometric ratio according to the reaction scheme shown in Figure 2.1.

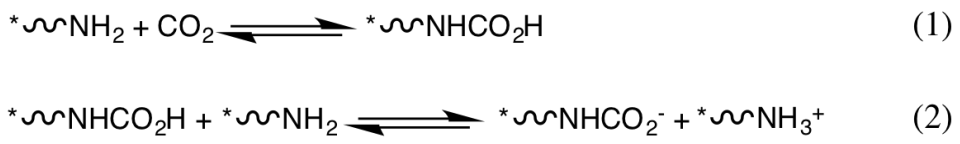

Figure 2.1. Amine 1:2 reaction mechanism.

The ability to form reversible chemical bonds vastly improved IL CO_2 absorption capacities making them comparable to conventional amines. This first generation CO_2-reactive IL suffered from a dramatic increase in viscosity upon reaction with CO_2, however, that prevented it from being used in a conventional amine stripper/absorber

unit.

In one of the first simulation works on CO_2-reactive ILs, Yu *et al.* [78] used a combination of classical molecular dynamics (CMD) simulations and *ab initio* calculations to investigate the molecular origin of the high viscosities of unreacted amine functionalized imidizolium ILs introduced by Bates [77]. The CMD simulations showed that the amine functionalized ILs have stronger cation-anion interactions than the corresponding IL without amine functionality. The added NH_2 group is a strong interaction site between cations and anions and most of the anions will participate in ion-type hydrogen bonding interactions with this moiety. *Ab initio* calculations of cation-anion interaction energies supported the CMD simulation results and demonstrated the high stability of the hydrogen bonding configurations. Calculated rotational energy profiles for the imidizolium side chains showed that the hydrogen bonding interactions reduced the mobility of the imidizolium side chains. This work concluded that the formation of hydrogen bonding networks within the IL is the primary reason for the high viscosity of the functionalized IL.

Following the work of Yu *et al.* [78], Gutowski *et al.* [79] used CMD simulations to identify the molecular mechanism behind the viscosity increase of amine functionalized imidizolium ILs upon reaction with CO_2. Gutowski found that part of the reason that the unreacted systems have such high viscosities is that replacement of a CH_2 group by an NH_2 functional group causes the density of the IL to increase by 10%. When 10% of the IL was reacted with CO_2, the apparent self-diffusivities of the ions decreased by an order of magnitude, which reflected the experimentally observed viscosity increase. When 20% of the IL was reacted with CO_2, the dynamics decreased further and the mean squared displacements (MSDs) for the product zwitterion and the dication were nearly identical, which indicated that interaction between these species might cause the observed decrease in dynamics. Similarly, the rotational dynamics decreased with increasing extent of reaction, and at the maxi-

mum extent of reaction, virtually no rotational motion occurred. Hydrogen bonding analysis and calculated radial distribution functions (RDFs) demonstrated that the observed changes in system dynamics upon reaction with CO_2 were primarily due to the formation of pervasive hydrogen bonding networks between the zwitterion and the dication. The ability of CMD to investigate the interplay between structural interactions and system dynamics proved to be extremely useful in understanding the first CO_2-reactive IL and opened the door to subsequent computational studies of these systems.

2.2.2 IL/Amine Mixtures

Due to the high viscosity of the first generation TSILs, researchers sought alternative reactive systems with lower viscosities. One obvious choice was to take advantage of the known amine chemistry and IL tunability by dissolving amines in ILs. In 2008, Camper *et al.* [80] demonstrated that monoethanolamine (MEA) and diethanolamine (DEA) can be dissolved in ILs with the $[Tf_2N]^-$ anion. The amines in these mixtures still react with CO_2 in a 1:2 CO_2/amine mechanism to form a carbamate complex [81]. However, the resulting carbamate complex is insoluble in the mixture and instead forms a precipitate that helps to drive the reaction forward and improves the reaction kinetics. These mixtures provide several benefits compared to previous TSILs, because they are cheaper to make and the lower viscosity allows them to be implemented in existing amine scrubbing towers. However, researchers still sought to develop solvents with greater absorption capacities in order to improve the efficiency of the absorption process.

2.2.3 Amine Tethered Anion ILs

After discovering that amine tethered cations can chemically absorb CO_2, some researchers reasoned that anions could also be tuned to bind CO_2 [1, 2, 82]. Mindrup

et al. [1, 82] performed quantum chemical calculations which indicated that when the amine is tethered to the anions instead of the cations, the reaction in Figure 2.1 favors step 1 instead of step 2, which allows a 1:1 CO_2/IL reaction stoichiometry to be achieved [1] instead of the 1:2 CO_2/IL stoichiometry demonstrated by previous amine functionalized imidizolium ILs. Therefore, there is an additional degree of freedom when designing TSILs to functionalize either the cation or the anion. Furthermore, enthalpies of reaction calculated at the 6-311++G(d,p) level of theory gave -71 and -55 kJ mol^{-1} for prolinate and methioninate complexes shown in Figure 2.2, which were in reasonable agreement with the experimental calorimetry values of -80 and -64 kJ mol^{-1} [1] . *Ab initio* calculations on single ion gas phase reactions were able to correctly predict both the reaction mechanism and reaction thermodynamics in good agreement with observed experimental results.

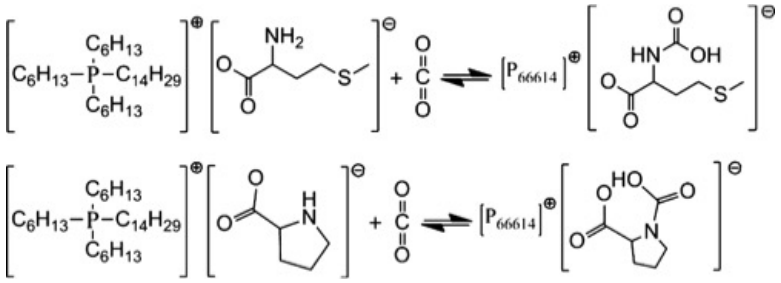

Figure 2.2. Reaction Schematics of CO_2 with $[P_{66614}][Met]$ (top) and $[P_{66614}][Pro]$ (bottom). Figure reproduced with permission from ref [1]. Copyright 2010 American Chemical Society.

Following this work, Goodrich *et al.* [2] synthesized six amine functionalized anion-tethered ionic liquids, which are shown in Figure 2.3. All of these ILs absorbed more than 0.5 mole CO_2/IL at a pressure of 1 bar. Therefore, two different reaction

models were proposed to account for the CO_2 absorption. The first model included both a 1:2 and a 1:1 CO_2/IL reaction mechanism. The second model only included the 1:1 CO_2/IL reaction mechanism from the addition of CO_2 to the anion, but it also considered the deactivation of reactants through unknown side reactions. Both models were able to fit the experimental isotherms fairly well. While these anion functionalized ILs showed superior absorption capacities to cation functionalized ILs, they suffered from similar high viscosities upon reaction with CO_2. The viscosities of the anion functionalized ILs increase up to 100 fold upon reaction with CO_2, and therefore, they are unsuitable for use in conventional stripper/absorber columns. The viscosity increase is likely due to the formation of hydrogen bonding networks similar to what was observed in the cation functionalized ILs [77–79].

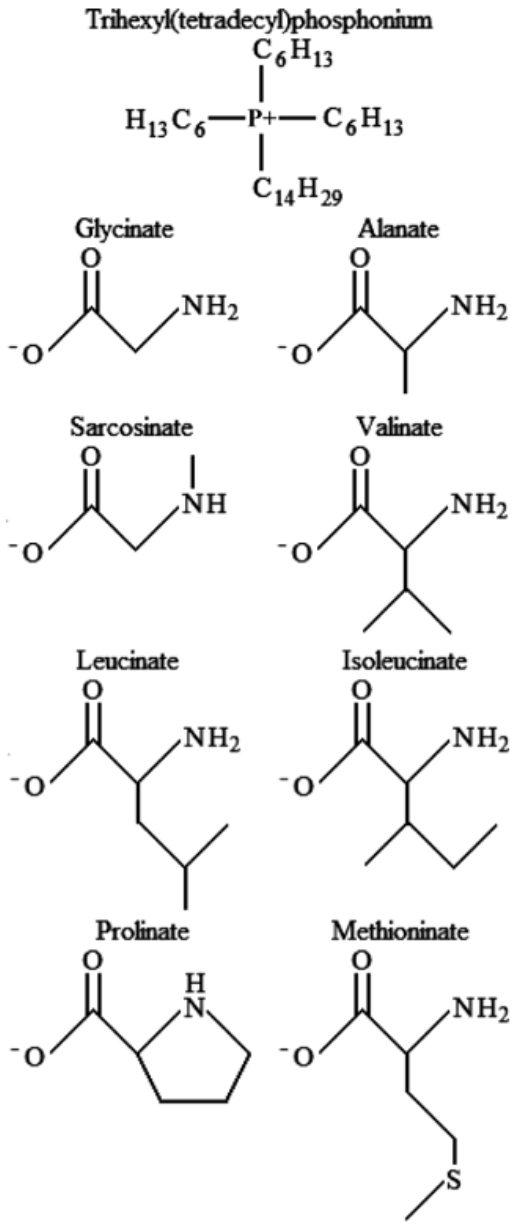

Figure 2.3. Structures of cation and amine-tethered anions studied by Goodrich *et al.* [2]. Figure reproduced with permission from ref [2]. Copyright 2011 American Chemical Society.

2.2.4 Amino Acid ILs

Following the discovery of TSILs, researchers reasoned that ILs made by neutralizing [emim][OH] with amino acids (AA) introduced by Ohno *et al.* [83, 84] could be functionalized to react with CO_2. These ILs are particularly interesting from an economic stand point because the use of naturally occurring AA precursors is a novel way to reduce the IL synthesis costs. Zhang *et al.* [85] synthesized ILs by pairing phosphonium cations with various AA anions. In the dry ILs, CO_2 reacted up to the theoretical 1:2 CO_2/IL to form carbamate species. In the presence of water, however, these AA ILs were able to react up to 1:1 CO_2/IL, which indicated that a different reaction mechanism was occurring in the wet systems leading to the formation of bicarbonate species. While AA ILs are relatively cheap to synthesize and they have high absorption capacities, they too suffer from a large viscosity increase upon reaction with CO_2. Based on the findings of Gutowski *et al.* [79], Luo *et al.* [86] argued that the viscosity increase from reaction with CO_2 could be avoided if the reacted species favored intramolecular hydrogen bonding over intermolecular hydrogen bonding. Using *ab initio* calculations on single gas phase ions, they found that the addition of nitrogen and oxygen atoms to the AA anions caused them to favor intramolecular hydrogen bonding over intermolecular hydrogen bonding. Experimental IR spectroscopy verified the formation of these intramolecular hydrogen bonds, and when the ILs reacted with CO_2, the viscosities either decreased or increased only slightly. However, the viscosities of the unreacted AA ILs were still too high for typical industrial applications.

In order to gain a better understanding of the reaction mechanism in AA ILs, Firaha *et al.* [3] used a combination of *ab initio* molecular dynamics (AIMD) simulations and implicit solvent quantum chemical calculations to examine AA IL reaction chemistry. The AIMD simulations were used to investigate the reaction mechanism of CO_2 with an example [emim][Gly] AA IL in order to surmise a general understanding

of AA IL reaction chemistry. In one simulation scenario, CO_2 was randomly inserted into a pre-equilibrated IL system in order to examine the time evolution of the reaction. A second simulation started from the products of the reaction: cations, anions, and the product glycinate zwitterions and carbamates. These simulation sought to examine which of the reaction pathways shown in Figure 2.4 were the preferred CO_2 absorption mechanisms.

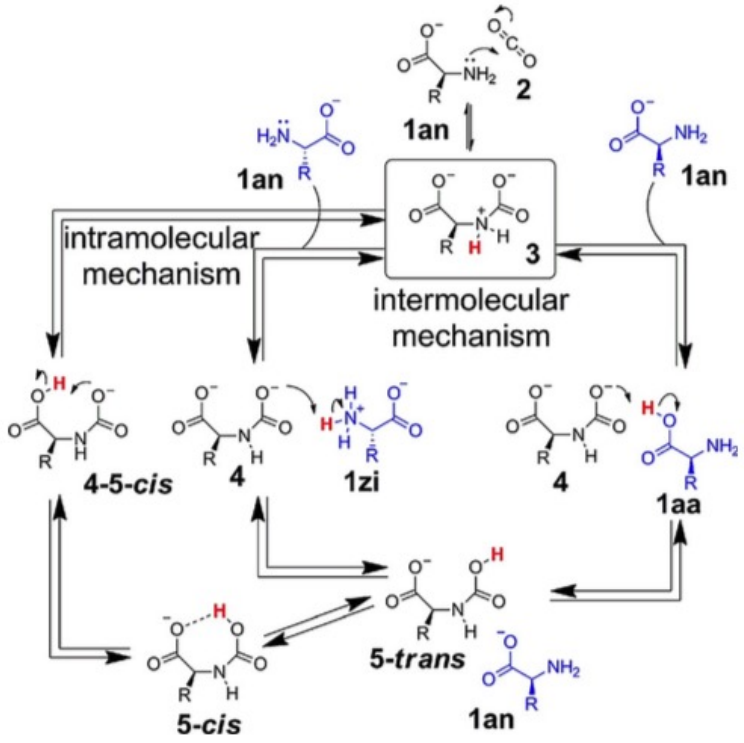

Figure 2.4. Possible CO_2 reaction pathways for AA ILs. Figure reproduced with permission from ref [3]. Copyright 2016 Wiley.

Additionally, the free energies of reactants, intermediates, transition states, and prod-

ucts for a series of 50 ILs consisting of AA anions paired with either imidizolium or phosphonium cations were calculated with implicit solvent density functional theory (DFT) using the COnductor-like Screening MOdel for Realistic Solvents (COSMO-RS). Free energy barriers were calculated in order to quantify relative reaction rates in the different AA ILs. The composite uncertainty of the methods used was approximately 10 kJ mol^{-1}, which prevented quantitative prediction of accurate reaction rates. Comparison of free energy barriers, however, allowed a qualitative ordering of reaction rates to be obtained. When calculating the relative reaction rates, it was assumed that no reaction occurred between the cations and anions due to the low basicity of the anions. Results from the AIMD simulations were analyzed in terms of correlated distribution functions (CDFs) of unique pair distances representative of the different possible reactions in the systems. The AIMD results verified the methods used to calculate the relative free energies of reactants, transition states, intermediates, and products. Based on the simulation results, the most likely mechanism for the reaction of [emim][Gly] with CO_2 is the formation of the glycinate-CO_2 adduct followed by proton abstraction from the amino or carboxylate groups, and the rate determining step is the formation of the glycinate-CO_2 adduct. After verifying the methods used to calculate relative free energies of the reaction species, the relative reaction rates of the 50 different AA ILs were calculated and compared. The analysis was able to correctly predict that out of all the AA ILs examined, $[P_{66614}]$[Pro] has the quickest experimentally observed reaction rate [87]. The study concluded that the nature of the anion is responsible for the preferred reaction mechanisms and whether or not the reaction favors a 1:2 or 1:1 CO_2/IL reaction stoichiometry.

While AIMD simulations are often preferred for examining reactions in the condensed phase, they suffer from both accessible time scales and system size limitations. In order to simulate dynamics of large systems for longer time scales, Zhang *et al.* [88] performed the first reactive force field (ReaxFF) parameterization for a CO_2-reactive

IL, $[P_{4444}][Gly]$. Though difficult to parameterize, ReaxFF provides a reasonable compromise between CMD simulations and AIMD simulations by allowing reactions to occur during dynamics with a computational expense that allows significantly larger systems to be simulated for longer timescales than AIMD simulations [89, 90]. The ReaxFF simulations were able to observe multiple instances of proton transfer which was not directly observed in previous AIMD simulations of other AA ILs [3] or in CMD simulations of the same IL [91], but rather was simply inferred based upon observed pair distances over the course of the simulations. Although ReaxFF allows rare reaction events to be observed in CMD simulations, its use has not been widely adopted within the IL community due to the difficulty of the parameterization procedure and the extensive *ab initio* data sets that are required for proper fitting of the numerous force field parameters.

2.2.5 Acetate Anion ILs

Ionic liquids with the acetate anion were some of the first reported CO_2-reactive ILs [92–95]. These ILs were first reported to react reversibly in the literature [93, 94]. However, more recent studies have shown that due to the fact that acetic acid is a weak acid, the $[Ac]^-$ anion will have a tendency to reprotonate and form a neutral species [95–100]. Besnard *et al.* [96] used nuclear magnetic resonance (NMR) experiments to investigate the reaction of [bmim][Ac] with CO_2 in order to determine the reaction products and reaction pathways. These experiments showed that the reaction gave rise to several products including 1-butyl-3-methylimidazolium-2-carboxylate and acetic acid, which was present in stable dimers. At high water content, bicarbonate was formed thereby reducing carboxylate formation. While the IL was reactive, these results presented a different picture of the reaction mechanism than the reversible complex formation previously proposed in the literature [93, 94]. The reaction of CO_2 with [bmim][Ac] and [bmim][TFA] was also investi-

gated by Cabaco *et al.* [97] using both Raman spectroscopy and DFT calculations. Their results showed that the reaction of CO_2 with [bmim][Ac] has two regimes: one up to 0.35 mole fraction CO_2 where carboxylation occurs and acetic acid is formed, and the other corresponding to physical absorption and the formation of the Fermi dyad. The CO_2 solubility in the fluorinated IL was lower than in the hydrogenated IL in the first regime due to chemical reaction. At higher pressures the solubility was higher in the fluorinated system due to increased physical solubility from favorable interactions between CO_2 and the fluorine groups. Cabaco *et al.* [97] also found that the reaction of CO_2 with the acetate anion was irreversible due to the formation of acetic acid. While finding that the first proposed reversible reaction scheme of CO_2 with $[Ac]^-$ ILs was wrong, these researchers concluded that more work was needed to fully understand the different possible reaction mechanisms.

Several researchers have used AIMD simulations to provide additional insights into the behavior of acetate anion ILs. Hollóczki *et al.* [98] used AIMD to simulate a periodic system of 1 CO_2 placed in 36 ion pairs of [emim][Ac]. In agreement with previous experimental and simulation studies, the CO_2 interacted most strongly with the anion and bent significantly from linearity when binding to the anion. There was, however, a strong interaction between the CO_2 and the imidizolium ring as confirmed by structural analysis of the AIMD simulation as well as static calculations of CO_2 imidizolium systems. This finding helped explain why the CO_2 solubility is higher when $[Ac]^-$ is paired with imidizolium cations rather than pyrolidinium cations. One important finding of Hollóczki is that dispersion interactions are required in order for the simulations to correctly model the bent structure of CO_2, which was confirmed with IR spectroscopy results. Brehm *et al.* used AIMD simulations to investigate [emim][Ac] and its mixture with water [99, 100]. They found that in the pure IL, the oxygen atoms of the $[Ac]^-$ anion participated in strong hydrogen bonding interactions with the ring hydrogens of the $[emim]^+$ cation and the O-H distance between

the counterions will occasionally match the C-H distance in the $[Ac]^-$ anion, indicating that proton transfer between counterions may be likely in this system. Likewise, when water was added to the IL, there was evidence that the $[Ac]^-$ anion will abstract a hydrogen from water to form acetic acid. However, it is difficult to observe this transfer directly in the simulations due to the limited time scales. While chemical intuition is able to make inferences on reaction behavior in ILs, experimental measurements supplemented by simulations results help to elucidate complex chemical processes, especially in systems with competing reactions.

2.2.6 Switchable Solvents and Silylamines

Another class of CO_2-reactive ILs that was first proposed by Jessop *et al.* for reactive CO_2 capture is switchable solvents which change from a neutral form to an IL form upon reaction with CO_2 [101]. One class of switchable solvents is made from mixtures of alcohol and either guanidine or amidine species which change to an ionic liquid form upon reaction with CO_2 as demonstrated in Figure 2.5. The use of such a system is not only applicable for CO_2 capture, but also for implementing reactions with CO_2 because the reaction can be carried out followed by a separation based on the polarity change of the solvent [102, 103]. Phan *et al.* demonstrated that these switchable solvents can react up to 1:1 CO_2/IL and that the reaction can be reversed to desorb the CO_2 either by heating or bubbling N_2 [4]. Higher conversion is achieved for primary alcohols than secondary and tertiary alcohols. Due to the polarity change, the viscosity of these switchable solvents increases by two orders of magnitude upon going form the neutral form to the IL form. Reaction in these solvents, therefore, is limited by the diffusion of CO_2 [104]. While these solvents are able to selectively absorb CO_2 in the presence of N_2, they will react to form bicarbonate species in the presence of water.

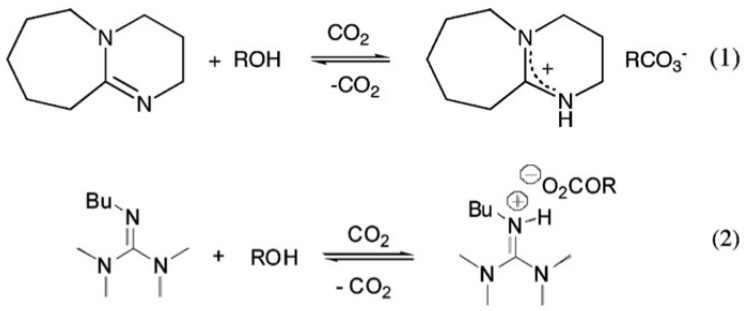

Figure 2.5. Reaction of alcohol/amidine mixtures (top) and alcohol/guanidine mixtures (bottom) with CO_2 to form an IL. Figure reproduced with permission from ref [4]. Copyright 2008 American Chemical Society.

Silylated amines are another class of switchable solvents which will change from a neutral form to an IL form upon reaction with CO_2 [102, 103, 105, 106]. Silylamines react with CO_2 according up to 1:2 CO_2/IL stoichiometry following the reaction mechanism of amines. While their chemical capacity for CO_2 is similar to MEA, these reversible ILs (RevILs) have high void fractions that give rise to enhanced physical solubilities. CO_2 can be desorbed and the original silylamine recovered by bubbling N_2 or by heating to moderate temperatures (100 C°). While CO_2 can react with alkonolamines, the resulting product is a solid, and the process requires a cosolvent for transport and separation. Using alkonolamines wastes a lot of energy heating the cosolvent to regenerate the alkonolamines.

Switchable solvents which form RevILs are thus advantageous because no cosolvent is required, which greatly reduces the energy penalty for regeneration of reactants. These RevILs are not yet suitable in industrial processes, however, because they suffer from the same drastic viscosity increase upon reaction with CO_2 as previous amine functionalized ILs. Blasucci *et al.* [107] examined structure property

relationships involving viscosity, polarity, and regeneration temperatures for a series of silylamines. The viscosities of silylamines decrease as the alkyl side chain lengths increases due to the reduced packing efficiency, which in turn increases the physical solubility of CO_2 by lowering the density and increasing the void fraction. The precursor viscosity is reduced for siloxylated amines relative to the corresponding silylated amines. The stability of the silylated amines in the presence of water, however, is higher than for the siloxylated amines. The reversal temperatures for various RevILs range between 100-150 $^{\circ}C$.

Simulation studies using the COSMO-RS approach were able to extend the understanding of CO_2 solubility in silylamines [108, 109]. While the COSMO-RS method was unable to quantitatively predict CO_2 absorption isotherms, the calculated solubility results were in qualitative agreement with available experimental results [108]. COSMO-RS results of Gonzales *et al.* [109] showed that increasing the alkyl chain lengths and the number of methyl substituents increases the CO_2 solubility by increasing van der Waals interactions and creating more void space within the IL. Furthermore, the COSMO-RS calculations showed that the addition of fluorine groups that interact favorably with CO_2 can increase the absorption capacity while simultaneously reducing the regeneration temperature. While several researchers have concluded that flourination creates favorable interactions for CO_2 absorption [97, 109], this result has recently come into question [110]. Computer simulations can aid in the development of structure property relationships, which helps to create design heuristics that experimentalists can use to select appropriate candidate ILs prior to synthesis and experiment.

2.2.7 Aprotic Heterocyclic Anion and Superbase ILs

While many of the first CO_2-reactive ILs demonstrated high CO_2 chemical solubilities, the high viscosities of these initial systems prevented them from gaining

traction in industry. However, the development of TSILs demonstrated that IL tunability could provide a platform for highly efficient reversible CO_2 capture as well as a means to control hydrogen bonding interactions, and thus, the viscosity. With the knowledge of hydrogen bonding mechanism responsible for the high viscosity in many CO_2-reactive ILs, Gurkan *et al.* [6] proposed that N-heterocyclic pyrrolide anions could be suitable for reversible CO_2 capture due to their isoelectronic structure with N-heterocyclic carbenes, which have been shown to react with CO_2. To test this idea, the structures and energies of reactant pyrrolide, CO_2, and product pyrrolide-CO_2 complexes were calculated at the G3 level of theory. The calculations indicated a strong reactivity of pyrrolide towards CO_2 and that the reaction energetics could be tuned through introduction of either electron donating or electron withdrawing groups on the pyrrolide ring. CMD simulations of $[P_{4444}]$[2CNpyr] over a full range of reaction compositions showed that the IL dynamics were not significantly affected by the reaction with CO_2. Therefore, this IL was experimentally synthesized and absorption isotherms were measured that supported a 1:1 CO_2/IL reaction mechanism, which was further verified by the presence of a carbonate peak in the NMR spectrum. Experimental measurements confirmed that the reaction with CO_2 does not have significant effects on the IL viscosity due to the aprotic nature of the anions, which prevents the formation of hydrogen bonding networks and salt bridges that were seen in previous ILs. Furthermore, the addition of 6.3 wt% water to the IL did not prevent it from achieving a high absorption capacity. Aprotic heterocyclic anion (AHA) ILs proved to be a tunable low viscosity class of ILs with the capability of absorbing CO_2 under flue gas conditions.

Wu *et al.* [111] performed CMD simulations of both unreacted and CO_2-reacted $[P_{4444}]$[2CNpyr] to elucidate the experimentally observed viscosity behavior of AHA ILs. The simulations demonstrated that the translational and rotational dynamics were independent of the extent of reaction, with the exception of a small difference

in the rotational dynamics of the the unreacted and CO_2 complexed anions. The observation that the IL dynamics did not change much upon reaction with CO_2 was explained by the fact that the amount of intermolecular hydrogen bonding did not change much with the extent of reaction. Calculation of Henry's law constants for N_2, O_2, CO_2, and H_2O showed that the solubilities of these gases were similar in the unreacted and CO_2-reacted ILs, with the exception of H_2O, which was approximately ten times more soluble in the CO_2-reacted IL due to favorable hydrogen bonding interactions with the reacted anion.

Sheridan *et al.* [112] used a combination of X-ray scattering experiments and CMD simulations to investigate how the liquid structure of AHA ILs changes from both cation and anion substitutions as well as anion reaction with CO_2. The liquid structure functions were both measured and computed for a series of four ionic liquids composed of two different phosphonium cations, $[P_{2228}]^+$ and $[P_{66614}]^+$, paired with two different AHA anions, $[2CNpyr]^-$ and $[4Triaz]^-$. The simulated and experimental structure functions were in reasonable agreement, showing that the liquid structure functions are relatively insensitive to the anion and whether or not it is reacted with CO_2. The fact that the liquid structure function does not change appreciably upon reaction with CO_2 further helps to explain why the viscosities of AHA ILs do not change much when they react with CO_2, because the liquid structure, and thus the intermolecular interactions giving rise to the viscosity, do not change much upon reaction with CO_2. The liquid structure functions of the AHA ILs had three primary features which are present in the liquid structure functions of other classes of ILs: a prepeak corresponding to long range ordering of polar and non-polar domains, a charge alternation feature corresponding to alternation of ions within the polar domain, and an adjacency peak resulting from close range interactions of molecules within the same solvation shell [113–120]. While all of these features were not directly seen in the experimental structure functions, the simulated structure functions

allowed for the total structure function to be partitioned into partial structure functions correlating specific species. This partitioning of the total structure function helped reveal important features not present in the total structure function due to cancellation of peaks and antipeaks. Both the experimental and simulated structure functions showed that the liquid structure function is sensitive to the cation, because the cation has both polar and non-polar components that cause the IL to organize into two distinct domains. While experiments are able to measure the total liquid structure function, CMD simulations are able to provide additional insights into the liquid structure by identifying which interactions give rise to the experimentally observed features. CMD simulations provide important insights into the relationship between liquid structure and observed physical properties.

Simulations proved to be invaluable in designing AHA ILs and understanding their properties. The ability of *ab initio* and CMD simulations to work in a predictive manner not only allowed researchers to understand IL behavior, but it also helped guide the design of AHA ILs prior to synthesis. By understanding the viscosity mechanism of amine functionalized imidizolium ILs and AA ILs, researchers were able to design AHA ILs to have low viscosities while maintaining high absorption capacities. The design of low viscosity, tunable ILs was monumental in advancing the application of CO_2-reactive ILs for post combustion CO_2 separations.

At the same time that AHAs were being synthesized, the Dai group was pioneering research on superbase ILs that have many of the same desirable properties of AHA ILs [8, 121–123]. Superbases are neutral organic solvents with conjugate acids that cannot be deprotonated by the hydroxide ion. Wang *et al.* [121] synthesized a series of ILs made from imidizolium cations paired with different superbase anions. These superbase ILs reacted with CO_2 to form amidinium carboxylate salts and were able to achieve absorption capacities of 1 mol CO_2/IL depending on the superbase. These superbase ILs showed relatively high absorption rates due to their low viscosities,

and the absorbed CO_2 could easily be desorbed by heating. When water was added to the superbase ILs, however, the CO_2 absorption capacities remained the same but the reaction mechanism changed and bicarbonate formation was detected from the reaction of the superbase with water. While superbase ILs demonstrated high CO_2 absorption capacities and low viscosities, the selectivity of superbase ILs to absorb CO_2 over N_2 was fairly low (typically < 10) [122].

Both superbase ILs and AHA ILs are excellent candidates for CO_2 capture because they have high absorption capacities and also high kinetic rates owing to the fact that the reaction with CO_2 has a minimal effect on the IL viscosities. Some of these ILs have a rather strange behavior where the viscosity will even decrease after reaction with CO_2 [5, 7]. Li *et al.* [5] used CMD simulations in order to understand why the viscosity of $[P_{66614}][Im]$ decreased after reaction with CO_2. Viscosities calculated using non-equilibrium dynamics showed that the viscosity does indeed decrease upon reaction with CO_2 as shown in Table 2.1. Both the rotational and translational dynamics were larger for the reacted IL than for the unreacted IL. Interestingly, the amount of hydrogen bonding does increase in the reacted IL due to favorable interactions with the negatively charge oxygen atoms, but this does not result in a higher viscosity. This observation suggests that unlike amine functionalized ILs, hydrogen bonding does not play a critical role in the system dynamics of superbase ILs. In the unreacted IL where the ions are symmetric, counterions distribute about each other in a symmetric fashion. This symmetric distribution of counterions causes their respective motions to be highly correlated, which results in slow system dynamics that are consistent with a higher viscosity. When the IL reacts with CO_2, however, the charge distribution in the anion becomes more asymmetric, thus creating an asymmetric distribution of the cations about the anions as shown in Figure 2.6. This asymmetry helps to break up the correlated motions of counterions, thereby allowing the ions to translate and rotate more freely. Li [5] suggested that asymmetry

of CO_2-reacted product anions can therefore be utilized to reduce IL viscosity. In support of this mechanism for the viscosity decrease, experiments on other aprotic anions which are symmetric in the unreacted state and asymmetric in the reacted state demonstrate the same decrease in viscosity upon reaction with CO_2 [7] as shown in Figure 2.7. The additional structural evidence provided by MD is a powerful tool in developing theories to explain experimental viscosity measurements.

TABLE 2.1

SIMULATED VISCOSITY OF THE NEAT AND SATURATED ILS IN COMPARISON WITH EXPERIMENTAL DATA OF $[P_{66614}][IM]$ BEFORE AND AFTER CO_2 ABSORPTION

	$[P_{66614}][Im]$	$[P_{66614}][ImCO_2]$
experiment [124]	810.4	648.7
simulation	897.0 ± 26.5	516.9 ± 28.4
relative error	11 %	-20 %

Table reproduced with permission from ref [5]. Copyright 2014 American Chemical Society.

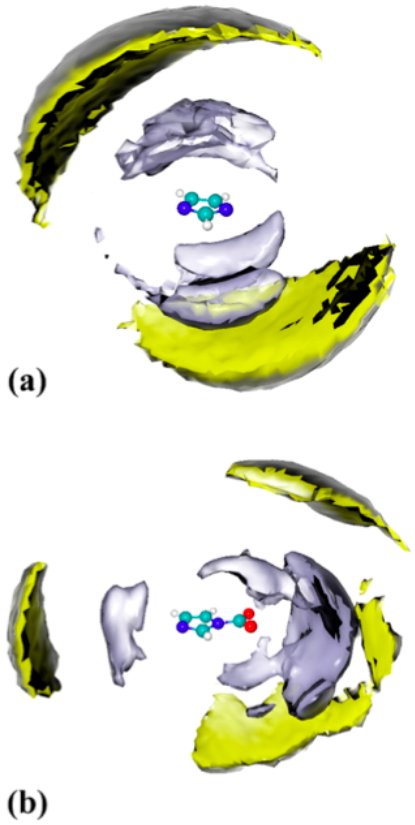

Figure 2.6. SDFs for central $[Im]^-$ for unreacted (top) and CO_2-reacted (bottom) $[P_{66614}][Im]$. Figure reproduced with permission from ref [5]. Copyright 2014 American Chemical Society.

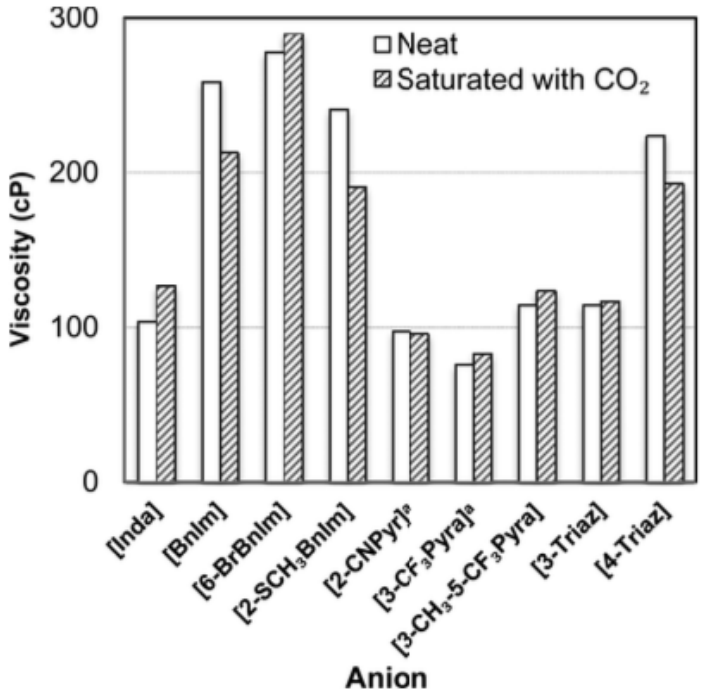

Figure 2.7. Viscosities of unreacted (white) and CO_2-reacted (gray) $[P_{66614}][AHA]$ ILs at 50 °C. [a]From Gurkan *et al.* [6]. Figure reproduced with permission from ref [7]. Copyright 2014 American Chemical Society.

2.2.8 Phenolic ILs

In a subsequent work by the Dai group, superbase protic ionic liquids (PILs) were derived by deprotonation of weak proton donors using super bases [8]. The PILs reacted with CO_2 to form liquid carbonate, carbamate, or phenolate salts. Depending on the anion, these PILs were capable of reacting up to 1:1 CO_2/IL. PILs made from reacting diols with superbases have two reaction sites, and are capable of reacting up to 2:1 CO_2/IL. The polarity of PILs can be tuned through choice of proton donor, which can be advantageous for use in organic reactions to simplify the separation process by inducing a phase split in the liquid product. Reaction energetics for the

reactions shown in Figure 2.8 were calculated at the B3LYP/TZVP level of theory giving reaction energies of -116.8, -85.2, and -41.7 kJ mol^{-1} for $[TFE]^-$, $[Im]^-$ and $[PhO]^-$, respectively. These reaction energetics indicated a weak driving force in $[PhO]^-$ ILs that helped to explain their low absorption capacities.

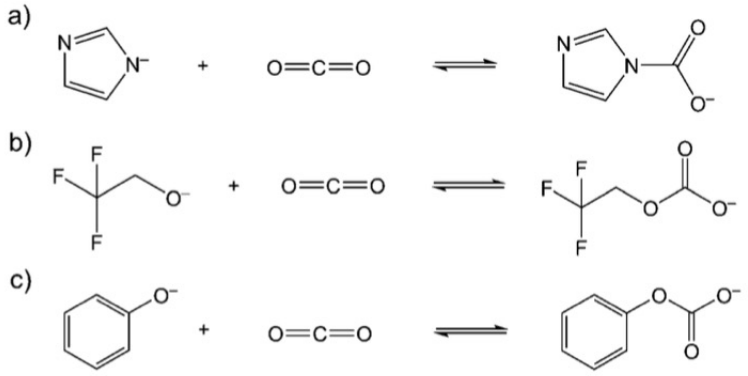

Figure 2.8. Reaction of PILs with CO_2. Figure reproduced with permission from ref [8]. Copyright 2010 Wiley.

Further calculations on phenolate ($[PhO]^-$) ILs demonstrated that the main determinant for the reactivity with CO_2 as well as the thermal stability of the IL is the amount of charge on the phenolate oxygen [125]. When the oxygen is more negative from the addition of electron donating groups to the phenolate ring, the IL will be more reactive with CO_2, but it will also have a lower thermal stability. The IL can be made more stable by decreasing the pk_a of the anion, however, the increased stability is incurred at a cost of lowering the CO_2 absorption capacity. The absorption capacities of various phenolic ILs are compared in Table 2.2.

The type of substituent (electron donating or electron withdrawing) as well as the

TABLE 2.2

THE EFFECT OF THE POSITION AND THE NUMBER OF SUBSTITUENTS, TEMPERATURE, AND WATER ON CO_2 CAPTURE IN PHENOLIC ILS

IL	T[°C][a]	CO_2 absorption[b]
$[P_{66614}]$[4-Cl-PhO]	30	0.82
$[P_{66614}]$[3-Cl-PhO]	30	0.72
$[P_{66614}]$[2-Cl-PhO]	30	0.67
$[P_{66614}]$[2,4-Cl-PhO]	30	0.48
$[P_{66614}]$[2,4,6-Cl-PhO]	30	0.07
$[P_{66614}]$[4-Cl-PhO]	50	0.65
$[P_{66614}]$[4-Cl-PhO]	70	0.50
$[P_{66614}]$[4-Cl-PhO][c]	30	0.89
$[P_{66614}]$[4-Cl-PhO][d]	30	0.88
$[P_{66614}]$[3-NMe_2-PhO]	30	0.94
$[P_{66614}]$[4-Naph]	30	0.89
$[P_{66614}]$[2-Naph]	30	0.86

[a] Determined after 30 min.
[b] Mole CO_2 per mole IL.
[c] Addition of water (2 wt%) to the IL.
[d] Addition of water (5 wt%) to the IL.
Table reproduced with permission from ref [125]. Copyright 2012 Wiley.

ring position of the substituent not only affects the reactivity but also the IL viscosity, which can be seen in Table 2.3. The fact that both the physical and chemical nature of ILs are tied to functionalized groups presents both the challenge and opportunity in designing an IL [25]. Chemical intuition can often be used to assess how a given substituent on an ion will effect the reactivity, but it can be quite challenging to assess how it affects other important properties such as the viscosity and chemical stability.

Both the gas phase reaction thermodynamics and the IL viscosity can be assessed without *a priori* knowledge by using a combination of *ab initio* calculations and CMD simulations in order to help guide the synthesis of promising ILs. The observed trends in Table 2.2 were rationalized by calculating the optimized structures of the anions, CO_2, and the reacted anion-CO_2 complexes at the B3LYP/6-31++G(p,d) level of theory [125]. The resulting calculations for the enthalpy of reaction as well as the partial atomic charge on the phenolate oxygen showed that these two properties are highly correlated with the experimentally observed absorption capacities. Therefore, calculations can be used in a predictive manner to to assess the relative reactivities for several anions within the same family of ILs.

TABLE 2.3

PHYSICAL PROPERTIES OF DIFFERENT PHENOLIC ILS

IL	η [cPa][a]	d [g cm^{-3}][a]	σ [s cm^{-1}][a]	T_d [°C][b]
[P_{66614}][4-Me-Pho]	392.7	0.894	2.561	238
[P_{66614}][4-MeO-PhO]	253.4	0.919	4.210	217
[P_{66614}][4-H-PhO]	246.7	0.896	3.001	245
[P_{66614}][4-Cl-PhO]	376.5	0.949	5.680	277
[P_{66614}][4-CF_3-PhO]	286.4	0.968	3.800	259
[P_{66614}][4-NO_2-PhO]	984.3	0.958	4.700	292
[P_{66614}][3-Cl-PhO]	223.2	0.931	3.940	270
[P_{66614}][2-Cl-PhO]	378.3	0.925	1.825	299
[P_{66614}][2,4-Cl-PhO]	472.5	0.966	2.179	302
[P_{66614}][2,4,6-Cl-PhO]	672.1	1.009	1.560	341
[P_{66614}][3-Me-PhO]	335.1	0.893	2.951	221
[P_{66614}][2-Me-PhO]	415.5	0.900	2.408	243
[P_{66614}][2,4-Me-PhO]	334.1	0.901	1.653	205
[P_{66614}][2,6-Me-PhO]	371.3	0.909	2.552	189
[P_{66614}][4-iPr-PhO]	388.2	0.906	1.612	250
[P_{66614}][4-tBu-PhO]	585.8	0.887	0.812	255
[P_{66614}][3-MeO-PhO]	374.8	0.937	3.840	258
[P_{66614}][3-NMe_2-PhO]	512.1	0.916	0.891	233
[P_{66614}][1-Naph]	1077	0.929	1.019	294
[P_{66614}][2-Naph]	878.4	0.930	1.010	284

[a] Determined at 23 °C.

[b] Determined by TGA under N_2 atmosphere.

Table reproduced with permission from ref [125]. Copyright 2012 Wiley.

2.2.9 Quantifying Reactivity Trends Using Quantum Calculations

The use of *ab initio* calculations has proven to be invaluable in understanding the behavior of IL-CO_2 reactions for both AHAs and superbase ILs [126]. Calculated enthalpies of reaction only considering the anion and CO_2 have often produced values in close agreement with experiment, which provides an easy way to assess the reactivity of a given anion. Wang *et al.* calculated an enthalpy of reaction of -56.4 kJ mol^{-1} for $[P_{66614}][4Triaz]$, which is in excellent agreement with the experimental value of -50.0 kJ mol^{-1} obtained from in-situ IR spectroscopy, indicating that the quantum calculations are able to accurately model these systems [124]. The calculated values for the enthalpy of reaction tend to trend well with experimentally observed absorption capacities as well as the required desorption temperatures, which provides a simple means to assess the chemical reactivities of different ILs [6, 124–126]. Furthermore, the calculations have demonstrated that the basicity of the anion can be used to tune the enthalpy of reaction of superbase ILs [9, 124]. More basic anions will bond CO_2 more strongly, however, the basicity of the anion also affects the thermostability of the IL and more basic anions will reprotonate at elevated temperatures. Therefore, the trade off between binding strength and thermostability requires a delicate balance for successful performance in an industrial application.

Teague *et al.* performed a series of quantum chemical calculations to develop structure property relationships for superbase ILs and to evaluate how various substituents to phenolate and cyclohexanate rings, which are shown in Figure 2.9, affect the CO_2 binding strength [9].

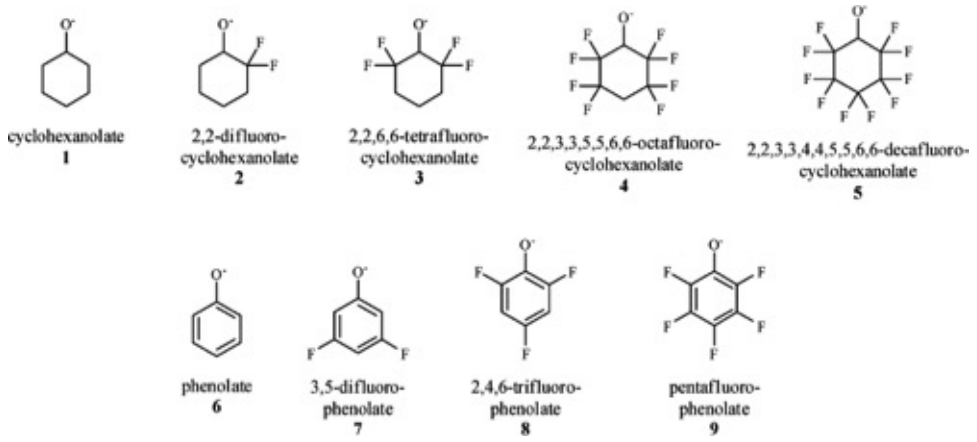

Figure 2.9. Structures of phenolate and cyclohexanate anions investigated by Teague *et al.* [9]. Figure reproduced with permission from ref [9]. Copyright 2010 American Chemical Society.

Enthalpies of reaction were calculated by optimizing the geometries of CO_2, the anions, and the anion-CO_2 complexes. Dispersion interactions which have previously been shown to be important in IL-CO_2 systems were modeled by using resolution of identity standard DFT augmented with a damped empirical dispersion using various levels of electronic structure theory. All of the calculations showed the same reactivity trends when comparing the different anions, although different methods and basis sets gave different values of computed properties. Qualitative trends between different ILs can be obtained using relatively cheap basis sets, however, higher levels of electronic structure theory are required to obtain quantitative results. These calculations indicated that the addition of electron withdrawing fluorine groups to the anion ring structure reduces the CO_2 binding strength and results in larger O-C distances and O-C-O angles. Teague examined the ability of the anion basicity to act as a descriptor for the CO_2 reactivity. The basicities of the anions were represented by their proton affinities and the partial atomic charges on the oxygen binding sites,

which were obtained through natural bonding orbital (NBO) analysis and calculated Mulliken charges. The proton affinities showed excellent correlation with the calculated reaction energetics within a group of anions (either phenolate or cyclohexanate), which was much better than the trend obtained when comparing both groups of anions. The energetics of reacting anions with CO_2, without considering the cation in the reaction, trend well with the charge on the CO_2 binding sites for both groups of anions (phenolates and cyclohexanates). This trend is fortunate because it allows different anion groups to be compared even if they have different binding sites (N vs. O).

Mercy *et al.* tried to gain additional insights from calculations of gas phase reaction energetics by including the cation in the calculations [10, 127], because it is known that many CO_2 reactive anions have different CO_2 absorption capacities when paired with different cations [16, 98]. Reaction energetics of CO_2 with 4 different superbase ILs consisting of $[P_{3333}]^+$ paired with $[Benzim]^-$, $[3Triaz]^-$, $[4Triaz]^-$, and $[Bentriz]^-$, which are shown in figure 2.10, were calculated using DFT.

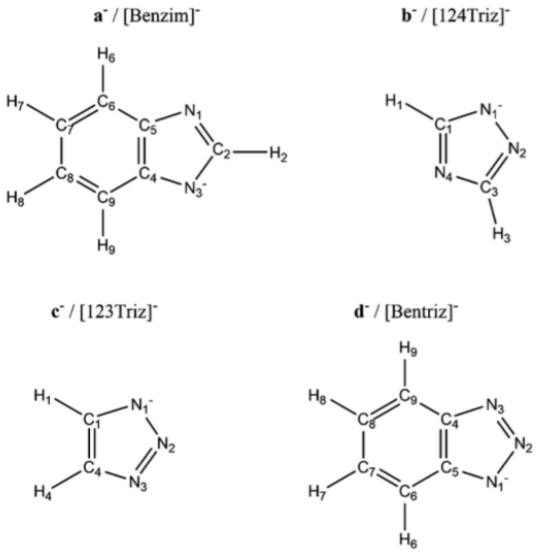

Figure 2.10. Structures of superbase anions investigated by Mercy *et al.* [10]. Figure reproduced with permission from ref [10]. Copyright 2015 Royal Society of Chemistry.

The gas phase enthalpies of reaction were calculated in two ways: first only the anions were considered in the reaction, and then the cation was also included. The calculated reaction enthalpies when only the anion was considered correlated well with experimental CO_2 absorption capacities, the carbamate bond length, and the amount of charge transferred from the anion to the COO^-. When the cation was included, however, the calculated reaction enthalpies were less exothermic than those calculated for the anion only reaction scenarios, and the trend between the absorption capacity and the enthalpy of reaction was lost. Additionally, the ionic pair reaction model model gave shorter carbamate bond lengths and smaller CO_2 angles than the anion only reaction model. Cations clearly do influence the CO_2 absorption capacity, however, it is not clear how to properly account for this effect when performing gas phase reaction calculations. Inclusion of the cation in the reaction calculations creates

difficulties because it is hard to determine an optimized geometry for a cation-anion pair, which makes it challenging to sample thermodynamically relevant geometries of a cation-anion pair and to obtain trustworthy energies and free energies of reaction.

While a great deal of experimental and simulation work has focused on tuning the reaction enthalpy to optimize CO_2 absorption, the entropy of reaction can be equally important. Luo *et al.* introduced a novel way to improve IL performance whereby absorption of CO_2 into anion functionalized ILs is driven by an entropic effect in addition to the enthalpic effect [11]. Using entropic effects to drive the absorption is desirable because it decreases the energy requirement for the desorption of CO_2, which helps improve the energy efficiency of the absorption cycle. ILs consisting of methylbenzoate and nicotinate anions (shown in Figure 2.11) paired with $[P_{66614}]^+$ will absorb CO_2 due to an entropic driving force caused by intermolecular hydrogen bonding interactions. While the $[P_{66614}]$[p-AA] IL has a higher absorption capacity than $[P_{66614}]$[o-AA], the absorption enthalpies calculated at the B3LYP/6-31++G(p,d) level of theory for $[P_{66614}]$[p-AA] and $[P_{66614}]$[o-AA] are -41 and -56 kJ/mol, respectively. These calculations indicate that entropy can be an important factor governing the free energy of reaction. Although hydrogen bonding can help drive the reaction entropically, the increase in viscosity due to intramolecular hydrogen bonding remains a challenge.

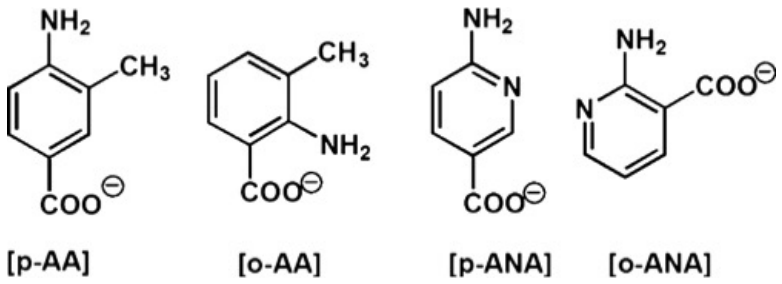

Figure 2.11. Structures of anions which demonstrate entropically driven reactivity investigated by Luo *et al.* [11]. Figure reproduced with permission from ref [11]. Copyright 2014 American Chemical Society.

Computations have done an excellent job in estimating reactivity trends and aiding experimental design of ILs, but the CO_2 reaction equilibria necessary for process design is very challenging to calculate. CO_2 absorption isotherms can be calculated from the free energy of reaction, but determining reaction free energies in the condensed phase is nontrivial due to the expense of quantum calculations using an explicit solvent. However, much of the computational burden can be removed using various approximations. Firaha *et al.* [128] calculated the free energy of reaction for a series of AHA and superbase ILs using COSMO-RS. Geometry optimizations were performed using an implicit solvent to obtain solvated geometries of the reacted and unreacted anions. The free energy of reaction was then determined by calculating the vibrational frequencies of the the solvated anions and product anions. This implicit solvation method gave significant improvement over the use of gas phase geometries to calculate reaction free energies. As shown in Table 2.4, the calculated reaction free energies using the solvated geometries were in qualitative agreement with experimental CO_2 solubilities, and in many cases quantitative agreement with free energies of reaction obtained by fitting isotherm models to experimental data.

TABLE 2.4

COMPUTED AND EXPERIMENTAL PROPERTIES

Anion	$\Delta_r H^{[a]}$	$\Delta_r G^{[a]}_{calcd}$	$\Delta_r G^{[b]}_{exp}$	Abs. cap.[c]
$[Inda]^-$	-63	-26	-16	0.92
$[BnIm]^-$	-67	-23	-13	0.91
$[6\text{-Br-BnIm}]^-$	-57	-11	-9	0.9
$[2\text{-CN-Pyr}]^-$	-47	-7	-6	0.88
$[3\text{-}CF_3\text{-Prz}]^-$	-52	-9	-6	0.87
$[1,2,4\text{-Tri}]^-$	-60	-9	-4	0.76
$[2\text{-}SCH_3\text{-BnIm}]^-$	-48	1	-3	0.72
$[3\text{-Me-5-}CF_3\text{-Prz}]^-$	-49	3	-2	0.63
$[1,2,3\text{-Tri}]^-$	-53	-1	2	0.25

[a] Computed-gas-phase enthalpy ($\Delta_r H$) and solvated Gibbs free energies ($\Delta_r G_{calcd}$) and [b] experimental Gibbs free energies ($\Delta_r G_{exp}$) at 298.15 K for the reaction of anions with CO_2. All energies are in kJ mol^{-1}. The experimental equilibrium constants from ref [7] were used to calculate $\Delta_r G_{exp}$ at 293 K.

[c] Absorption capacity in mol CO_2 per mol IL. The data was interpolated to a pressure of 0.9 bar from the two nearest experimental points in refs [6, 7].

Firaha *et al.* [128] concluded that a suitable IL for CO_2 capture needs to have a high absorption capacity while minimizing the necessary energy to desorb the CO_2 and regenerate the IL. Candidate ILs should therefore have a Gibbs free energy of reaction between -32 and 16 kJ mol^{-1}. Calculated free energies of reaction generally correlate in a quadratic fashion with the CO_2 absorption capacities, and therefore through simple frequency calculations on gas phase and solvated geometries the free energy of reaction, and thus the predicted absorption capacities, can be estimated.

Calculated reaction energetics have trended well with experimental CO_2 absorption capacities for AHAs, superbase ILs, and phenolic ILs. However, it is worth mentioning a word of caution. For all of these ILs, researchers initially believed that CO_2 would bind to the anions in the same way for different anions within the same family of ILs. However, more recent experimental and computational studies have shown that many of these systems do not react with CO_2 according to the originally proposed reaction mechanisms. Spectroscopy studies combined with DFT calculated reaction mechanisms from Gohndrone *et al.* [129] have shown that certain ILs consisting of phosphonium cations paired with azolide anions will bind CO_2 to the cations rather than the anions. The reaction chemistries in these systems are further complicated by the fact that the binding preference can depend on the temperature. A similar study by Lee *et al.* [130] found that the same behavior occurs in ILs consisting of phosphonium cations paired with phenolate anions. These examples help illustrate the point that calculations should not be interpreted separately from experimental results. Spectroscopic analysis plays a very important role in assessing the reaction chemistries of IL-CO_2 systems. While many calculated reaction energetics trend well with experimental absorption capacities when comparing different anions and different anion substituents, these results are often serendipitous and do not necessarily reflect the underlying chemistry. Therefore, researchers must use caution in order ensure that their models are accurate when performing computational

studies on CO_2-reactive ILs due to their complex reaction chemistries.

2.3 Other Advantages of Simulations

2.3.1 Physical Solubility Calculations

While the vast majority of computational work on CO_2-reactive ILs has focused on calculating reaction energetics and thermodynamic equilibrium or understanding observed viscosity trends, simulations have much more to offer in designing CO_2-reactive ILs. One area where simulations are aptly suited to aid in IL design is in calculation of physical gas solubilities. In many of the proposed applications of CO_2-reactive ILs, other gases that are present could have adverse effects on the IL performance. It is therefore important to have an understanding of IL affinity for different species and to know whether or not the IL will selectively absorb CO_2 in the presence of other gases such as N_2, O_2, H_2O, and CH_4. When solutes do not undergo chemical reactions in the solvent environment, the physical solubilities can be calculated by using Monte Carlo (MC) simulations, free energy methods in CMD simulations, or through the use of implicit solvent quantum calculations. Each of these methods has associated strengths and weaknesses in understanding the behavior of IL systems.

Some of the earliest solubility calculations on IL systems were performed using CMD simulations to investigate solute-solvent association energetics [131, 132]. In general, these studies have shown the the solute polarity and its ability to form hydrogen bonds is the primary factor that governs solute-IL interactions. Subsequent CMD simulations sought to quantify solubility through calculation of relative solute free energies. One of the earliest studies examining the solubility of various solutes in ILs was performed by Lyndon-Bell *et al.* [133] The excess chemical potentials of various polar and nonpolar solvents in [dmim][Cl] were calculated using a two step

approach. First, Widom particle insertion was used to calculate the excess chemical potential of a small LJ molecule. Following the Widom particle insertion, thermodynamic integration was performed for a series of alchemical transformations of the LJ molecule into the different solvent molecules. While there were no measured excess chemical potentials to compare with, the calculated excess chemical potentials were in qualitative agreement with experimentally measured solubilities. This study proved that thermodynamic integration provides a reliable and robust means to access free energy changes in IL systems. At the same time, Deschamps *et al.* [132] used CMD free energy methods to calculate gas solubilities in [bmim][PF_6] and [bmim][BF_4]. An important finding of this study was that charges must be added to the force field models of neutral molecules in order to accurately model quadrapole moments, and thereby obtain free energies that are consistent with experimental results.

CMD free energy methods such as Widom insertion, free energy perturbation, thermodynamic integration, and the Bennett Acceptance Ratio (BAR) provide means whereby the infinite dilution free energy of solvation can be determined from CMD simulations and subsequently used to calculate Henry's law constants [12, 111, 134]. Liu *et al.* [12] used BAR to calculate solvation free energies and Henry's law constants for various solutes in [emim][Tf_2N]. The calculated solvation free energies and Henry's law constants shown in Figure 2.12 were in qualitative agreement with experiment and in some cases quantitative agreement. One of the primary benefits of using CMD simulations is that they provide understanding of not only physical solubility but also its molecular origin, which helps researchers decide which chemical functionality will give the best performance in a given application.

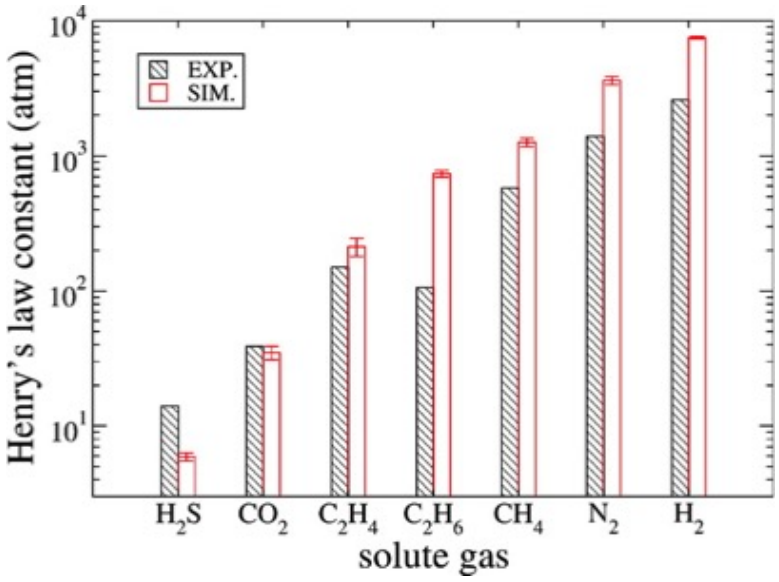

Figure 2.12. Calculated Henry's law constants for various gases in [emim][Tf_2N]. Figure reproduced with permission from ref [12]. Copyright 2014 American Chemical Society.

MC simulations are another popular method for calculating gas solubilities in ILs. Solubility is calculated in a rigorous manner in MC simulations by equilibrating liquid and vapor phases such that the chemical potential of the solute is equal in the two phases. Shah *et al.* [135] calculated Henrys law constants for H_2O, O_2, C_2H_6, C_2H_4, CH_4, O_2, and N_2 in [bmim][PF_6] with Monte Carlo simulations using both test particle insertion and the expanded ensemble method. In the test particle insertion method, a non-interacting solute test particle is placed in a random orientation at random positions within previously generated configurations and the solute-solvent interaction energy is computed and used to determine the Henry's law constant. In the expanded ensemble method, the interaction between solute and solvent molecules is linearly scaled by a coupling parameter, λ, which helps to increase the acceptance of swap moves from the low density vapor phase to the high density liquid phase.

The expanded ensemble simulations allowed translation, rotation, volume, swap, and λ adjustment moves. The simulations started by placing a noninteracting solute molecule into a random place within the box containing the ionic liquid. MC trial moves were then performed until the solute reached the uncoupled state where λ=0, after which a new test particle was inserted into the system. A uniform sampling of the λ space was accomplished by using the Wang-Landau method [136, 137]. The chemical potential was then calculated based on the probabilities of visiting the different end states (either complete interaction or no interaction between the solute and the solvent). The simulations were able to predict the correct trend in Henry's law constants between the different solutes, but the calculated Henry's law constants for all tested solutes were higher than the experimental values. Similar to the findings of Deschamps *et al.* [132], it was necessary to add a quadrapole moment to the ethane and ethene force fields in order to observe the correct selectivity trend of these species. The partial molar enthalpy and entropy of solvation for H_2O and CO_2 were calculated by performing simulations at different temperatures. The calculated partial molar enthalpies of solvation were larger than the experimental values. Neither test particle insertion nor the expanded ensemble approach were able to capture the experimentally observed increase in O_2 solubility with increasing temperature. Henry's law constants calculated using the test particle insertion method were found to depend on the system size. In general, the expanded ensemble results showed better agreement with experiment and no system size dependence.

One of the main benefits of using MC simulations for solubility calculations is that it provides a means to calculate mixed gas solubilities, which can be extremely difficult to measure experimentally [65]. Understanding mixed gas solubilities is of critical importance in understanding absorption selectivity, which can have significant implications for the energy requirements of a given separation. For instance, in post combustion CO_2 capture, if the IL absorbs species such as N_2 or O_2, it will result

in high parasitic energy requirements to compress these species to high sequestration pressures. Shi *et al.* [138] calculated both pure component and mixed gas absorption isotherms of O_2, N_2, and SO_2 in [hmim][Tf_2N]. Pure gas isotherms were calculated using continuous fractional component bias Monte Carlo (CFC MC), which improves the acceptance of swap moves between phases through scaled solute-solvent interactions that help to avoid unfavorable high energy insertions into dense systems. The simulations were able to reproduce the experimental isotherms for the pure components. Additionally, mixed gas solubilities were calculated using Gibbs ensemble MC simulations and the ability of regular solution theory to model mixed gas solubilities was evaluated. The simulations showed that the mixed gas solubilities behave ideally as if the solutes did not interact. This result was contradictory to solubility data at the time [139], but has since been confirmed experimentally [140]. MC simulations have also correctly predicted that the solubilities of sparingly soluble gases in ILs tend to increase with increasing temperature [141].

Another popular method for calculating physical gas solubilities is to perform implicit solvent quantum chemical calculations. The free energy of solvation can be calculated by taking the difference in free energy between the gas phase optimized geometry and the solvated optimized geometry. One popular way to perform these calculations is the use of COSMO-RS [108, 109, 128, 142, 143]. Implicit solvation calculations are quite useful for screening large candidate sets because the calculations are easier and cheaper to run in a high throughput manner than MC simulations or CMD free energy methods that require specific tuning of simulation parameters for each different system as well as accurate force field models for all considered species. Zhang *et al.* used COSMO-RS to calculate Henry's law constants for CO_2 in 408 different ILs that physically absorb CO_2 [142]. The model was first verified by comparison with experimental data and equations of state for CO_2. The calculations showed that the Henry's law constants are sensitive to the anions while

being mostly insensitive to the cations. However, increasing the cation alkyl chain lengths was found to decrease the Henry's law constants, which was in agreement with other studies [143]. After performing the screening, the best candidate anion ($[FEP]^-$) was paired with three different cations and experimental CO_2 absorption isotherms were measured for these ILs. The experimental results confirmed that the CO_2 solubility is improved by using the proposed $[FEP]^-$ anion. Although this study demonstrates the screening potential of COSMO-RS, the method does have some limitations. While the experimental and calculated Henry's law constants were in excellent agreement at room temperature, the temperature dependence of the calculated Henry's law constants did not have the same slope as the experimental Henry's law constants. COSMO-RS is an excellent tool for efficiently screening large sets of candidate solvents, but it can have problems for accurate quantitative prediction.

Simulations have proven to be a powerful tool for predicting physical gas solubilities. Understanding the physical solubilities of species present with CO_2 is an important aspect of designing better CO_2-reactive ILs. CMD free energy methods are useful for both calculating solubilities and understanding the molecular origins of solubility. MC simulations allow mixed gas solubilities that are rarely reported in literature to be calculated in a direct and rigorous manner. Implicit solvation models provide a simple means to estimate physical solubilities and are aptly suited to screen extensive sets of candidate solvents. Simulations are a great design tool to help understand how the IL and solute chemical structures govern the physical solubilities of various solutes in CO_2-reactive ILs.

2.3.2 IL-Water Mixtures

Understanding the behavior of IL-water mixtures is of fundamental importance to CO_2 separations and other IL applications where water is present. The interactions between water and CO_2-reactive ILs are crucial as many ILs are known to be

hygroscopic and they will absorb significant amounts of water [144–146]. Water effects not only the physical properties of ILs [147–150], but it can also change reaction chemistries and CO_2 absorption capacities [7, 83, 96, 104, 121, 151, 152]. Computational methods have been extremely useful in understanding how water affects IL performance.

CMD simulations have been used extensively to investigate excess molar properties and the behavior of IL-water mixtures [153, 154]. In general, the hydrophobic/hydrophilic nature of the anion determines the miscibility of the mixtures. Many ILs have demonstrated an increase in system dynamics and a decrease in viscosity upon the addition of water [7, 152, 153], although some ILs show the opposite behavior [155]. Initial CMD simulation studies on IL-water mixtures found that the increase in IL system dynamics from the addition of water was primarily attributed to the fact that water decreases counterion association, thereby allowing ions to diffuse more freely [154, 156, 157]. Using a series of CMD simulations, Feng *et al.* [149] found that water forms strong interactions primarily with anions. These CMD simulations showed that anions which interacted strongly with water would form persistent associated clusters with water, whereas when the anions interacted weakly with water, the water would self aggregate [149]. These studies demonstrated that water can drastically alter IL behavior and that it is difficult to assess the impact of water a priori.

The majority of simulation literature on IL-water mixtures has focused on a few select classes of ILs, namely the imidizolium family of ILs [149, 156, 158–161], and there have only been a few simulation studies on mixtures of water and CO_2-reactive ILs. Thompson *et al.* [155] used a combination of experiments and CMD simulations to study interactions with CO_2 and H_2O for a series of ILs having a $[P_{4444}]^+$ cation paired with a series of $[3Triaz]^-$ anions functionalized at the 4-position with various electron donating and electron withdrawing groups. The CO_2 absorption

capacities for the ILs varied from 0.07-0.4 mol CO_2/IL at 30 °C and 1 bar, depending on the substituent. The ILs with electron donating groups had lower thermal decomposition temperatures as did the ILs with alkyl substituents on the anions. Steric hindrance and the addition of electron withdrawing groups decreased the CO_2 absorption capacities. When water was added to these ILs, the absorption capacities did not change, however, the viscosities of the unreacted ILs increased and the CO_2 reaction mechanism changed from a a carbamate formation to bicarbomate formation with some possible ylide formation. Partial charges obtained using the CHarges from Electrostatic Potentials using a Grid-based (CHELPG) method and calculated interaction energies of CO_2 and H_2O with the ring nitrogens of $[3Triaz]^-$ showed that interactions with H_2O are more favorable than interactions with CO_2, and that the preferred nitrogen binding site is the one with the most negative charge.

CMD simulations by Sheridan *et al.* for a series of ILs consisting of $[P_{2228}]^+$ paired with $[2CNpyr]^-$, $[3Triaz]^-$, $[PhO]^-$ anions showed that the interactions with water depend primarily on the ability of the anions to form stable hydrogen bonds with water [162]. The water affinity estimated by calculated Henry's law constants showed that water is stabilized through hydrogen bonding interactions with anions, and that these interactions tend to increase as the anion atoms become more negatively charged. Simulations of both dry ILs and 1:1 water/IL mixtures showed that water can drastically alter the IL ion dynamics. Water tends to form the first solvation shell around the anions, which reduces the counterion association and causes the ion diffusivities to nearly double in the $[2CNpyr]^-$ and $[3Triaz]^-$ ILs, which is similar to previous findings for other ILs [154, 156, 157]. Although the added water decreased the counterion association in the $[PhO]^-$ IL, the $[PhO]^-$ anions associated through hydrogen bonds with water, and the result was that the system dynamics were virtually unaffected by the addition of water. It is possible that this result is due to the fact that no chemical reactions were considered in the CMD simulations.

Recent experimental work has shown that ILs with phenolate anions can undergo reactions in the presence of water [123, 130]. For this reason, Brehm *et al.* [99] suggested that AIMD simulations are the appropriate way to model IL-water mixtures. However, it is not yet possible to accurately assess system dynamics from AIMD simulations due to the limited system sizes and timescales that can be simulated. It is interesting to note that while both Thompson *et al.* [155] and Sheridan *et al.* [162] examined ILs consisting of phosphonium cations paired with $[3Triaz]^-$, the effects of water were different in each study. Thompson found that the addition of water resulted in slower ion dynamics [155], whereas Sheridan found that added water causes the ion dynamics to increase [162]. This observation suggests that the effects of water on IL dynamics are not only sensitive to the anion, but also to the cation it is paired with and the amount of water absorbed.

2.3.3 IL Toxicity

Toxicity presents a major challenge in the design of ILs for industrial applications. While a great deal of physical and chemical data exists for a wide range of ILs, toxicity data remains scarce [163]. The unknown toxicity of many ILs is one of the largest barriers to the widespread application of ILs in industrial processes [146]. Due to their high thermal and chemical stabilities, ILs can persist for long times if they are released into the environment and therefore, understanding the mechanisms which cause IL toxicity is important. The fact that ILs have such low vapor pressures and that many ILs are colorless means that they may go undetected if they are released into the environment. While there have been biodegradability [164–171] and toxicity [172–175] studies for some of the most commonly researched ILs, the high rate at which new ILs are designed and synthesized means many ILs have no toxicity or biodegradability data. Studies on imidizolium based ILs have shown that the IL toxicity tends to increase with increasing alkyl chain lengths on the imidizolium cation

[167]. Interestingly, some researchers have proposed using the toxicity of imidizolium ILs to selectively target and disrupt cancer cells [176]. The potential risk of chemical release into the environment makes it important to understand how different tuning of cations and anions affects the IL toxicity.

CMD simulations provide a convenient platform whereby the toxicity and the toxicity mechanisms of ILs can be assessed prior to synthesis and experiment. Bingham *et al.* [177] pioneered the use of CMD simulations to elucidate the toxicity mechanism for a class of imidizolium ILs. CMD simulations were run to investigate how ILs made from $[bmim]^+$ paired with anions ranging from hydrophilic to hydrophobic in the order $[Cl]^-$, $[PF_6]^-$, and $[Tf_2N]^-$ interact with lipid bilayer membranes. The simulations showed that in all cases, the $[bmim]^+$ hydrophobic alkyl tails inserted into the lipid bilayer and associated with the hydrophobic lipid tails, while the imidizolium ring associated with the polar lipid head groups. The $[Cl]^-$ anions remained in an aqueous environment, whereas the $[PF_6]^-$ anions formed a thin layer on the lipid bilayer surface. With $[bmim][Tf_2N]$, the counter ions precipitated into globules in solution while some of the $[emim]^+$ cations inserted into the bilayer and some of the $[Tf_2N]^-$ anions reassociated with the inserted cations. Bingham found that interaction of the ions with the bilayer cause large fluctuations in the compressibility modulus of the bilayer, which may contribute to morphological changes in the bilayer.

Yoo *et al.* [13] followed the work of Bingham and used a combination of molecular dynamics simulations and fluorescence microscopy studies on synthetic lipid bilayer membranes in order to investigate the toxicity mechanisms of imidizolium ILs. The experiments showed that the toxicity of 1-n-alkyl-3-methylimidazolium ($[C_nmim]^+$) based ILs increases with increasing alkyl chain lengths on the imidizolium cation, which was in agreement with previous studies [167]. Similar to Bingham's results, the CMD simulations showed that the hydrophobic cation alkyl chain will spontaneously insert deep into the lipid bilayer while the imidizolium ring will interact with the

lipid head groups, whereas the hydrophilic anions such as $[Cl]^-$ remain in the aqueous environment surrounding the lipid bilayer. Even more hydrophobic anions such as $[Tf_2N]^-$ only showed modest interactions with the lipid bilayer occasionally inserting and reassociating with inserted cations. The amount of cation insertions into the lipid bilayer increased with increasing IL concentration, which also caused the fluctuations in the lipid bilayer thickness to increase as shown in Figure 2.13. The disruptions in the lipid bilayer thickness may eventually lead to sufficient bilayer disruption to result in the death of cells. Potential of mean force simulations for imidizolium insertion into the lipid bilayer calculated free energies of insertion of -27 and -37 kJ mol^{-1} for $[bmim]^+$ and $[dmim]^+$, respectively, further indicating that cations with longer alkyl chain lengths are more likely to insert into the lipid bilayer.

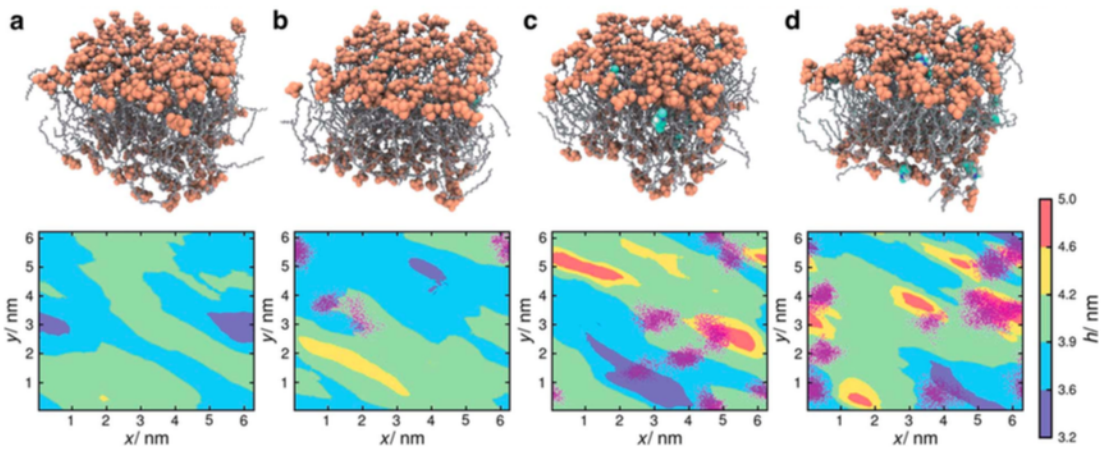

Figure 2.13. Snapshot of configurations (above) and bilayer thickness contour plots (h)(below). The contour plots were averaged over the last 20 ns of the simulation. (a) The hydrated lipid bilayer, (b) 16 mM [bmim][Cl], (c) 50 mM [bmim][Cl], (d) 100 mM [bmim][Cl]. Locations of inserted cation atoms from each frame are indicated by the dots in magenta. Figure reproduced with permission from ref [13]. Copyright 2014 Royal Society of Chemistry.

Further course grained simulations by Yoo *et al.* showed that when the alkyl chains are sufficiently long (n=10), the cations will self assemble into vesicles that will adsorb to the lipid bilayer surface causing the bilayer to buckle and bend [178]. The morphological changes in the lipid bilayer induced by ILs is thought to be the primary cytotoxicity mechanism of imidizolium ILs. CMD simulations are able to demonstrate on a molecular level how ILs disrupt lipid bilayer membranes. Understanding how IL structure relates to toxicity allows researchers to design ILs with lower toxicity. Also, knowing how the ions interact with the membrane could allow researchers to implement a mechanism to inhibit cell disruption by ILs.

2.4 Outstanding Research Issues

Significant advances have been made in applying CO_2-reactive ILs to CO_2 separations. Several ILs have been synthesized adding reactivity to either the anions or cations. Researchers have demonstrated that the reactivity of the ILs can be tuned between a physical absorption and strong chemical absorption by functionalizing the ions. Many of the initial barriers in IL design such as the high viscosity have been overcome by using a combination of simulations and experiments to develop structure property relationships, whereby the physical properties can be understood in terms of the chemical structures. However, there remains significant room for improved design and a lot of work has yet to be done before ILs can be applied for industrial scale CO_2 capture from point source emitters.

Several opportunities exist where computations may yet aid in the design of CO_2-reactive ILs. One issue is the question of IL lifecycle. While most experimental studies on CO_2 absorption in reactive ILs have shown that the absorption process can be performed several cycles with little or no loss of efficiency, ILs have not yet been applied extensively in pilot-scale operations to assess their lifecycle. In order for ILs to be used in place of current amine technologies, researchers will have do

demonstrate that ILs solvents will work efficiently with solvent replacement costs that are similar to or better than amines. Simulations can be aid in understanding IL life cycle by assessing different reaction pathways which may eventually lead to deactivation of the IL. As mentioned previously, simulations can also be used to assess how the structure of ILs relates to their toxicity. In order to perform efficiently in CO_2 separations, ILs will need to selectively absorb CO_2 over other gases that are present. Simulations have already proven their use in predicting the solubilities of different gases in ILs and will aid in understanding absorption selectivity. Quantum chemical calculations can be used to predict reaction pathways and associated free energies, thereby allowing kinetic reaction rates to be assessed and compared within a family of candidate ILs. It is possible that ILs will be mixed with cosolvents to improve their performance in CO_2 separations. Both CMD and MC simulations can be used to predict mixtures properties, which can help identify optimal cosolvents. While many issues remain in designing CO_2-reactive ILs, simulations have demonstrated their ability to aid in overcoming these problems, and as such, they will continue to aid experimentalists in designing better ILs.

2.5 Outlook

Molecular simulations have made significant contributions to the present understanding of IL-CO_2 chemistries. Simulations have acted as a tool to understand the behavior of CO_2-reactive ILs from the earliest design stages. In some of the first computational work on CO_2-reactive ILs, *ab initio* calculations on simple reactions between anions and CO_2 gave reaction energetics that helped identify potentially reactive species. CMD simulations helped identify the hydrogen bonding mechanisms responsible for large viscosities of first generation of CO_2-reactive ILs made from amine functionalized imidizolium cations. This molecular level understanding helped lead to the design of AHA ILs and superbase ILs, both of which alleviated the viscos-

ity problem while improving the CO_2 absorption capacity in a tunable way. CMD has provided a reliable and relatively cheap means to investigate IL structure and dynamics. These simulations have helped researchers assess whether or not a candidate IL will have acceptable physical properties for industrial application prior to synthesis. Furthermore, CMD simulations provide a convenient platform for investigating the toxicity mechanisms of ILs for which no experimental toxicity data exist. Implicit solvation quantum chemical calculations such as COSMO-RS have successfully been applied to calculate gas solubilities for a broad range of solutes in various known and proposed ILs, which provided an efficient means to screen large sets of candidate ILs for the most promising CO_2 capture properties. MC simulations have further extended the understanding of gas solubilities in ILs allowing both pure and mixed gas physical solubilities to be calculated, which are difficult and time consuming to measure experimentally. The development of CO_2-reactive ILs for industrial scale CO_2 capture has come a long way since the first investigations of their potential use, and along the way, simulations have aided in designing ILs and understanding their properties.

The synergistic feedback between simulation and experiment will continue to advance the understanding and design of new CO_2 capture ILs. Clearly, these systems have complex chemistries and large design spaces, which makes it unlikely to find optimal ILs through a trial and error process. While the available computational chemistry methods have provided valuable insights into IL behavior, many of the molecular simulations suffer from various assumptions regarding different aspects of the CO_2 absorption process. For instance, understanding how the solvation environment affects the reaction chemistries has not yet been assessed in a rigorous manner. After initial screening of candidate ILs using the various methods described in this review, different levels of theory such as AIMD, QM/MM hybrid methods, and reactive Monte-Carlo methods may provide experimental chemists additional information on

how the liquid environment affects the reaction process so that they may design better ILs. ILs have been, and remain, promising candidates for CO_2 capture processes and they will likely play a key role in future efforts to mitigate CO_2 emissions.

2.6 Abbreviations Used in this Chapter

TABLE 2.5:

FULL CHEMICAL NAMES FOR CHEMICAL ABBREVIA-TIONS USED IN THIS CHAPTER

Abbreviation	Full Chemical Name
$[P_{2228}]^+$	triethyl-octyl-phosphonium
$[P_{3333}]^+$	tetrapropyl-phosphonium
$[P_{4444}]^+$	tetrabutyl-phosphonium
$[P_{66614}]^+$	trihexyl-tetradecly-phosphonium
$[P_{222(1O1)}]^+$	triethyl(methoxymethyl)phosphonium
$[emim]^+$	1-ethyl-3-methyl-imidizolium
$[bmim]^+$	1-butyl-3-methyl-imidizolium
$[hmim]^+$	1-hexyl-3-methyl-imidizolium
$[dmim]^+$	1-dodecyl-3-methyl-imidizolium
$[Met]^-$	methioninate
$[Pro]^-$	prolinate
$[Gly]^-$	glycinate
$[Ac]^-$	acetate
$[TFA]^-$	trifluoroacetate
$[2CNpyr]^-$	2-cyanopyrrolide
$[3Triaz]^-$	1,2,3-triazolide
$[4Triaz]^-$	1,2,4-triazolide
$[Im]^-$	imidazolate
$[Inda]^-$	indazolide
$[BnIm]^-$	benzimidazolide
$[Pyr]^-$	pyradine

TABLE 2.5: *Continued*

Abbreviation	Full Chemical Name
$[PhO]^-$	phenolate
$[TFE]^-$	trifluoroacetyl
$[Naph]^-$	naphtholate
$[p\text{-}AA]^-$	4-amino-3-methylben- zoic acid
$[o\text{-}AA]^-$	2-Amino-3-methylbenzoic acid
$[p\text{-}ANA]^-$	6-amino- nicotinic acid
$[o\text{-}ANA]^-$	2-aminonicotinic acid
$[PF_6]^-$	hexafluorophosphate
$[BF_4]^-$	tetrafluoroborate
$[Cl]^-$	chloride
$[Tf_2N]^-$	bis(trifluoromethylsulfonyl)imide
$[FEP]^-$	tris(pentafluoroethyl)trifluorophosphate
$[pyrr]^-$	pyrrolide
MEA	monoethanolamine
DEA	diethanolamine
DBU	(1,8-diazabicyclo-[5.4.0]-undec-7-ene

CHAPTER 3

FORCE FIELD PARAMETERIZATION

3.0.1 Parameterization Procedure

Force field Lennard-Jones parameters and intramolecular potentials for all of the simulations reported in this thesis were obtained using the Antechamber package in AMBER to assign atom types for AMBER potentials. All of the molecular dynamics simulations were performed using the GROMACS simulation software. The functional form in eq. 3.1 was used to describe both the intramolecular and intermolecular degrees of freedom. Note that the potential functional form varies between different CMD software packages so use caution when transferring parameters.

$$V = \sum_{bonds} \frac{K_r}{2}(r - r_0)^2 + \sum_{angles} \frac{K_\Theta}{2}(\Theta - \Theta_0)^2 + \sum_{dihedrals} K_\Phi[1 + Cos(n\Phi - \Phi_0)] + \sum_{impropers} \frac{k}{2}(\Theta - \Theta_0)^2 + \sum_{\text{atom i}} \sum_{i>j} 4\epsilon_{ij} \left[\left(\frac{\sigma_{ij}}{r_{ij}} \right)^{12} - \left(\frac{\sigma_{ij}}{r_{ij}} \right)^{6} \right] + \frac{q_i q_j}{4\pi\epsilon_0 r_{ij}} \tag{3.1}$$

Some of the dihedrals used the periodic functional form shown in eq. 3.1, while other dihedrals were modeled using the Ryckaert-Bellemans (RB) functional form shown in eq. 3.2

$$V_{rb}(\phi_{ijkl}) = \sum_{n=0}^{5} C_n(cos(\psi))^n \tag{3.2}$$

where ψ is equal to ϕ -180° with ϕ being the dihedral angle. The force field parameters listed in Appendix A indicate which form was used for each dihedral.

Bonds, angles, and dihedrals were parametrized based off of the atom type assignment [179–181]. Partial atomic charges were obtained using the restricted electrostatic potential fitting method [182] for an electrostatic potential grid calculated with Gaussian09 [183] using the Merz-Kollman scheme [184, 185]. The resulting partial atomic charges were then scaled by 0.8 as is commonly done when modeling ILs to give better agreement between simulated and experimental diffusivities and to account for charge transfer between counter ions in the liquid phase [186–188]. Partial charges for the phosphonium cations were calculated at the B3LYP/6-311++g(d,p) level of theory due to the large size of the molecules. The partial charges for the reacted and unreacted anions were calculated at the B3LYP/aug-cc-pvdz level of theory. Prior to the charge fitting, the molecular structures were optimized and frequency calculations were performed to ensure the geometries converged to stable minima of the potential energy surfaces having only positive real frequencies.

The force field for for the CO_2-reacted 2-cyanopyrrolide ($[2CNpyr{:}CO_2]^-$) was modified following the assignment of default AMBER parameters. The default bond length for the N-C bond between $[2CNpyr]^-$ and CO_2 was 1.35 Å while the bond length from the *ab initio* optimized structure was 1.56 Å. Additionally, the default AMBER parameterization had a CO_2 angle of 130° while the *ab initio* optimized structure had an angle of 135.6°. Therefore, a hand fit was performed to optimize the force field parameters involving the CO_2 moiety: the C-N bond, the CO_2 angle, and the dihedral terms involving the rotation of the CO_2 group. A similar procedure was used to modify the force field parameters involving the CO_2 group for the CO_2-reacted 1,2,4-triazolide anions.

The following procedure was used to fit the force field parameters involving the CO_2 group. First, a scan was performed where the value of the bond, angle, or

dihedral being fitted was varied and a single point energy was calculated for the given geometry. Then, the same scan was performed using the force field to calculate the energies of the same geometries with the energy contribution of the term being fitted removed from the total energy. Next, the difference in energy between the two scans was used to fit force constants for the given degree of freedom assuming the equilibrium geometry for the C-N bond and the CO_2 angle given by the *ab initio* optimized structures. The force field optimization changed the original force fields in the following ways: 1) the C-N bond length between CO_2 and the anion increased while the bond force constant decreased, 2) both the CO_2 equilibrium angle and force constant increased, 3) the dihedral energy barrier for the rotation of the CO_2 decreased.

CHAPTER 4

ANION DEPENDENT DYNAMICS AND WATER SOLUBILITY EXPLAINED BY HYDROGEN BONDING INTERACTIONS IN MIXTURES OF WATER AND APROTIC HETEROCYCLIC ANION IONIC LIQUIDS

4.1 Introduction

As discussed in the review of CO_2-reactive ILs in Chapter 2, understanding water-IL interactions is crucial for the successful application of CO_2-reactive ILs in post combustion CO_2 capture. Many ILs are known to have high water affinities, and consequently it can be difficult to remove water from an IL [144]. The absorbed water can have dramatic effects on both the physical and chemical properties of an IL[7, 151, 189]. Several researchers have found that even a small amount of water can drastically reduce IL viscosity [2, 147, 190, 191]. Experimental measurement of activity coefficients for water in ILs revealed that the coefficients depend on specific interactions between anions and water [192]. Furthermore, the hydrophobic/hydrophilic nature of the anion determines the IL water solubility. A cation paired with a hydrophilic anion can be completely miscible with water, whereas the solubility of water in ILs having the same cation paired with hydrophobic anions can be quite low[146, 189, 193]. Experiments have shown that water not only effects the physical properties of CO_2-reactive ILs, but it can also affect CO_2 reaction chemistries and absorption capacities [7, 121, 151, 152] The presence of water in CO_2 separation processes thus necessitates a fundamental understanding of the physical interactions between water and AHA ILs.

Molecular dynamics (MD) simulations have been used extensively in the IL community to provide molecular level detail on specific interactions in water/IL mixtures that give rise to bulk thermodynamic and transport properties. Simulations of water-IL mixtures showed that when water is added to ILs, the counterion association weakens resulting in reduced viscosity, which is consistent with experimental results [154, 156–158]. Voth and coworkers [149] have examined the effects of varying anions and imidizolium alkyl chain lengths on the liquid structure of water/IL mixtures. While the cation alkyl chain lengths affected the cation aggregation, the mixture behavior was more sensitive to the anion. Anions such as chloride interact strongly with water and form persistent microstructures. Water is less likely to form clusters in these ILs than in ILs that have anions which interact weakly with water. Brehm *et al.* [99, 100] used *ab intio* molecular dynamics (AIMD) simulations to investigate 1-ethyl-3-methylimidazolium acetate mixtures. They observed strong hydrogen bonding interactions between water and the electronegative oxygen atoms of the acetate anion, and occasionally, the anion would share a hydrogen from water to form acetic acid. The hydrogen bonding interactions can cause significant polarization of both the ions and water, and therefore, *ab initio* methods are preferred to study these systems. AIMD simulations, however, have high computational expense which greatly limits the system size and time scales that can be simulated. Therefore, although classical MD cannot account for breaking and formation of chemical bonds which may occur in IL-water mixtures, it provides the most suitable method to examine structure and dynamics with high statistical accuracy such that the simulation results are mostly independent of the starting configurations. The assumption of the present work is that these aprotic anions will remain stable in the presence of water.

In this work, MD simulations were performed to investigate physical interactions between water and AHA ILs. The ILs have a common triethyl-octyl-phosphonium cation ($[P_{2228}]^+$) paired with the anions 2-cyanopyrrolide ($[2CNpyr]^-$), 1,2,3-triazolide

([3Triaz]$^-$), and phenolate ([PhO]$^-$). The cation and anions are shown in Figure 4.1. These combinations were chosen to represent two classes of ILs that exhibit chemical binding of CO_2 [1, 7, 8, 130]. The effects of water on IL dynamics were investigated through calculation of self-diffusion coefficients. The liquid structures of the wet and dry systems were compared through calculation of both radial distribution functions (RDFs) and spatial distribution functions (SDFs). Hydrogen bonding analysis was performed to provide insights into the structure and dynamics of the wet ILs. The relative water solubilities in each IL were compared through the calculation of Henry's law constants for water.

4.2 Computational Details

4.2.1 Liquid Structure and Diffusivity

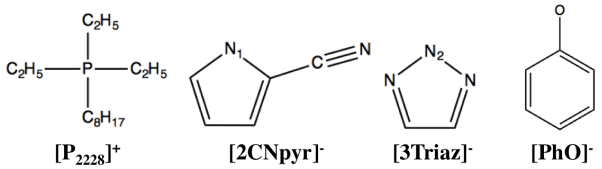

Figure 4.1. Ion Structures.

The liquid structure and dynamics of both wet and dry ILs were investigated through a series of MD simulations. A conventional class I force field was used in the simulations, the complete details of which are included in Appendix A. Both dry ILs and liquid mixtures of 1:1 mole ratio water/IL were simulated using GRO-

MACS version 4.5.5 [194–196]. Long range electrostatics were handled using particle mesh Ewald summation [197]. Long range corrections to the Lennard-Jones (LJ) interactions were applied when computing the energy and pressure.

Initial structures of 150-200 cation-anion pairs with/without an equivalent number of water molecules were generated using Packmol[198]. After performing a steepest descent energy minimization, the systems were annealed to 700 K in the NVT ensemble for 500 ps followed by an 8 ns NPT equilibration to 333 K and 1 atm using a Berendsen thermostat and barostat[199]. A final NPT equilibration using a Nosé-Hoover thermostat [200, 201] and a Parrinello-Rahman barostat[202] was run for 2 ns. Following equilibration, an NVT production run of 4-10 ns was conducted using the same run parameters as the final equilibration while sampling configurations every picosecond. Three simulations of each system were run using different initial configurations to estimate uncertainties of the calculated structural and dynamic properties. All simulations with $[2CNpyr]^-$ used a 1 fs time step due to the high frequency modes of the cyano group, whereas a time step of 2 fs was used for the other systems. All covalent bonds with hydrogen were constrained using the LINCS algorithm to allow a larger time step to be used [203].

Self-diffusion coefficients of wet and dry systems were calculated using the Einstein relation

$$D = \frac{1}{6t}\langle |r_i(t) - r_i(0)|^2 \rangle \tag{4.1}$$

where D is the self-diffusion coefficient, t is the time, and the quantity in brackets is the mean squared displacement (MSD) of the center of mass of the molecule.

4.2.2 Hydrogen Bonding

The polar nature of ILs causes strong interactions between ions and water. Previous work has shown that hydrogen bonds are important descriptors for characterizing the structure of both pure ILs [204–208] and IL/water mixtures [193, 209, 210]. The energetic and geometric criteria used to describe a hydrogen bond can vary significantly in the literature [79, 204, 211, 212]. In this work, a geometric criterion shown in Figure 4.2 was used to define hydrogen bonds [79, 111].

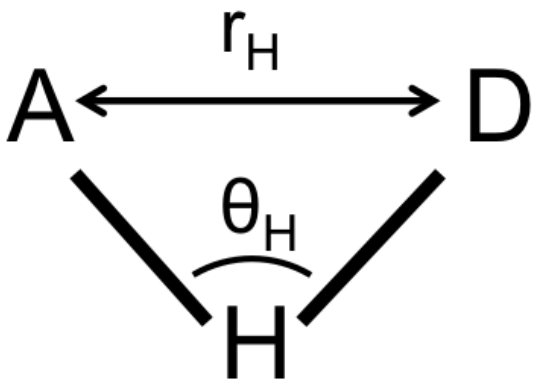

Figure 4.2. Geometric criterion used to define a hydrogen bond. Symbols have the following meaning: A - hydrogen bond acceptor, D - hydrogen bond donor, H - hydrogen, r_H - distance between donor and acceptor atoms, Θ_H acceptor-hydrogen-donor angle. Nitrogen and oxygen atoms were considered to be hydrogen bond acceptors while all atoms covalently bonded to hydrogen were considered to be hydrogen bond donors.

The interaction between hydrogen bond donor and hydrogen bond acceptor atoms was considered to be a hydrogen bond if r_H was less than 3.3 Å while θ_H was greater than 145°. All atoms covalently bonded to hydrogen were considered to be hydrogen bond

donors while all nitrogen and oxygen atoms were considered to be hydrogen bond acceptors. It is difficult to compare the hydrogen bonding character between different IL systems as there is no clear metric for quantifying the degree of hydrogen bonding. Therefore, a previous metric was used to examine hydrogen bonding in terms of the percent of hydrogen bond acceptor atoms satisfying the hydrogen bonding criterion, which we will refer to as the hydrogen bonding occupancy[79, 111].

4.2.3 Henry's Law Coefficients

The relative solubility of water in each IL was estimated through calculation of the Henry's Law constant, $k_H(T.P)$,

$$k_H(T,P) = \mathrm{k}_B T \rho(T,P) \exp\left(\frac{\Delta G_\infty}{\mathrm{k}_B T}\right) \tag{4.2}$$

where k_B is the Boltzmann constant, ρ is the density of the pure IL, and ΔG_∞ is the infinite dilution free energy of solvation. ΔG_∞ was calculated using the Bennett Acceptance Ratio (BAR) method as implemented in GROMACS version 4.5.5 [134]. The simulations work by creating a function of the potential which depends on a coupling parameter, λ, which linearly scales the interaction between the solute and surrounding solvent. The free energy of solvation is calculated by gradually "turning off" solute-solvent interactions by running several simulations ranging from complete solute-solvent interactions to no solute-solvent interactions [134, 213, 214].

The free energy of solvation was calculated using a two step approach. In the first step, the electrostatic contribution to the free energy of solvation was calculated by turning off Coulomb interactions between water and the IL. In a second step, the van der Waals contribution to the free energy of solvation was calculated by turning off the LJ interactions. While the LJ interactions were being turned off, the partial atomic charges of water were set to zero to prevent particle overlap that might cause

simulation instability. For both the electrostatic and the van der Waals portions of the solvation free energy calculation, λ was set to 15 equally spaced values ranging from 0 to 1. For all solvation free energy calculations, a single water molecule was placed in a box of 150 cation-anion pairs to simulate an infinitely dilute system. The same equilibration and production procedures previously mentioned were used in the solvation free energy calculations with the exception that all thermostating was performed using Langevin dynamics.

4.3 Results

4.3.1 Diffusion of Phenolate is Unaffected by Water

The results for the self-diffusion coefficients of both the dry and 1:1 water/IL wet systems are summarized in Table 4.1. Plots of all calculated MSDs can be found in the appendix in Figure B.1.

TABLE 4.1

CALCULATED SELF-DIFFUSION COEFFICIENTS OF THE WET AND DRY ILS

Anion	**D^+ Dry**	**D^+ Wet**	**D^- Dry**	**D^- Wet**
$[2CNpyr]^-$	3.3 ± 0.3	4.4 ± 0.1	4.7± 0.5	7.0 ± 0.6
$[3Triaz]^-$	1.3 ± 0.1	2.2 ± 0.1	1.3 ± 0.2	3.7 ± 0.1
$[PhO]^-$	2.6 ± 0.3	2.3 ± 0.4	3.0 ± 0.2	3.4 ± 1.1

D^+ and D^- are the cation and anion self-diffusion coefficients, respectively. Values given are in units of 10^{-11} m^2 s^{-1}. Uncertainty in the last significant figure was calculated as the standard deviation of calculated diffusivities from three independent simulations.

In $[2CNpyr]^-$ and $[3Triaz]^-$ systems, both cation and anion self-diffusion increased when water was present, with the anion dynamics showing a larger increase. These results agree with the common finding that IL viscosity will tend to decrease when water is added[7, 151, 190, 191], since viscosity generally scales inversely with self-diffusivity according to the Stokes-Einstein model . The diffusion behavior of $[PhO]^-$ systems, however, showed a different behavior when water was added where the anion self-diffusion coefficient increased only slightly whereas the cation self-diffusion coefficient showed no statistical difference between the wet and dry systems.

4.3.2 Liquid Structure Shows Water Resides Near Anions

Most of the literature indicates that ion dynamics increase when water is added to ILs as a results of reduced counterion interactions [154, 156–158]. The liquid structures of each IL were examined through calculation of RDFs and SDFs to see if structural changes from the addition of water could explain the observed changes in diffusivities. SDFs highlighting the interactions of anions with cations, water, and other anions are shown in Figure 4.3. The SDFs show that water interacts quite strongly with the anions in each system. Water resides closer to the anions than the cation phosphorus head groups do. Both water and the polar cation head groups associate primarily with negatively charged anion atoms. The general structure of the cations and anions solvating a central anion does not change appreciably when the water is added to the ILs. There is a unique behavior observed in the $[PhO]^-$ system, however, that is not observed for the other anions. In wet $[PhO]^-$ systems, water causes the anions to approach each other.

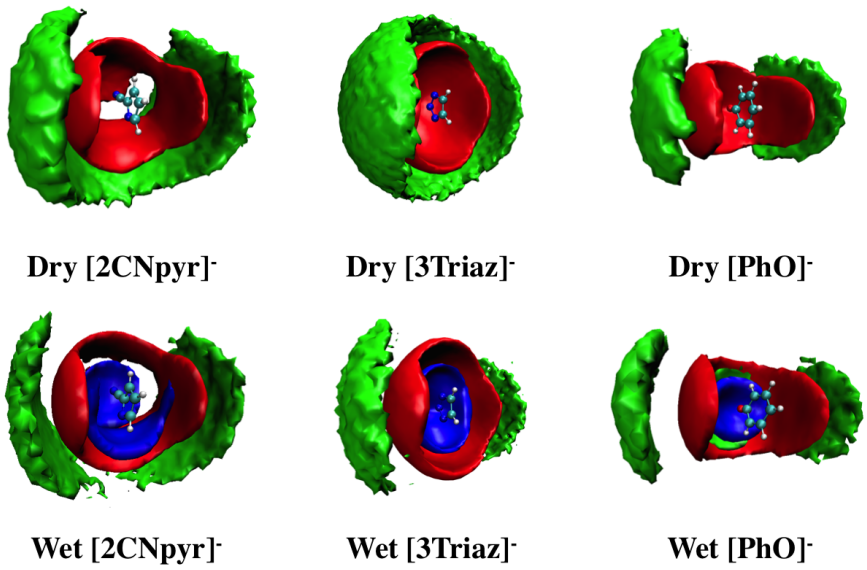

Figure 4.3. SDFs of cations (red), anions (green), and water (blue) about a central anion for both dry and wet systems. The phosphorus from the cation (P), the oxygen on water (O_W), the unique ring nitrogen on $[3Triaz]^-$ (N_2), the ring nitrogen on $[2CNpyr]^-$ (N_1), and the oxygen on phenolate (O) were chosen to represent each species. Isodensity values for each species were chosen to show high probability regions of each species within the first solvation shell.

Changes in the liquid structure shown in the SDFs can be explained through examination of RDFs. RDFs for the wet and dry systems are shown in Figure B.2 of the appendix. For all of the ILs studied, both cation-cation and cation-anion RDFs show decreased coordination when water is added. The peaks broaden and the peak maxima shift to longer distances in agreement with the SDFs. The reduced counterion interactions when water is added helps explain the increased ion diffusivities. Figure 4.4 shows a change in the liquid structure unique to the $[PhO]^-$ IL. The first maximum in the anion-anion RDF shifted from 0.77 nm to 0.43 nm when water was added while the peak height increased from 1.4 to 1.9.

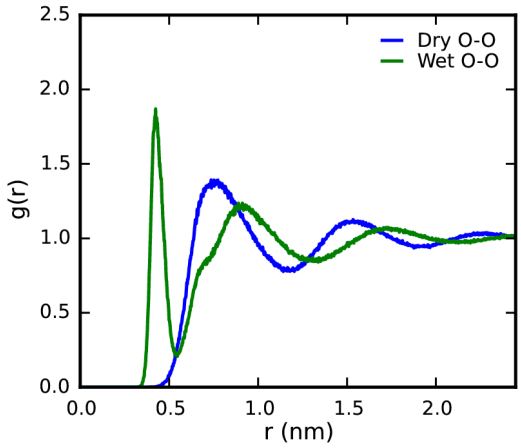

(a) $[PhO]^-$

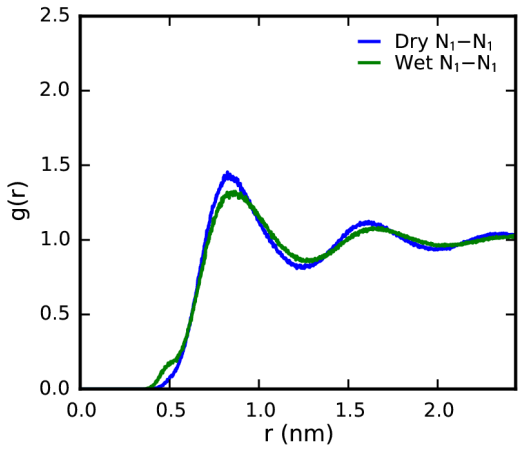

(b) $[2CNpyr]^-$

Figure 4.4. Comparison of anion-anion RDFs of the wet and dry $[PhO]^-$ and $[2CNpyr]^-$ systems.

Wet system RDFs highlighting the different interactions between anions, cations, and water are shown in Figure 4.5. In all of the wet systems, the anions show higher coordination with water than with the cations. The intensity of the first peak in anion-water RDFs decreases as $[PhO]^-$ >> $[3Triaz]^-$ > $[2CNpyr]^-$ with the peak being over three times as high in the $[PhO]^-$ system as in the other systems. The first maximum in the cation-anion RDF is at approximately the same distance as the first maximum in the cation-water RDF for all systems, which implies competing interactions between these species.

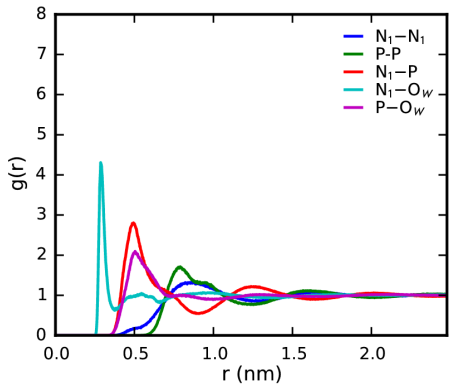

(a) $[2CNpyr]^-$

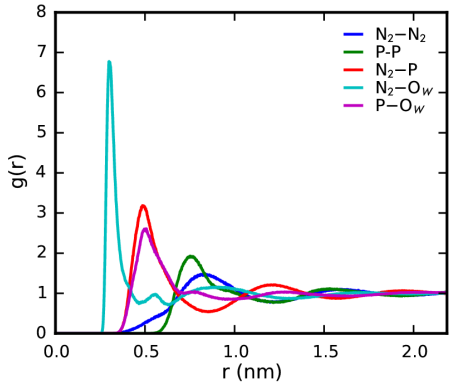

(b) $[3Triaz]^-$

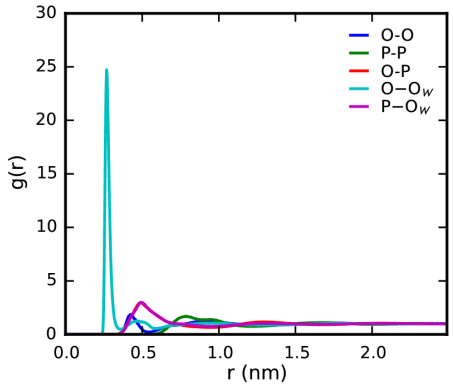

(c) $[PhO]^-$

Figure 4.5. Wet system RDFs. Highly charged atoms were selected to represent each species: the phosphorus atom on the cation (P), the ring nitrogen on $[2CNpyr]^-$ (N_1), the unique nitrogen on $[3Triaz]^-$ (N_2), the oxygen on $[PhO]^-$ (O), and the oxygen on water (O_W).

Figure 4.6 shows RDFs between the water oxygens (O_W) in the wet systems. All systems have a first maximum at 0.27 nm with peak intensities of 33.2, 22.3, and 17.8 for $[2CNpyr]^-$, $[3Triaz]^-$, and $[PhO]^-$, respectively. Based on the intensities of the first maxima in the water-water RDFs, water is dispersed the most in $[PhO]^-$ ILs and clustered the most in the $[2CNpyr]^-$ ILs. The wet $[2CNpyr]^-$ system has a significant second solvation shell, whereas the other systems don't show ordering beyond the first solvation shell.

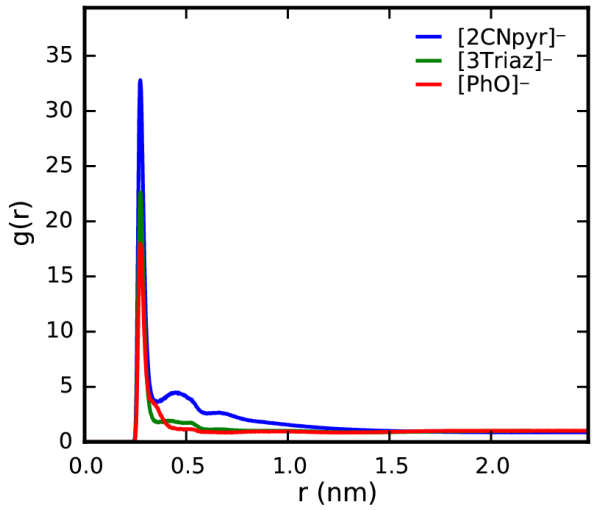

Figure 4.6. RDFs between water oxygens in each wet IL.

4.3.3 Hydrogen Bonding Depends on the Anion

Results for the total hydrogen bonding occupancy [79, 111] considering all possible hydrogen bond donor and hydrogen bond acceptor atoms for the dry and wet systems are shown in Table 4.2.

TABLE 4.2

HYDROGEN BONDING OCCUPANCY CALCULATED AS THE SIMULATION AVERAGE PERCENTAGE OF ACCEPTOR ATOMS SATISFYING THE HYDROGEN BONDING CRITERIA

Condition	**[2CNpyr]$^-$**	**[3Triaz]$^-$**	**[PhO]$^-$**
Dry	0.001 ± 0.001	0.001 ± 0.001	0.012 ± 0.001
Wet	0.453 ± 0.004	0.408 ± 0.001	0.816 ± 0.001

All species covalently bonded to hydrogen were considered hydrogen donors. All nitrogen and oxygen atoms were considered hydrogen acceptors.

There is negligible hydrogen bonding in the dry systems for all of the ILs due to their aprotic nature. The hydrogen bonding occupancy of the wet systems decreases as $[PhO]^- > [2CNpyr]^- > [3Triaz]^-$. This trend follows the absolute value of the charge on the most negative hydrogen bond acceptor atom on each anion. It may therefore be possible to obtain rough estimates of the hydrogen bonding occupancy from relatively cheap charge fitting calculations. However, the hydrogen bonding occupancy still does not allow for direct comparison of ILs that have different numbers of acceptor atoms.

To make better comparisons between ILs, hydrogen bonding between water molecules was calculated to shed light on the dispersion of water in each system. Hydrogen bonding between water molecules indicates that they are forming either clusters or hydrogen bonding networks. Previous studies have shown water will primarily hydrogen bond with anions rather than cations [193, 209, 210]. The calculated RDFs and SDFs indicate that water resides close to the anions near hydrogen bonding acceptor atoms. Hydrogen bonding occupancy between anions and water was therefore calculated normalizing by the number of water molecules to allow a direct comparison of

anions. Hydrogen bonding between water and anions indicates the formation of hydrogen bonding networks. Likewise, hydrogen bonding between water molecules but not between water and the anions indicates that water is aggregating into clusters. A final examination of hydrogen bonding in the wet systems only considered hydrogen bonds where water was considered to be a hydrogen bond donor while anions were considered to be hydrogen bond acceptors. A summary of hydrogen bonding excluding cations is shown in Table 4.3. Correlated distribution functions that compare the hydrogen bond distance to the hydrogen bond angle are presented in Figures B.3- B.10 Hydrogen bonding between water molecules decreases as $[2CNpyr]^- > [3Triaz]^- > [PhO]^-$, indicating that $[2CNpyr]^-$ systems have the most water clustering and $[PhO]^-$ systems have the least. The ability of each anion to form stable hydrogen bonds with water differs. The $[2CNpyr]^-$ system has the least hydrogen bonding between anions and water, while the amount of hydrogen bonding between the anions and water in the $[3Triaz]^-$ and $[PhO]^-$ systems is quite similar.

An interesting result appears in the hydrogen bonding where water acts as a donor while the anion acts as an acceptor. In this case, there is more hydrogen bonding in the $[PhO]^-$ system than in the $[3Triaz]^-$ system. This result is unusual because $[3Triaz]^-$ has three hydrogen bonding acceptors, whereas $[PhO]^-$ has only one. On average, the hydrogen acceptors on $[3Triaz]^-$ have 0.34 occupancy whereas the hydrogen acceptor on phenolate has an occupancy greater than one indicating that multiple waters hydrogen bond with each $[PhO]^-$. An example geometry demonstrating multiple hydrogen bonds between $[PhO]^-$ and water is shown in Figure 4.7. The amount of hydrogen bonding only considering acceptors from anions and donors from water is significantly less than the amount of hydrogen bonding when both species are considered donors and acceptors. There is an interaction between water and the anion ring hydrogens that is most prevalent with $[2CNpyr]^-$ and least prevalent with $[PhO]^-$.

TABLE 4.3

HYDROGEN BONDING OCCUPANCY CALCULATED AS THE SIMULATION AVERAGE NUMBER OF SELECTED HYDROGEN DONOR-HYDROGEN ACCEPTOR PAIRS SATISFYING THE HYDROGEN BONDING CRITERIA NORMALIZED BY THE NUMBER OF WATER MOLECULES

Type	**[2CNpyr]$^-$**	**[3Triaz]$^-$**	**[PhO]$^-$**
Water-Water	0.79 ± 0.03	0.61 ± 0.01	0.43 ± 0.01
Anion-Water	1.36 ± 0.01	1.63 ± 0.01	1.63 ± 0.02
Anion Accepting	0.57 ± 0.01	1.02 ± 0.01	1.20 ± 0.03

The anion accepting row represents hydrogen bonds where water acts as hydrogen donor while the anion acts as a hydrogen acceptor.

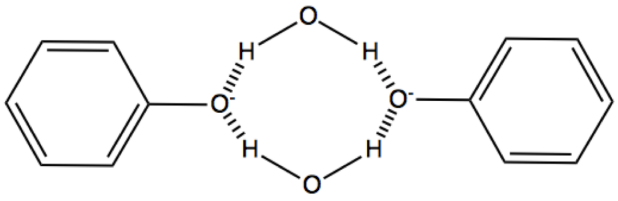

Figure 4.7. Example geometry demonstrating wet [P_{2228}][phenolate] hydrogen bonding. Covalent bonds are shown as solid lines while hydrogen bonds are shown as dashed lines.

4.3.4 Water Solubility Determined by Water-IL Electrostatic Interactions

The relative solubility of water in each IL was estimated by calculating the Henry's law constant for water in each IL using eq. 4.2. The results for ΔG_∞ and the calculated Henry's law constants are shown in Table 4.4. The affinity of an IL for

water depends on the anion, with ΔG_∞ varying by more than 10 kJ mol^{-1} between the three different ILs. Based on the solvation free energy, the $[PhO]^-$ system shows the highest affinity for water while the $[2CNpyr]^-$ system shows the lowest. The LJ portion of the solvation free energy is approximately the same for all systems because they all have comparable liquid densities, and therefore, the cavity formation energy of a neutrally charged molecule is similar in each IL. The Coulombic contribution to ΔG_∞ is greatest for $[PhO]^-$, suggesting that electrostatic interactions are critical for determining water solubility.

TABLE 4.4

INFINITE DILUTION FREE ENERGY OF SOLVATION AND THE RESULTING HENRY'S LAW CONSTANTS AT 333 K AND 1 BAR

Anion	**ΔG Coulomb**	**ΔG LJ**	**ΔG_∞**	**K_H** (bar)
$[2CNpyr]^-$	-21.1 ± 0.3	7.4 ± 0.1	-13.7 ± 0.3	0.54 ± 0.09
$[3Triaz]^-$	-25.6 ± 0.2	7.5 ± 0.1	-18.1 ± 0.2	0.12 ± 0.02
$[PhO]^-$	-33.0 ± 0.6	7.2 ± 0.1	-25.8 ± 0.6	0.01 ± 0.01

Solvation free energies are given in units of kJ mol^{-1}. Uncertainties in the solvation free energies are based on block averaging of five equal length intervals using g_bar in GROMACS 4.5.5.

4.4 Discussion

The presence of water significantly affects both the IL structure and dynamics. When water is added to $[2CNpyr]^-$ and $[3Triaz]^-$ ILs, both cation and anion diffusivities increase because water breaks up counterion interactions as demonstrated in the RDFs. SDFs support these findings, showing that water tends to be located near the highly charged anion atoms which the polar cation head group is attracted to. In the dry ILs, attraction between counterions is very strong resulting in the formation of ion cages that can persist for long times [215]. The co-diffusion of ions within these cages results in slow dry system dynamics. When water reduces counterion attraction through Coulombic screening, the ions are capable of diffusing more freely and the dynamics increase in line with previous findings [154, 156–158].

However, the effects of water on system dynamics are anion dependent. Self-diffusion coefficients for $[2CNpyr]^-$ and $[3Triaz]^-$ approximately doubled when water was added to these systems, whereas $[PhO]^-$ self-diffusion increased by only 13% when water was added. This phenomenon is best explained through examination of the RDFs in combination with the hydrogen bonding results. In the $[2CNpyr]^-$ and $[3Triaz]^-$ systems, the first maxima in the anion-anion RDFs shift to longer distances when water is added, which suggests that water weakens the ionic network, leading to enhanced anion dynamics. The $[PhO]^-$ system exhibits a unique behavior, however, where the addition of water causes the anions to approach each other via hydrogen bonds, forming persistent associated clusters. Although water breaks up counterion interactions in the $[PhO]^-$ systems similarly to the other systems, the $[PhO]^-$ anions demonstrate highly correlated motion when water is present. The bulky cations have difficulty diffusing through associated anions as they become entangled with the anion clusters and compete with water for attraction to anions. Water added to the phenolate systems, therefore, has less of an effect on the the system dynamics.

The calculated Henry's law constants show that all of the ILs studied have high

water affinity. The solvation free energy for water in each IL is highly negative, indicating that water present in vapors contacting the IL will spontaneously be absorbed into the ILs. The differences in solvation free energies can be attributed to anion-water Coulombic interactions. The trend in magnitude of the Coulombic portion of the solvation free energy follows the same trend as the amount of hydrogen bonds formed where water acts as a hydrogen bond donor while the anions act as hydrogen bond acceptors. The ability of an anion to stabilize water through hydrogen bonding determines the water solubility. The high water affinity of AHA ILs can be a serious issue in CO_2 separations because water not only affects the physical properties of the ILs, but it could also affect the reaction chemistry [7, 121, 151, 152].

4.5 Conclusions

The effects of water on the liquid structure and dynamics of AHA ILs were investigated for three CO_2-reactive ILs having a common phosphonium cation but different heterocyclic anions. The addition of water reduced both cation-cation and cation-anion coordination in all of the ILs. When water was added to $[PhO]^-$ ILs, anions associated through hydrogen bonds. This behavior was not observed in the wet $[2CNpyr]^-$ and $[3Triaz]^-$ systems. Water added to the ILs reduced counter ion interactions resulting in higher anion diffusivities in agreement with literature on other classes of ILs. Cation self-diffusion decreased in the wet $[PhO]^-$ systems because cation motion was hindered by water-$[PhO]^-$ hydrogen bonding networks.

The solubility of water in the ILs, as determined by Henry's law constants, followed the trend $[PhO]^- > [3Triaz]^- > [2CNpyr]^-$, following the same trend of hydrogen bonding between anions and water. The relative solubilities of water in each IL depends on the ability of the anion to stabilize the water through hydrogen bonding. Decomposition of the water solvation free energy into Coulombic and LJ contributions showed that the difference in solvation free energies depends almost entirely on

Coulombic interactions. Therefore, through choice of anions, the hydrogen bonding and thus the water solubility can be tuned to reduce the AHA IL viscosity and optimize performance in CO_2 separations. It would be interesting in future studies to examine if the choice of cation can also affect interactions with water. For instance, one could imagine that functionalization of cation alkyl chains with polar functional groups might increase cation-water interactions leading to higher dispersion of water and an even greater increase in the system dynamics.

CHAPTER 5

LIQUID STRUCTURE OF CO_2-REACTIVE APROTIC HETEROCYCLIC ANION IONIC LIQUIDS FROM X-RAY SCATTERING AND MOLECULAR DYNAMICS

5.1 Introduction

In the review presented in Chapter 1, an important point arrises that properties of liquids can be understood in terms of their liquid structure. Molecular dynamics (MD) simulation have been used extensively to examine the molecular level structure of liquids, from which bulk properties can be understood. The liquid structure provides information on the dominant and persistent interactions between different species, and how these interactions give rise to observable properties. Although much is known about the physical and chemical properties of aprotic heterocyclic anion ionic liquids (AHA ILs) [6, 7, 16], little is known about their liquid structure. Therefore, the purpose of the present chapter is to examine the liquid structure of AHA ILs and how it changes due to cation and anion substitution as well as reaction with CO_2.

Several research groups have examined the liquid structure for other classes of ILs using X-ray or neutron scattering experiments combined with MD simulations [113–120, 216–218]. A number of groups have used high-energy X-ray scattering experiments to study the liquid structure for a variety of ILs with different types of anions and cations [118, 119, 219–223]. The electrostatic interactions that dominate the liquid ordering typically result in three primary long range structure function

features: a prepeak also known as a first sharp diffraction peak between 0.25-0.5 $Å^{-1}$ due to the alternation of polar/nonpolar domains, a charge separation feature near 1 $Å^{-1}$, and a peak near 1.5 $Å^{-1}$ due to adjacency interactions within the IL. The prepeak is usually attributed to heterogeneous domain formation within the IL, which generally requires ions of sufficient size with long nonpolar tails although this is not always the case [118, 120, 219–222, 224–231]. Several computational researchers have demonstrated that MD simulations can recover the experimental structure functions and shed light on the specific molecular correlations responsible for these features [114, 217, 231–236]. Partitioning of the total structure function into partial structure functions representing the correlations between the different ions revealed a charge alternation feature, which was absent in the total structure function of certain ILs due to the cancellation of peaks and antipeaks. Kashyap found that when the long alkyl cation tails are functionalized with polar ether groups, the liquid structure function changes dramatically and the prepeak disappears [233]. Additionally, simulations showed the percolation of polar and nonpolar networks that are primarily responsible for the ordering within ILs [113, 114, 217, 223, 229, 233, 236].

The objective of the present work is to obtain a detailed understanding of the liquid structure of AHA ILs in both the unreacted and CO_2-reacted states using a combination of X-ray scattering experiments and MD simulations. The ILs studied are a combination of two phosphonium cations, triethyloctylphosphonium ($[P_{2228}]^+$) and trihexyltetradecylphosphonium ($[P_{66614}]^+$), paired with two different AHA anions, 2-cyanopyrrolide ($[2CNpyr]^-$) and 1,2,4-triazolide ($[4Triaz]^-$). These ILs have shown great promise as CO_2 capture solvents [7]. The effects of the CO_2 reaction on the liquid structure are investigated by comparison of neat and CO_2 complexed IL structure functions. Additionally, we examine the changes in the IL structure from both cation and anion substitutions. Finally we comment on the ability of the structure function to describe the liquid structure and the additional insights provided by

MD simulation.

5.2 Experimental Methods

5.2.1 X-ray Scattering Experiments

Experimental structure functions were measured by Seungmin Oh of the Brennecke research group from The University of Notre Dame with help from Edward W. Castner Jr. X-ray scattering data was obtained in a momentum transfer (q) range of 0.2 to 20 $Å^{-1}$ using X-rays generated at the Advanced Photon Source (APS) beam-line 11-ID-B at Argonne National Laboratory. All samples contained less than 500 ppm of water for both pure and CO_2 saturated ILs. All IL structure functions were measured at room temperature where the ILs remained liquid (note that $[P_{2228}]$[4Triaz] was a super-cooled liquid). Samples were exposed to a collimated X-ray beam (58.65 kV, $\lambda = 0.2114$ Å) with a monochromator of Si(311), a beam size of 0.5 mm x 0.5 mm and a 120 s total exposure time. The given X-ray scattering data were post-processed for integration and domain conversion from scattering angle, 2Θ, to scattering vector, q, using the Fit2D software package from Hammersley *et al* [237, 238]. The total structure function was calculated using eq. 5.1

$$S(q) = \frac{I_{coh}(q) - \sum_i x_i f_i^2(q)}{\left[\sum_i x_i f_i^2(q)\right]^2} \tag{5.1}$$

in which $I_{coh}(q)$ indicates the total intensity, x_i is fraction of atom type i, and $f_i(q)$ is the atomic form factor of atom type i found in the International Tables of Crystallography [239]. The structure function calculation and various corrections were processed using PDFgetX2 software from Qui *et al.* [240]. The atomic fraction of each CO_2 saturated IL was determined using previously reported and new experimental CO_2 solubility data: 0.92, 0.9, 0.8, and 0.8 moles of CO_2 per mole IL for $[P_{2228}]$[2CNpyr] [16], $[P_{66614}]$[2CNpyr] [7], $[P_{2228}]$[4Triaz], and $[P_{66614}]$[4Triaz] [7], re-

spectively.

5.3 Computational Methods

The structures of the ions studied in this work are shown in Figure 5.1. $[4Triaz]^-$ has two different nitrogen sites where the CO_2 can react. It is currently unknown where the $[4Triaz]^-$ reaction site is in the liquid phase. Therefore, both reaction sites were considered in this work with the hope that comparison of the simulated and experimental structure functions would identify the stable reaction site.

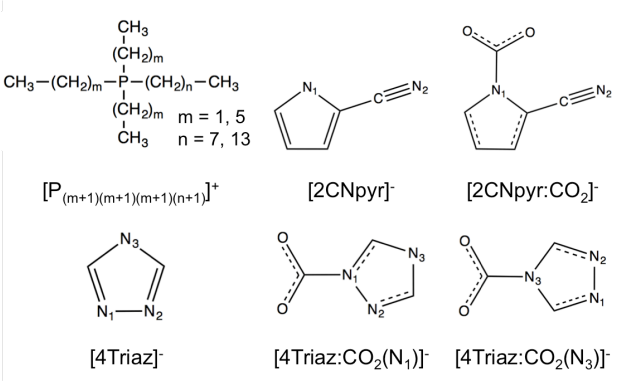

Figure 5.1. Structures of ions studied in this work. The phosphonium cations have different alkyl chain lengths where m and n are equal to 1 and 7 or 5 and 13 for $[P_{2228}]^+$ and $[P_{66614}]^+$, respectively.

The liquid structure function was calculated via MD simulations using eq. 5.2

$$S(q) = \frac{\rho_\circ \sum_{i=1}^{N} \sum_{j=1}^{N} x_i f_i(q) x_j f_j(q) \int_0^{r_\infty} 4\pi r^2 (g_{ij}(r) - 1) \frac{sin(qr)}{qr} W(r) dr}{\left[\sum_{i=1}^{N} x_i f_i(q)\right]^2} \qquad (5.2)$$

where S(q) is the total structure function, $\rho_\circ$ is the atomic number density, i and j are indices for unique atom types, N is the total number of atom types, $f_i(q)$ is the atomic form factor for atom type i, $g_{ij}(r)$ is the pair distribution function between atoms of types i and j, r is the distance between atoms i and j, and q is the scattering vector. $W(r)$ is a Lorch window function given by $W(r) = sin(2\pi r/L)/(2\pi r/L)$ [236]. Computer simulations can provide additional understanding of experimental structure functions because the summation limits in eq. 5.2 can be selected to extract partial structure functions correlating specific groups of atoms. For example, both summations can run over the indices of cation atoms thereby obtaining the cation-cation contribution to the total structure function. By partitioning the total structure function in this way, one can gain valuable insights into the interactions which determine the liquid structure. Previous works by Santos and Kashyap showed that this partitioning reveals important features of the liquid structure which can remain absent in the experimental structure function due to the cancellation of peaks by antipeaks [119, 232–234].

To calculate the liquid structure functions, a series of MD simulations were run using GROMACS version 4.5.5 [194–196]. Initial structures were generated by placing 1000-2000 ion pairs in a simulation box using Packmol [198]. In modeling the CO_2-reacted ILs, it was assumed that all of the anions were bound to CO_2. No physically absorbed CO_2 was considered as the amount of physically absorbed CO_2 is estimated to be less than 3 mole % [16]. Next, a steepest descent energy minimization was performed. Following the energy minimization, the systems were annealed to 700 K for 500 ps, and subsequently equilibrated in the NPT ensemble. The equilibration procedure differed depending on the system due to the large size and slow dynamics of the $[P_{66614}]^+$ cation. Production runs for systems with $[2CNpyr]^-$ were run at 300 K while production runs for systems with $[4Triaz]^-$ were run at 313 K due to the higher melting point of ILs with this anion. Note that the temperature difference

of 18 K between the simulations and experiments will have a negligible impact on the liquid structure functions due to the low thermal expansivities of ILs [119, 235]. For the $[P_{2228}]^+$ systems, an initial NPT equilibration to the production temperature and 1 atm was performed for 8 ns using a Berendsen thermostat and barostat. Next, the systems were equilibrated for an additional 2 ns using a Nosé-Hoover thermostat [200, 201] and a Parinello-Rahman barostat [202]. Following the equilibration, an NVT production run of 2-4 ns was performed, saving configurations every 0.1-0.3 ps. For the $[P_{66614}]^+$ systems, additional initial equilibration was performed to allow the system to relax properly following the annealing. For these systems, the temperature was decreased by 100 K over 1 ns intervals until reaching the production temperature. At this point the same equilibration and production run procedures of the $[P_{2228}]^+$ systems were followed. For all simulations, a time step of 1 fs was used. All covalent bonds to hydrogen were constrained using the LINCS algorithm to allow a larger time step [203]. The equations of motion were integrated using the Verlet Leap-Frog algorithm [241, 242]. Long range electrostatics were handled using particle-mesh Ewald summation [197]. Long range corrections were applied to both energy and pressure. Lorentz-Berthelot mixing rules were applied to Lennard-Jones interactions [243]. All force field parameters are provided in Appendix A.

Preliminary simulations were performed on the $[P_{2228}]$[2CNpyr] system to evaluate the effects of the cutoff radius as well as the system size on the calculated structure function. First, simulations of 1000 ion pairs were run where the cutoff radius was set to either 12 or 14 Å. The resulting structure functions were found to be unaffected by an increase in the cutoff radius. Therefore, the cutoff was set to 12 Å for all remaining systems to speed up the simulations. The system size was then tested by performing simulations of 1000 and 2000 ion pairs. Again these simulations produced nearly identical structure functions so all further simulations used between 1000 and 2000 ion pairs.

5.4 Results

5.4.1 Experimental Structure Functions

The experimental structure functions are shown in Figure 5.2 for ILs containing $[P_{2228}]^+$ with unreacted and CO_2-reacted $[2CNpyr]^-$ and $[4Triaz]^-$. For the unreacted $[4Triaz]^-$, there is a small prepeak at 0.42 $Å^{-1}$ and two additional overlapping peaks near 1 $Å^{-1}$ and 1.5 $Å^{-1}$. The unreacted $[2CNpyr]^-$ has the same overlapping peaks near 1 $Å^{-1}$ and 1.5 $Å^{-1}$, but it does not have a clearly defined prepeak. For the CO_2-reacted ILs, the overlapping peaks at 1.5 $Å^{-1}$ become more pronounced for $[2CNpyr]^-$, but for $[4Triaz]^-$ there is only one peak. The prepeaks are still present for the CO_2-reacted ILs, with the one for $[2CNpyr]^-$ becoming more pronounced upon reaction. Previous studies on other ILs have observed these three peaks, assigning them as a prepeak, a charge alternation peak, and an adjacency peak, respectively [119, 232–234]. In the intra-molecular region ($q > 2$ $Å^{-1}$), the structure functions of all liquids are similar because the cations are the same and the anions have very similar structures.

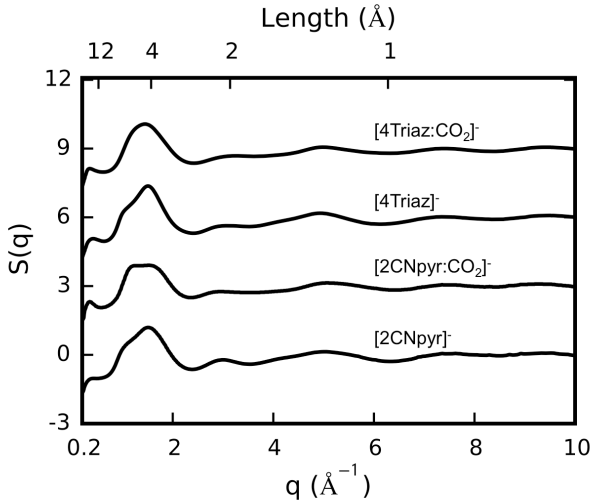

Figure 5.2. Room temperature (295 K) experimental structure functions for all ILs with $[P_{2228}]^+$. The structure functions are offset by 0, 3, 6, and 9 for $[2CNpyr]^-$, $[2CNpyr:CO_2]^-$, $[4Triaz]^-$, and $[4Triaz:CO_2]^-$, respectively. The primary abscissa (bottom) is in reciprocal space while the secondary abscissa (top) shows the corresponding real space distance.

Figure 5.3 compares the experimental structure functions for unreacted and CO_2-reacted $[2CNpyr]^-$ with the $[P_{66614}]^+$ and $[P_{2228}]^+$ cations. In the inter-molecular region ($q < 2$ Å^{-1}), there are pronounced intensity increases in the prepeak and adjacency peak when either anion is paired with the larger cation, combined with a less pronounced increase in peak intensities in the intra-molecular region ($q > 2$ Å^{-1}). The prepeak is clearly developed at approximately 0.4 Å^{-1} in the $[P_{66614}]^+$ systems, and the adjacency peak is a single distinctive peak rather than two partially overlapping peaks, as seen in the $[P_{2228}]^+$ systems. These features of the $[P_{66614}]^+$ systems have been observed in the structure functions of other ILs that have the same cation [113, 119]. Also, for both anions, the prepeak location shifts to slightly larger q values when comparing $[P_{66614}]^+$ to $[P_{2228}]^+$ ILs. However, saturating the ILs with

CO_2 has almost no effect on the structure functions of the $[P_{66614}]^+$ ILs.

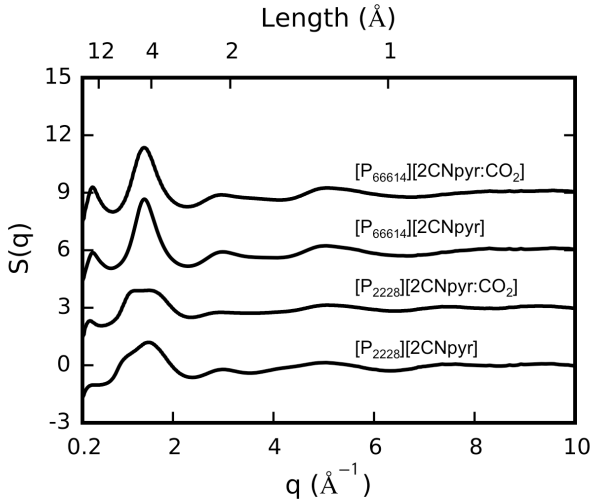

Figure 5.3. Room temperature (295 K) experimental structure functions for all ILs with $[2CNpyr]^-$. The structure functions are offset by 0, 3, 6, and 9 for $[P_{2228}][2CNpyr]$, $[P_{2228}][2CNpyr:CO_2]$, $[P_{66614}][2CNpyr]$, and $[P_{66614}][2CNpyr:CO_2]$, respectively. The primary abscissa (bottom) is in reciprocal space while the secondary abscissa (top) shows the corresponding real space distance.

The position of the prepeak in $S(q)$ for the two AHA-ILs with the $[P_{66614}]^+$ cation is found at q=0.40 Å^{-1} and q=0.38 Å^{-1} for the $[2CNpyr]^-$ and $[4Triaz]^-$ anions, respectively. Compared to prepeak positions for two other ILs that also have the $[P_{66614}]^+$ cation, this indicates a domain size for the AHA ILs that is between the ones based on Cl^- or $[Tf_2N]^-$ anions. Gontrani *et al.* reported a prepeak at q=0.37 Å^{-1} for $[P_{66614}][Cl]$ [113], while Kashyap *et al.* reported a value of q=0.42 Å^{-1} for $[P_{66614}][Tf_2N]$ [119]. A Cl^- anion for a tetrahedral phosphonium cation should lead

to a polar domain with a coordination number of about four anions surrounding each cation, with the size and packing leading to the observed intermediate range order then being determined by nanoscale aggregation of the hydrocarbon tails. The charged head-group interactions for a bulky, flexible anion such as $[Tf_2N]^-$ are necessarily more diffuse. The details of the packing arrangements about the cation for the two AHA anions, $[4Triaz]^-$ and [2CNpyr], must lead to longer-range interactions in $[P_{66614}]^+$ ILs.

A different effect is noted for the position of the prepeak in $S(q)$ for the two AHA ILs with $[P_{2228}]^+$. The prepeak in $S(q)$ for $[P_{2228}][4Triaz]$ is observed at q=0.42 $Å^{-1}$ while there is no well defined prepeak observed for $[P_{2228}][2CNpyr]$. Previous studies of the liquid structure of $[P_{2228}][Tf_2N]$ showed a prepeak at q=0.4 $Å^{-1}$ indicating that the packing of this tetraalkyl-phosphonium cation with the $[4Triaz]^-$ anion leads to intermediate range order with a less extended range with an effective domain size of about 15 Å, as compared to the domain size of about 16 Å for $[P_{2228}][Tf_2N]$ [217].

5.4.2 Comparison of Experimental and Simulated Structure Functions

A comparison between experimental and simulated densities is shown in Table 5.1. The simulated densities are consistently lower than the experimental densities by 2-5%, with the difference being larger for ILs with $[P_{2228}]^+$. This level of agreement is sufficient for obtaining reliable liquid structures from MD simulations.

The simulated and experimental structure functions for the ILs with $[2CNpyr]^-$ are shown in Figure 5.4. Simulated and experimental structure functions for ILs with $[4Triaz]^-$ are shown in the SI. In all systems, the simulated structure functions have smaller prepeaks than the corresponding experimental structure functions. Additionally, the amplitude of the adjacency peak tends to be slightly larger in the simulations than in the experiments. The simulations capture the experimental observation that

TABLE 5.1

COMPARISON OF EXPERIMENTAL AND SIMULATION DENSITIES

System	Temperature (K)	Experiment	Simulation	% Difference
$[P_{2228}][2CNpyr]$ [16]	300	0.953	0.913(1)	-4.2
$[P_{2228}][2CNpyr:CO_2]$	300	1.024	0.977(1)	-4.6
$[P_{2228}][4Triaz]$	313	0.957	0.915(1)	-4.4
$[P_{2228}][4Triaz:CO_2]$	313	1.016	0.979(1)	-3.6
$[P_{66614}][2CNpyr]$ [7]	300	0.900	0.874(1)	-2.9
$[P_{66614}][2CNpyr:CO_2]$	300	0.929	0.909(1)	-2.2
$[P_{66614}][4Triaz]$ [7]	313	0.892	0.867(1)	-2.8
$[P_{66614}][4Triaz:CO_2]$	313	0.922	0.903(1)	-2.1

Experimental values for all systems other than ILs with unreacted $[4Triaz]^-$ have been interpolated based on a linear fit of temperature dependent densities. All densities are in units of g cm^{-3}. Experimental uncertainties are 1 x 10^{-3} g cm^{-3}. Simulation uncertainties in the last significant digit, shown in parenthesis, are estimated using block averaging on the final 2 ns of NPT equilibration.

the adjacency peak in the $[P_{2228}][2CNpyr]$ IL broadens upon reaction with CO_2. Both the experimental and simulated structure functions of the $[P_{66614}]^+$ ILs do not change after reaction with CO_2. Given the excellent agreement between the simulated and experimental structure functions, the MD structure functions can be partitioned into subcomponents to provide further insights into the liquid structure.

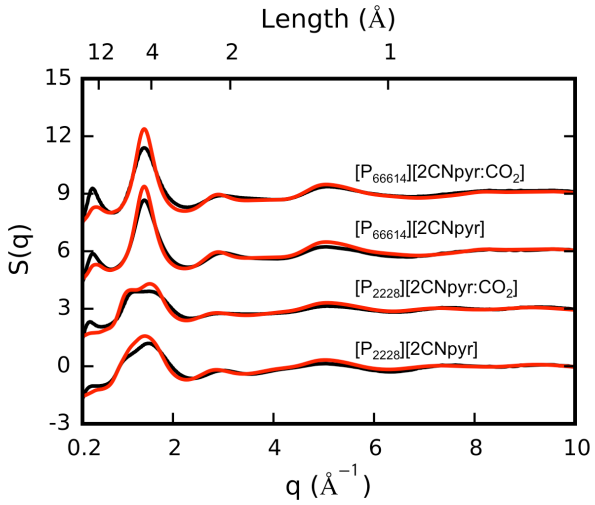

Figure 5.4. Comparison of experimental and simulated structure functions for all $[2CNpyr]^-$ ILs. Experimental structure functions are shown in black. Simulated structure functions are shown in red. The structure functions are offset by 0, 3, 6, and 9 for $[P_{2228}][2CNpyr]$, $[P_{2228}][2CNpyr:CO_2]$, $[P_{66614}][2CNpyr]$, and $[P_{66614}][2CNpyr:CO_2]$, respectively. The primary abscissa (bottom) is in reciprocal space while the secondary abscissa (top) shows the corresponding real space distance.

5.4.3 Structure Function Partitioning - Unreacted ILs

Previous work has shown that important IL structure function features can be absent in the experimental structure function due to the cancellation of peaks with

antipeaks. The decomposition of the $[P_{2228}][2CNpyr]$ total structure function into the cation-cation ($S^{C-C}(q)$), anion-anion ($S^{A-A}(q)$), and cation-anion ($S^{C-A}(q) + S^{A-C}(q)$) partial structure functions is shown in Figure 5.5. Both the $S^{C-C}(q)$ and $S^{A-A}(q)$ curves show peaks at a q value of 0.8 Å^{-1}, corresponding to a Bragg domain size of 8 Å. Examination of radial distribution functions shown in Figure C.5 confirms that both the cation-cation and anion-anion RDFs have a first maximum at this distance. However, the total structure function does not display a peak at this distance due to a cancellation by the counterion cross correlation antipeak. None of the partial structure functions appear to contribute significantly in the prepeak region. The adjacency peak has contributions from each of the ionic partial structure functions due to the adjacency interactions between each group.

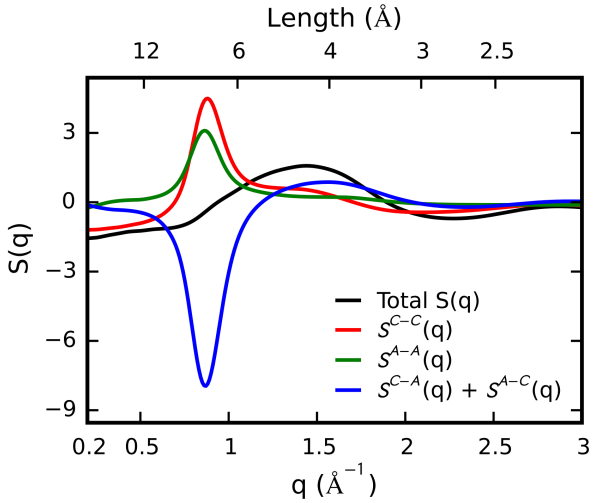

Figure 5.5. Ionic partial structure functions for $[P_{2228}][2CNpyr]$. The primary abscissa (bottom) is in reciprocal space while the secondary abscissa (top) shows the corresponding real space distance.

It is known that ILs have both polar and nonpolar domains. Following the work of Santos and Kashyap [119, 232–234], the partial structure functions were computed by further partitioning the cation into a polar head group (CH) consisting of the phosphorus and the short alkyl chains and a nonpolar tail group (CT) consisting of the long alkyl chain. Figure 5.6 shows the resulting partial structure functions involving the CT group. There is indeed a significant contribution to the prepeak from CT-CT correlations. However, this contribution is once again masked from the total structure function due to cancellation by the CT-CH and CT-A antipeaks. Both the CT-CT and CT-A correlations make substantial contributions to the adjacency peak at 1.5 Å^{-1} indicating close contact of these species.

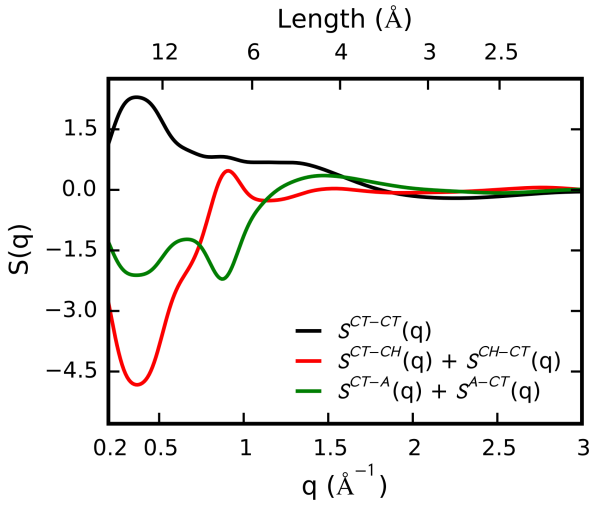

Figure 5.6. Partial structure functions of $[P_{2228}][2CNpyr]$ involving the CT group. The primary abscissa (bottom) is in reciprocal space while the secondary abscissa (top) shows the corresponding real space distance.

While the structure functions provide useful information about the liquid ordering, they only give a one dimensional description of the three dimensional liquid. Further insight into the arrangement of ions within the IL can be obtained by examining spatial distribution functions (SDFs) from the MD simulations. Figure 5.7 shows SDFs for the unreacted $[P_{2228}]^+$ ILs. Although the structure functions of these ILs are nearly identical, there are stark differences in the SDFs about a central anion. $[4Triaz]^-$ has its negative charge distributed more evenly around the aromatic ring while $[2CNpyr]^-$ has most of its charge localized on the two nitrogen sites. The different charge distributions cause distinct arrangements of the anions with respect to the cations and other anions. In the $[2CNpyr]^-$ system, the anion tends to orient with the nitrogens toward the phosphorus of the cation. The nitrogens attract cation heads, which in turn structure the other anions. The $[4Triaz]^-$ anion shows less of a preferred orientation towards the cation where the phosphorus will associate with the entire ring instead of just one side. From the perspective of a central cation, however, the SDFs of the two ILs are quite similar.

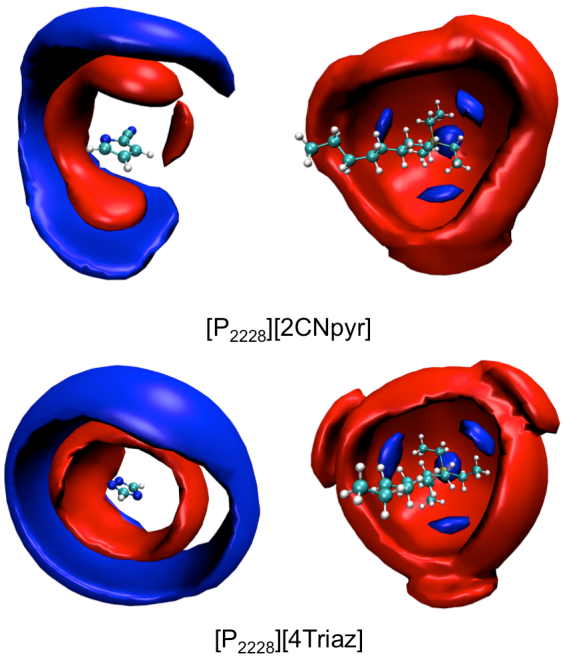

Figure 5.7. Comparison of SDFs for $[P_{2228}][2CNpyr]$ and $[P_{2228}][4Triaz]$. For the $[P_{2228}][2CNPyr]$ system, the cation P atom (red) is shown at isodensities 5 and 2.4 nm^{-3} and the anion N_1 atom (blue) is shown at isodensities of 2.8 and 7 nm^{-3} for the $[2CNpyr]^-$ and $[P_{2228}]^+$ reference molecules, respectively. For the $[P_{2228}][4Triaz]$ system, the cation P atom (red) is shown at isodensities 5 and 2.5 nm^{-3} and the N_1 atom (blue) is shown at isodensities of 3 and 9 nm^{-3} for the $[4Triaz]^-$ and $[P_{2228}]^+$ reference molecules, respectively. All SDFs were computed using TRAVIS [14] and rendered using VMD [15].

5.4.4 Structure Functions of CO_2-Reacted ILs

While the reaction with CO_2 does not change the main features of the total structure function, there are a few noticeable differences between the unreacted and CO_2-reacted systems. The reaction with CO_2 causes the adjacency peak in the $[P_{2228}][2CNpyr]$ structure function to flatten and broaden in both the experimental and simulated structure functions. Figure 5.8 compares the simulation results

of the unreacted and CO_2-reacted total structure function as well as the ionic subcomponents. The peak broadening is a result of several changes in the ionic partial structure functions. Primarily, there is a decrease in the cation-cation and cation-anion correlation in the adjacency peak region. The anion-anion structure function, however, shows no major differences between the unreacted and CO_2-reacted systems.

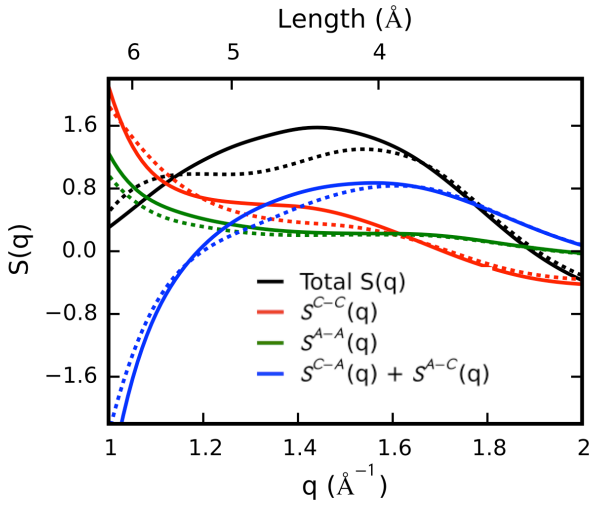

Figure 5.8. Comparison of unreacted (solid lines) and CO_2-reacted (dashed lines) $[P_{2228}][2CNpyr]$ total structure functions and the ionic subcomponents. The bounds were chosen to highlight the changes in the adjacency peak upon reaction with CO_2. The primary abscissa (bottom) is in reciprocal space while the secondary abscissa (top) shows the corresponding real space distance.

The reaction with CO_2 has even less of an effect on the $[P_{2228}][4Triaz]$ system. Unlike $[2CNpyr]^-$, CO_2 can react at one of two sites on $[4Triaz]^-$ (N_1 and N_3, noting that N_2 is equivalent to N_1). Figure 5.9 shows a comparison of the experimental

structure function with the simulated structure functions considering the different possible reaction sites of $[4Triaz]^-$. Three different reaction scenarios were considered for this system: all of the CO_2 reacted at the N_1 site, all of the CO_2 reacted at the N_3 site, and a 50/50 mix of the two reaction sites. While all of the simulated structure functions differ slightly from the experimental structure function, they are virtually indistinguishable from one another. This suggests that the long range order is insensitive to the reaction site of $[4Triaz]^-$, and the preferred binding site cannot be determined from the structure functions.

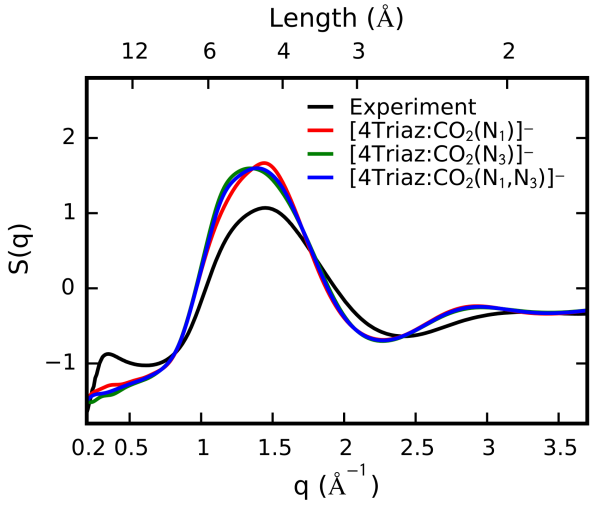

Figure 5.9. Comparison of experimental and simulated $[P_{2228}][4Triaz:CO_2]$ structure functions. $[4Triaz:CO_2(N_1)]$, $[4Triaz:CO_2(N_2)]$, and $[4Triaz:CO_2(N_1, N_3)]$ correspond to simulations with the CO_2 reacted at the N_1 site, the N_3 site, and a 50/50 mix of the two sites, respectively. The primary abscissa (bottom) is in reciprocal space while the secondary abscissa (top) shows the corresponding real space distance.

The reaction site on $[4Triaz]^-$ does effect the liquid structure, as shown in Figure

5.10. When the CO_2 reacts at the N_1 site, the cation interacts primarily with one side of the anion due to the asymmetric charge distribution. When the CO_2 reacts at the N_3 site, however, there is a symmetric charge distribution on the anion and therefore the cation forms close contacts with the entire anion. Similar to the case of the unreacted anions, the SDFs about a central cation show the same four lobes where the anions tend to locate. While the reaction site affects which atom on the anion is closest to the phosphorus of the cation, it does not effect the positions of anions solvating the cation head group. The fact that the cation SDFs show the same behavior regardless of the anion and whether or not it is reacted with CO_2 helps to explain why the structure functions for a given cation display the same characteristic features.

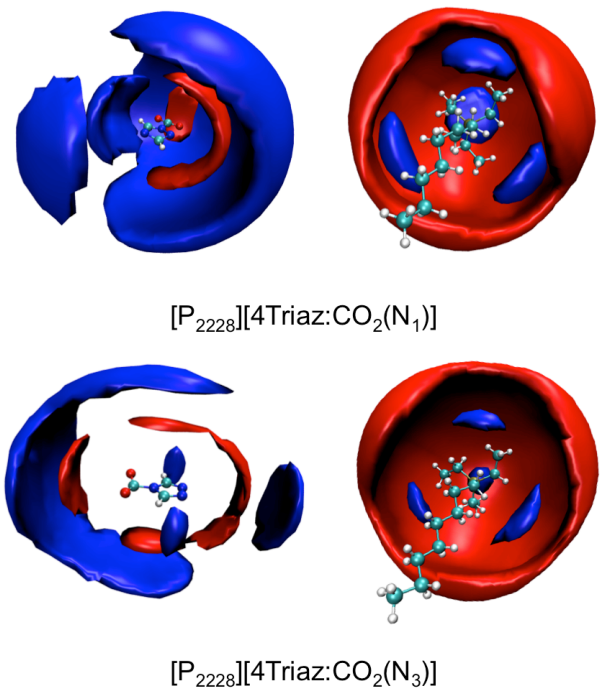

Figure 5.10. Comparison of SDFs considering the different $[P_{2228}][4Triaz{:}CO_2]$ reaction sites. For both of the CO_2-reacted systems, the cation P atom (red) is shown at isodensities of 8 and 2.5 nm^{-3} and the reaction site N atom (blue) is shown at isodensities of 2.5 and 6 nm^{-3} for the $[4Triaz{:}CO_2]^-$ and $[P_{2228}]^+$ reference molecules, respectively.

5.4.5 Structure Function - Cation Substitution

Both experimental and simulation results show that the structure function changes more from cation substitution than from anion substitution. This is to be expected since the maximum spatial extent of the cations is 11 heavy atoms for $[P_{2228}]^+$ and 21 for $[P_{66614}]^+$, while the anions have only 3 or 5 heavy atoms for $[4Triaz]^-$ and $[2CNpyr]^-$, respectively. For both anions studied, increasing the cation alkyl chain lengths increases the amplitudes of the prepeak and adjacency peak. Figure 5.11 shows a partitioning of the $[P_{66614}][2CNpyr]$ total structure function into

its ionic subcomponents. The ionic subcomponents have different behavior than in the $[P_{2228}][2CNpyr]$ system. Of notable interest is the fact that the cation-cation structure function now has two peaks instead of one and contributes more to the adjacency peak. Additionally, the cation-anion structure function shows a much more well defined peak in the adjacency region while the anion-anion structure function makes only a slight contribution to the adjacency peak. The combination of both the cation-cation and cation-anion structuring causes the increase in the adjacency peak as compared to the corresponding $[P_{2228}]^+$ system. Both the cation-cation and anion-anion structure functions show a peak at 0.8 $Å^{-1}$ while the cation-anion structure function shows an antipeak at this location similar to what was observed for the $[P_{2228}]^+$ cation. However, with the $[P_{66614}]^+$ cation there is a significant left shoulder to the anion-anion peak which, out of all the ionic partial structure functions, makes the largest contribution to the prepeak.

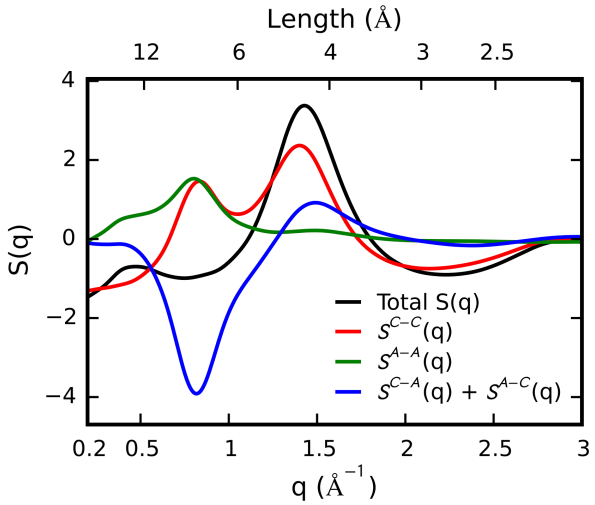

Figure 5.11. Decomposition of the $[P_{66614}][2CNpyr]$ total structure function into its ionic partial structure function components. The primary abscissa (bottom) is in reciprocal space while the secondary abscissa (top) shows the corresponding real space distance.

The reaction with CO_2 in the $[P_{66614}]^+$ systems does not change the total structure function. However, the ionic partial structure functions shown in Figure 5.12 have appreciable differences between the unreacted and CO_2-reacted systems. The anion-anion peak shifts towards smaller q values, which makes sense due to the increased anion size after the reaction. The cation-anion antipeak also shifts to the same q value. The CO_2-CO_2 partial structure function is rather flat and featureless making a slight contribution to intermolecular features over a wide range of q values. The CO_2-anion partial structure function has a peak in the charge alternation region as well as a broad shoulder extending to small q values while the CO_2-cation partial structure function forms an antipeak in the charge alternation region and makes a slight contribution to the adjacency peak. Once again, the experimental structure function provides much

useful information regarding ordering of different liquid domains, but correlations of specific species can be "drowned out" due to the panoptic nature of the scattering experiment.

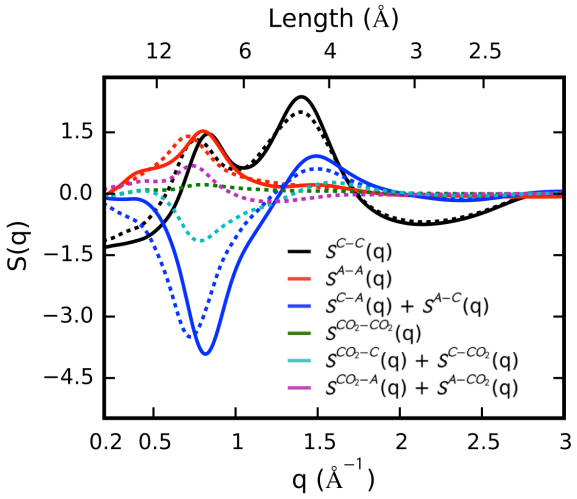

Figure 5.12. Comparison of unreacted (solid lines) and CO_2-reacted (dashed lines) $[P_{66614}][2CNpyr]$ ionic and subionic partial structure functions. The primary abscissa (bottom) is in reciprocal space while the secondary abscissa (top) shows the corresponding real space distance.

5.5 Discussion

The AHA ILs studied in this work have the same characteristic structure function features as previously studied ILs: a prepeak, a "hidden" charge alternation peak, and an adjacency peak. The prepeak forms between 0.3 and 0.4 Å^{-1}, depending on the cation, corresponding to a real space distances of 21 and 16 Å, respectively. Charge alternation occurs near 0.8 Å^{-1} corresponding to a real space distance of 8

Å, consistent with computed RDFs. There is also an adjacency peak which forms at 1.5 $Å^{-1}$ corresponding to a length of 4 Å. Examination of the SDFs helps to explain the origin of these features. The anions are attracted to the polar CH group and they tend to occupy four lobes between the short cation alkyl chains. These anions in turn attract other CH groups forming polar domains within the IL. Likewise, the nonpolar CT group doesn't interact much with either the anions or the CH groups, and tends to aggregate with other CT groups. The formation of the polar and non-polar domains gives rise to features in the structure function. The prepeak results from the alternation of the two domains within the IL. The charge alternation feature, which is absent in the total structure functions, results from the alternation of charged species within the polar domain. The peak at 1.5 $Å^{-1}$ results from a multitude of adjacency interactions within the IL between nearest neighbors such as anions immediately solvating the CH group, aggregated CT groups, and small contributions from cations and anions forming the same solvation shell around an ion.

Comparison of experimental and simulated structure functions of CO_2-reactive ILs reveals information about the IL landscape. The experimental structure functions are insensitive to the anion because both anions are similar in size, having five membered rings that undergo similar steric interactions within the IL. Both $[4Triaz]^-$ and $[2CNpyr]^-$ paired with either $[P_{2228}]^+$ or $[P_{66614}]^+$ have structure functions with the same characteristic shapes. However, the ordering lengths are different as determined by the cation.

The structure function doesn't directly reveal the different three dimensional local structure near the anions. $[4Triaz]^-$ has more observed orientations with respect to the cation than does $[2CNpyr]^-$. From the prospective of the cation, however, the two anions behave quite similarly, tending to occupy four high probability lobes between alkyl chains of the CH group. For this reason, both anions end up producing

comparable structure functions.

The reaction with CO_2 has little influence on the overall liquid structure function. There is only a slight change in the structure of $[P_{2228}]^+$ ILs upon reaction with CO_2 and there is no change in the structure of $[P_{66614}]^+$ ILs after reaction. The reaction with CO_2 does cause a slight shift in the anion-anion partial structure functions due to the increased anion size. The added CO_2 does change the product anion charge distribution and thus the orientation towards the phosphorus of the cation, but it does not change the product anion solvation of cation head groups enough to change the liquid structure. This supports experimental evidence that the liquid viscosity does not change much after reaction with CO_2, because the liquid ordering and thus the inter-ionic interactions giving rise to the viscosity don't change when the anion reacts with CO_2. Furthermore, examination of structure functions for different $[4Triaz]^-$ reaction sites shown in Figure 5.9 demonstrate that the total structure function is completely insensitive to the reaction site.

The most significant change in the liquid structure results from cation substitution. Comparison of the corresponding $[P_{2228}]^+$ and $[P_{66614}]^+$ ILs shows that the increased alkyl chain length on both the CH and CT groups results in increased intensities of both the prepeak and the adjacency interaction peak. Increasing the cation size causes the cation-cation partial structure function to split from one to two peaks. One of the cation-cation peaks remains at the original charge alternation location while the other peak is the primary contributor to the adjacency interaction peak. As the alkyl chain lengths increase, there are increased adjacency interactions between cations as both the CT and CH chains start to aggregate with one another. Additionally, the anion-anion partial structure functions in the $[P_{66614}]^+$ ILs form a broad shoulder at small q values, which contributes significantly to the formation of the prepeak. The cation is the major determinant of the IL structure because it has both polar and nonpolar components causing the IL structure to have two dis-

tinct domains. The anions tend to be confined to the same locations near the cation phosphorus atom regardless of the cation size. This well defined structuring of counterions becomes highly pronounced in $[P_{66614}]^+$ ILs because the nonpolar domains are sufficiently large to form continuous percolating networks within the IL.

5.6 Conclusions

The liquid structure functions of AHA ILs are similar to previously studied ILs. The large size of the cation causes the formation of both polar and nonpolar domains within the IL. The correlated structure of these two domains increases with the cation size and its ability to form continuous nonpolar domains. As such, the cation plays the main role in ordering. The anions are only minor players in the liquid structure as different anions tend to occupy the same preferred locations near the phosphorus between the short alkyl chains of the cation. The organization of the polar domains, therefore, is insensitive to the specific anion and whether or not it has reacted with CO_2. Furthermore, the different reaction sites considered on $[4Triaz]^-$ produce nearly identical structure functions.

The total structure functions of reactive AHA ILs don't change appreciably upon reaction with CO_2. The unreacted and CO_2-reacted anions tend to have the same spatial preference relative to the cation. Both the polar and nonpolar domains remain approximately the same before and after reaction so that the total liquid structure function is not dramatically affected by the reaction. This observation helps to explain why the viscosities of these ILs do not change appreciably upon reaction with CO_2.

While many of the experimental systems exhibit similar one dimensional structure functions, the actual structure within the first solvation shell is sensitive to the anion size and charge distribution. However, these effects fail to manifest distinguishable correlated ordering in the outer solvation shells resulting in the same long range

structuring features. The experimental structure function is a good reporter of the ordering length scales but it fails to tell a complete description of the local three dimensional IL liquid structure. MD lends itself to provide further insights in spatial correlations of different species as well as probable orientations of adjacent ions.

CHAPTER 6

CALCULATING CO_2 SOLUBILITIES IN CO_2-REACTIVE APROTIC HETEROCYCLIC ANION IONIC LIQUIDS

Early work on applying ionic liquids (ILs) in CO_2 separations focused on the use of ILs which physically absorbed CO_2 without reacting with it. However, the CO_2 solubilities of these ILs were to small for them to be used in post combustion CO_2 capture due to the low CO_2 partial pressures. Recently, a class of aprotic heterocyclic anion (AHA) ILs have been synthesized that react with CO_2 according to the following reaction scheme

$$\left[C^+ + A^-\right] + CO_2 \leftrightarrow \left[C^+ + A : CO_2^-\right] \tag{6.1}$$

where anions (A^-) will bind CO_2 in a 1:1 reaction stoichiometry, thereby significantly enhancing the CO_2 solubility and making ILs more attractive than conventional amines as potential solvents for CO_2 separations [6, 7, 124, 244, 245]. A simple IL can be made from a multitude of combinations of anions and cations (˜10^6 combinations) [246], which makes it difficult to screen candidate ILs in the laboratory. The vast chemical space for designing ILs necessitates computational methods to estimate CO_2 solubilities in CO_2-reactive ILs and guide the design of candidate ILs prior to synthesis and experimental measurement.

When solutes do not react in the solvent environment, the physical solubility is relatively easy to compute. Physical solubility can be estimated in an indirect way using free energy methods in CMD simulations to calculate excess chemical

potentials and Henry's Law constants [12, 111]. Physical absorption isotherms can be calculated directly using Gibbs ensemble Monte-Carlo simulations to determine equilibrium compositions of liquid and vapor phases over a range of thermodynamic states [135, 141, 247]. When solutes undergo chemical reactions in the solvent environment, however, calculating solubilities becomes increasingly more difficult as the reaction equilibria involves bond formation that can only be modeled using quantum calculations.

The first attempts to estimate CO_2 solubilities in CO_2-reactive ILs were based on the gas phase reaction of anions with CO_2 [6, 7, 126]. The gas phase enthalpy of reaction, neglecting cation interactions, was used to rank the relative CO_2 solubilities of various ILs with different anions. Although the calculated gas phase reaction enthalpies gave rough estimates of IL reactivity at a relatively low computational cost, they did not always give qualitative solubility trends when compared to experimental data [7]. Furthermore, the enthalpy of reaction cannot be used to quantitatively predict the reaction equilibria for IL-CO_2 systems that is needed to determine the IL performance limits in CO_2 separations.

Quantitative prediction of CO_2 solubilities in CO_2-reactive ILs can be be achieved by calculating the Gibbs free energy of reaction. Firaha *et al.* calculated the free energy of reacting CO_2 with ILs by determining solvated geometries of reacted and unreacted anions using COSMO-RS [128]. They used the solvated ion geometries to estimate the free energy of reaction, which gave significant improvement over the use of gas phase geometries to calculate reaction free energies. The reaction free energies from the solvated ion geometries were in qualitative agreement with experimental CO_2 solubilities, and in many cases quantitative agreement with free energies obtained by fitting isotherm models to experimental data. Implicit solvation models, however, are not always capable of modeling solvents with micro-heterogeneous charged regions that will polarize the solute molecule [248–250].

The free energy of reaction can also be calculated using explicit solvation models. An explicit solvation model could improve the quality of results as implicit solvent models neglect specific interactions in the system when the local solvation environment is non-homogeneous [251]. It is difficult to calculate the free energy of reaction quantum mechanically using an explicit solvation environment due to difficulties in proper solvent conformational sampling and system size limitations. Free energy, however, is a state function and therefore any thermodynamic cycle that takes the reactants to the product state will give the correct free energy of reaction. By using a thermodynamic cycle, it is therefore possible to explicitly account for the effects of the local solvation environment on the free energy of reaction without directly performing quantum calculations on the solvent.

In this work, we propose a computational approach to predict CO_2 solubilities in CO_2-reactive IL systems. All of the model parameters for the free energy of reaction were obtained using CMD and *ab initio* simulations, making it a general predictive method. Solvation environment effects of large systems were calculated using CMD simulations, which allowed the reaction to be modeled using a small enough gas phase system for high level *ab initio* calculations. Several researchers have employed thermodynamic cycles to account for solvation effects on reaction thermodynamics, typically using either an implicit solvation model or quantum mechanical/molecular mechanical methods [252–254]. In this work, the effects of the solvation environment on reaction thermodynamics are directly modeled in a rigorous manner using CMD free energy methods and direct simulation of both liquid and vapor phases. The method was tested for an IL with a triethyl-octyl-phosphonium cation ($[P_{2228}]^+$) paired with a 2-cyanopyrrolide anion ($[2CNpyr]^-$), as this is one of the most widely studied AHA anions[6, 7, 255]. Figure 6.1 shows the structure of the cation along with the reacted and unreacted anion. CO_2 absorption isotherms were calculated at 300, 333, and 360 K to examine the CO_2 solubility temperature and pressure

dependence. The $[P_{2228}][2CNpyr]$ system was used to demonstrate the method while highlighting the relative free energy contributions of the gas phase reaction, solvation environment effects, and the extent of reaction.

6.1 Method

6.1.1 Thermodynamic Cycle

In this work, a method is presented for calculating the reaction equilibrium between CO_2 and AHA ILs, which is shown as step 1 in Figure 6.2. During this reaction in $[P_{2228}][2CNpyr]$, the CO_2 will bond to the ring nitrogen of the $[2CNpyr]^-$ anion as shown in Figure 6.1.

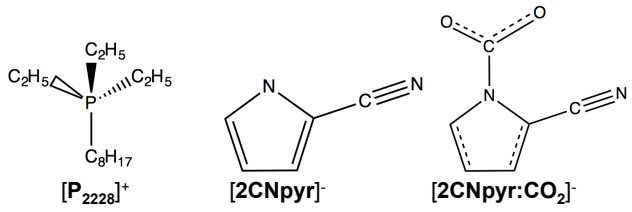

Figure 6.1. Molecular structures of the cation, the anion, and the reacted anion.

The reaction equilibria for the IL-CO_2 system can be found by calculating the free energy of reaction as a function of temperature, pressure, and composition. This calculation is simplified by breaking the reaction into several smaller steps to form the thermodynamic cycle shown in Figure 6.2.

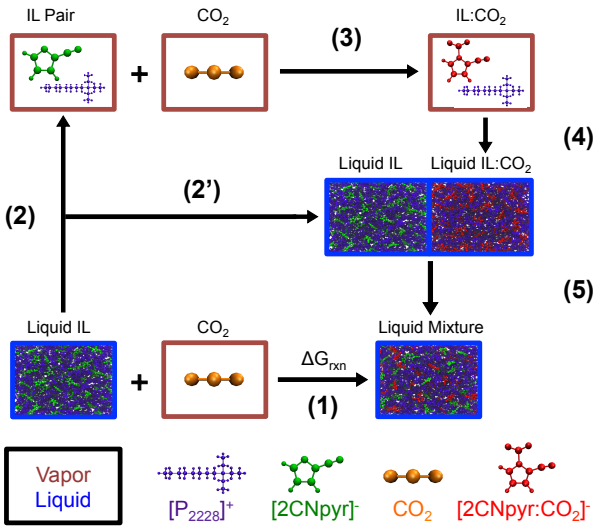

Figure 6.2. Thermodynamic free energy cycle for the reaction of CO_2 in IL (1). Free energies are determined based upon the following steps: (2) vaporization of IL at constant T and P; (2') a portion of the unreacted IL remains liquid and is mixed with reacted IL in step 5 (3) reaction of IL with CO_2 in the gas phase; (4) condensation of the CO_2-reacted IL vapor at constant T and P; (5) mixing of the unreacted IL with the CO_2-reacted IL. The overall free energy of reaction depends on the extent of reaction. Steps 2 through 4 have a linear dependence on the extent of reaction, while the free energy of mixing in step 5 has a nonlinear dependence on the extent of reaction.

Solvation environment effects in steps 2, 4, and 5 are calculated using CMD simulations. The free energy of the gas phase reaction in step 3 is calculated using *ab initio* methods. The free energy change for the entire cycle is given by

$$\Delta G_{rxn}(\xi) = \xi\left(\Delta G^{IL}_{vap} + \Delta G^{g}_{rxn} - \Delta G^{IL:CO2}_{vap}\right) + \Delta G^{l}_{mix}(\xi) \tag{6.2}$$

where ΔG_{rxn} is the free energy of the overall reaction (step 1), ΔG^{IL}_{vap} is the free energy of vaporization of the unreacted IL (step 2), ΔG^{g}_{rxn} is the free energy of the gas phase reaction (step 3), $\Delta G^{IL:CO2}_{vap}$ is the free energy to vaporize the CO_2-reacted

IL (step 4), and ΔG^{l}_{mix} is the free energy of mixing unreacted IL with CO_2-reacted IL (step 5) with all quantities in kJ mol^{-1}. The free energy of reaction depends on the extent of reaction, ξ, which is defined as the mole fraction of anions that have reacted with CO_2.

In the following subsections, the methods used to calculate the free energy contribution of each piece of the thermodynamic cycle along with the assumptions used in each calculation are discussed. The complete computational details of both the CMD and *ab initio* calculations are provided in the Simulation Details section.

6.1.2 Vaporization and Condensation: Steps 2 and 4

The free energy changes in steps 2 and 4 are given by the free energy of vaporization/condensation of the unreacted and CO_2-reacted IL, respectively. In the thermodynamic cycle, the difference in the free energy changes of steps 2 and 4 has a linear dependence on the extent of reaction, and therefore, we calculated the combined free energy change of steps 2 and 4

$$\Delta\Delta G_{vap} = \Delta G^{IL}_{vap} - \Delta G^{IL:CO2}_{vap}. \tag{6.3}$$

$\Delta\Delta H_{vap}$ and $\Delta\Delta S_{vap}$ are defined similarly.

We used two different methods to calculate $\Delta\Delta G_{vap}$; each method will be indicated by a superscript. In the first method, $\Delta\Delta G^{BAR}_{vap}$ was calculated using the Bennett Acceptance Ratio (BAR) method [134]. In a second method, $\Delta\Delta G^{ST}_{vap}$ was calculated by estimating $\Delta\Delta H_{vap}$ from CMD simulations [256–259] and $\Delta\Delta S_{vap}$ from the Sackur-Tetrode (ST) equation for the translation entropy of an ideal gas [260]. The combined entropy change using the ST approximation is

$$\Delta\Delta S_{vap} = R \ln\left(\frac{m^{IL}}{m^{IL:CO2}}\right) \tag{6.4}$$

where m^{IL} is the molar mass of the unreacted cation-anion pair and $m^{IL:CO2}$ is the molar mass of the CO_2-reacted cation-anion pair.

6.1.3 Gas Phase Reaction: Step 3

The free energy of the gas phase reaction was calculated using two different *ab initio* methods. The first and simplest method was to calculate the free energy of reaction using the harmonic oscillator and rigid rotor approximations. This method was applied to two different reaction scenarios: the *anion-only* reaction scheme

$$[2CNpyr]^{-}(g) + CO_2(g) \rightarrow [2CNpyr : CO_2]^{-}(g) \tag{6.5}$$

and the *ion-pair* reaction scheme

$$[P_{2228}][2CNpyr](g) + CO_2(g) \rightarrow [P_{2228}][2CNpyr : CO_2](g). \tag{6.6}$$

The partition functions of the products and reactants in eqs. 6.5 and 6.6 were evaluated by calculating the vibrational frequencies of the optimized product and reactant gas phase geometries. The partition function calculations assume that vibrational modes are accurately modeled using the harmonic oscillator approximation and that rotational motion is accurately modeled within the rigid rotor approximation. Using these assumptions, the total partition function of a molecule can be calculated with eq. 6.7

$$q = q_{trans} q_{rot} q_{vib} q_{elec} \tag{6.7}$$

where the partition functions for the various degrees of freedom are defined as

$$q_{trans}(V,T) = \left(\frac{2\pi m}{h^2 \beta}\right)^{\frac{3}{2}} V \tag{6.8}$$

$$q_{vib}(T) = \prod_{j=1}^{3n-6} \frac{e^{\frac{-\beta h\nu_j}{2}}}{1 - e^{-\beta h\nu_j}} \tag{6.9}$$

$$q_{rot}(T) = \frac{\sqrt{\pi}}{\sigma} \left(\frac{8\pi^2 I_A}{h^2\beta}\right)^{\frac{1}{2}} \left(\frac{8\pi^2 I_B}{h^2\beta}\right)^{\frac{1}{2}} \left(\frac{8\pi^2 I_C}{h^2\beta}\right)^{\frac{1}{2}} \tag{6.10}$$

where m is the molecular mass, β is the Boltzmann factor, $\frac{1}{k_B T}$, h is Planck's constant, n is the number of atoms in the molecule, ν is a vibrational frequency, σ is the symmetry factor, and I_A, I_B, and I_C are the principle moments of inertia of the molecule. The electronic partition function is approximately one for all of the reaction species because the spacing between electronic energy levels is much greater than the thermal energy at the temperatures studied. The free energy of the gas phase reaction can be calculated as $\Delta G_{rxn} = \Delta H_{rxn} - T\Delta S_{rxn}$. The enthalpy, H, is defined as $H = U + PV$. The internal energy, U, and the entropy, S, can be calculated for the product and reactant species using eqs. 6.11 and 6.12 respectively [261]

$$U = \langle E \rangle = k_B T^2 \left(\frac{\partial \ln q}{\partial T}\right)_{N,V} \tag{6.11}$$

$$S = k_B \ln(q) + k_B T \left(\frac{\partial \ln q}{\partial T}\right)_{N,V} \tag{6.12}$$

where all variables have their previous definitions. The anion only model is the simplest method to calculate the free energy of the gas phase reaction, and therefore, it serves as a benchmark for comparison with more complicated methods.

A second method which avoids the harmonic oscillator and rigid rotor approximations is to calculate the free energy of the gas phase reaction from the potential of mean force (PMF) [262, 263]. To calculate the PMF, a series of *ab initio* molecular dynamics (AIMD) simulations of an ion pair with a single CO_2 were run where the carbon-nitrogen bond length between CO_2 and $[2CNpyr]^-$ was held fixed by applying

the necessary constraint force. The average constraint force was sampled at several constraint lengths from the bonded state to the unbonded state. The PMF is related to the average constraint force by

$$\frac{dW(r)}{dr} = -\langle F(r) \rangle \tag{6.13}$$

where *W(r)* is the PMF and $\langle F(r) \rangle$ is the average value of the constraint force at a given constraint length, r. The free energy of the gas phase reaction is

$$\Delta G^{\circ}_{rxn} = -RT \ln \left[4\pi \int_0^{r^*} r^2 e^{-\beta[W(r)-W(r_D)]} dr \left(\frac{P^{\circ}}{k_B T} \right)^{-\Delta\nu} \right] \tag{6.14}$$

where r^* is the distance where the CO_2 is no longer bound to the anion and r_D is the longest distance in the PMF calculation at which W(r_D) and its first derivative are both zero. The complete derivation of eq. 6.14 is shown in Appendix E.

6.1.4 Liquid Mixing: Step 5

The thermodynamic properties of mixing unreacted IL with CO_2-reacted IL were investigated by simulating mixtures ranging from unreacted to fully CO_2-reacted IL in 0.1 mole fraction intervals. The thermodynamics of mixing unreacted IL and CO_2-reacted IL were calculated using an ideal solution model

$$\Delta G^{Ideal}_{mix} = -T \Delta S^{Ideal}_{mix} \tag{6.15}$$

where the entropy of mixing for an ideal solution, ΔS^{Ideal}_{mix}, is given by

$$\Delta S^{Ideal}_{mix} = -R \sum_{x_i} x_i \ln (x_i) \tag{6.16}$$

where the summation is taken over the component mole fractions, x_i. The molar

entropy of mixing for a binary mixture of unreacted IL and CO_2-reacted IL is

$$\Delta S_{mix}^{Ideal} = -R\left[\xi \ln\left(\xi\right) + \left(1-\xi\right)\ln\left(1-\xi\right)\right] \tag{6.17}$$

where the extent of reaction, ξ, is given by the mole fraction of reacted anions. The validity of the ideal solution model is confirmed in the results section.

6.1.5 Full Cycle

The free energy of reaction combining all of the steps in the thermodynamic cycle is

$$\begin{aligned}\Delta G_{rxn}(\xi, P, T) =& \xi\left[\Delta G_{gas}^{\circ} + \Delta\Delta G_{vap} - RT\ln\left(\frac{m^{IL}}{m^{IL:CO2}}\right)\right] \\ &+ RT\left[\xi\ln(\xi) + (1-\xi)\ln(1-\xi)\right] \\ &- \xi RT\ln\left(\frac{P}{P^{\circ}}\right).\end{aligned} \tag{6.18}$$

The expression for the free energy of reaction can be used to calculate a reaction isotherm by specifying T and P and determining the value of ξ that minimizes the free energy of reaction. The value of the quantity $\left(\Delta G_{gas}^{\circ} + \Delta\Delta G_{vap}\right)$ determines the solubility of CO_2 in a given IL with a more negative value indicating a higher solubility.

6.2 Simulation Details

6.2.1 CMD Simulations

All of the CMD simulations were run with GROMACS 4.5.5 [194–196] using initial structures generated by Packmol [198]. The vapor phase was simulated as a single ion pair in a non-periodic 10 nm box. Coulomb and Lennard-Jones (LJ) interactions were

calculated using a plain cut-off of 20 nm. LJ parameters ϵ_{ij} and σ_{ij} were calculated using Lorentz-Berthelot combining rules [243]. The vapor systems were equilibrated for 10 ns in the NVT ensemble using a Nosé-Hoover thermostat [200, 201] followed by 25 ns production run while sampling energies every ps. Ten simulations with different initial configurations were run in order to get good statistics. The standard deviation of the total energy between the replicate runs was used as an uncertainty estimate for the vapor phase enthalpy.

The enthalpy of mixing as well as the volume of mixing were calculated by simulating 200 ion pair liquid mixtures with compositions ranging from unreacted to fully CO_2-reacted IL. Both LJ and Coulomb interactions used a switch potential with a 1.2 nm cutoff and a switch applied at 1.15 nm. Long range corrections to the LJ potential were applied to energy and pressure. Following an initial steepest descent energy minimization, the systems were annealed to 700 K in the NVT ensemble for 500 ps. Then an equilibration was performed for 8 ns in the NPT ensemble with a Berendsen thermostat and barostat [199]. A final NPT equilibration using Nosé-Hoover thermostat [200, 201] and a Parrinello-Rahman barostat [202] was performed for 2 ns. After equilibration, a production run of 4 ns was run sampling energies every ps using the same run parameters as the final equilibration. For all simulations, a 1 fs time step was used and all covalent bonds to hydrogen were constrained using the LINCS algorithm to allow a larger time step to be used [203].

6.2.2 Solvation Free Energy Calculations

The free energy of solvation was calculated using the Bennett Acceptance Ratio (BAR) method as implemented in GROMACS version 4.5.5 [134]. The simulations work by creating a function of the potential that depends on a coupling parameter, λ, which scales the interaction between the solute and surrounding solvent. The details of the BAR method and similar free energy perturbation methods can be found in

Bennett's original paper and several other works [134, 213, 214]. The difference in the solvation free energies of an unreacted cation-anion pair and a CO_2-reacted cation-anion pair is

$$\begin{aligned} \Delta\Delta G_{vap} &= -\Delta\Delta G_{solv} \\ &= \Delta G_{solv}^{IL:CO2} - \Delta G_{solv}^{IL} \\ &= \Delta G_{vap}^{IL} - \Delta G_{vap}^{IL:CO2} \end{aligned} \tag{6.19}$$

where ΔG_{solv}^{IL} is the free energy to solvate an unreacted cation-anion pair in unreacted IL and $\Delta G_{solv}^{IL:CO2}$ is the free energy to solvate a CO_2-reacted cation-anion pair in fully reacted IL.

Calculating the solvation free energy for an ion pair requires the calculation of the solvation free energy for the anion and a separate calculation for the solvation free energy of the cation. The solvation free energy for an ion can be broken up into two parts:

$$\Delta G_{solv} = \Delta G_{solv}^{vdW} + \Delta G_{solv}^{Q}$$

where ΔG_{solv}^{vdW} is the van der Waals contribution to the solvation free energy and ΔG_{solv}^{Q} is the electrostatic contribution to the solvation free energy. The solvation free energy of a single ion was calculated using a two step approach. In the first step, the electrostatic contribution to the solvation free energy was calculated. During this step the charges on the solute molecule were the same as the equivalent solvent molecule. Several simulations were run ranging from full electrostatic interactions between solute and solvent molecules to a non-interacting state where solute charges were effectively "turned off".

In a second step, the van der Waals contribution to the solvation free energy

was calculated. During this step, charges on the solute molecule were set to zero to prevent particle overlap that might effect the simulation stability and convergence. Similar to the electrostatics, several intermediate simulations were run between full solute-solvent LJ interaction and the solute not interacting with the solvent via LJ interaction.

6.2.3 PMF

The PMF simulations were performed using Car-Parrinello molecular dynamics (CPMD) [264]. For each PMF simulation, a single cation with an anion-CO_2 complex was placed in a 15 Å cubic box with periodic boundary conditions. The Kohn-Sham orbitals were expanded using a plane wave basis set with a cutoff of 30 Ry. An electronic mass of 400 a.u. and a time step of 0.12 fs were used. All hydrogens were substituted with deuterium atoms in order to allow a larger time step to be used. An empirical van der Waals correction was applied to ion pairs using Grimme's damped dispersion model. Temperature was controlled using a Nosé-Hoover thermostat. The constraint force was sampled along the reaction coordinate from a distance between the $[2CNpyr]^-$ ring nitrogen and the CO_2 carbon from 1.1 to 2.8 Å in 0.1 Å increments, from 2.8 to 4.2 Å in 0.2 Å increments, and from 4.2-5.8 Å in 0.4 Å increments. At each distance interval, a constraint was placed on the C-N distance and the system was equilibrated for 5 ps followed by a 5 ps production run where the constraint force was sampled every ten steps. Two simulations where run at each constraint distance starting from different initial configurations in order to sample a diverse set of ion configurations. The resulting constraint forces at each constraint length were then averaged. The PMF profiles were calculated by trapezoid integration of the average constraint forces over the constraint distances using eq. 6.13.

6.2.4 Partition Function Calculations

Two different models were used to get the free energy of the gas phase reaction using calculated partition functions. For the *anion-only* model, the geometry was optimized followed by a frequency analysis using a PBEPBE/aug-cc-pvdz basis set. Extensive benchmarking was performed on a family of AHA ILs indicating that this method gives excellent agreement with higher levels of theory. In the *ion-pair* model, the cation was included in the reaction.

To get initial configurations for the *ion-pair* model, a CPMD simulation was run for 10 ps using the same run options from the PMF calculations with no constraints applied. The production trajectory was broken into 10 equal length trajectories and the lowest energy configuration from each was taken for further analysis. Using these minimum energy configurations, an initial geometry optimization was performed using PBEPBE/6-31g+(d,p) basis set. Following the initial optimization each structure was re-optimized and a frequency analysis was performed using PBEPBE/6-311g+(d,p) basis set. The *ion-pair* calculations gave free energies that were lower than those from the *anion-only* model by several kJ mol^{-1}. All isotherms predicted using the gas phase free energy of reaction from the *ion-pair* model saturated at very low CO_2 pressure. The *ion-pair* calculations do not give accurate free energies of reaction for two reasons: the ion pairs have several low frequency modes due to the motions of the counterions, and it is difficult to sample the thermodynamically relevant configurations due to the large configurational space of an ion pair relative to that of a single ion. Therefore, results for the free energy of the gas phase reaction obtained from the *ion-pair* model were excluded from further analysis and isotherm prediction.

6.3 Results

Results for the free energy contributions from the different steps in the thermodynamic cycle are summarized in Table 6.1. The enthalpy of vaporization is larger for the CO_2-reacted IL than for the unreacted IL. This difference is due to increased van der Waals interactions with the addition of the CO_2 moiety to the anion. The enthalpy of vaporization from 300 to 360 K ranged from 153 to 165 kJ mol^{-1} and 161 to 172 kJ mol^{-1} for unreacted and CO_2-reacted IL, respectively. These values are comparable to both experimental measurements and calculations on similar ILs with the enthalpy of vaporization across a broad range of ILs varying from 100 to 200 kJ mol^{-1} [257, 265].

TABLE 6.1

FREE ENERGY CHANGES FOR THE THERMODYNAMIC CYCLE

Temperature (K)	300	333	360
$\Delta\Delta H_{vap}$	-6.72 ± 0.82	-7.79 ± 0.48	-7.80 ± 0.34
-T$\Delta\Delta S_{vap}$	0.32	0.36	0.39
$\Delta\Delta G^{ST}_{vap}$	-6.40 ± 0.82	-7.43 ± 0.48	-7.41 ± 0.34
$\Delta\Delta G^{BAR}_{vap}$	-8.60 ± 2.28	-10.64 ± 1.60	-6.85 ± 1.15
Anion-Only ΔG°_{gas}	-1.7	3.1	7.1
PMF ΔG°_{gas}	0.9	7.3	9.7

Values given are in kJ mol^{-1}. Uncertainties are based on block averaging of five equal space intervals of the CMD trajectories.

The calculated values for $\Delta\Delta G_{vap}^{ST}$ and $\Delta\Delta G_{vap}^{BAR}$ are similar; there is only a statistical difference in these values greater than one standard deviation at 333 K. The fact that $\Delta\Delta G_{vap}^{BAR} \approx \Delta\Delta G_{vap}^{ST}$ suggests that the difference in the gas phase translational entropy of the unreacted and CO_2-reacted IL provides a good estimate for $\Delta\Delta S_{vap}$. We caution that this result, however, may simply be a fortuitous cancellation of errors from combining the thermodynamics of the vaporization and condensation steps. Yet it appears that the assumptions used to calculate $\Delta\Delta S_{vap}$ are sufficient for the present purpose of calculating the overall free energy of reaction. Calculating $\Delta\Delta G_{vap}^{ST}$ only requires two liquid simulations and two vapor phase simulations whereas calculation of $\Delta\Delta G_{vap}^{BAR}$ requires 120 liquid simulations. One may therefore choose to use the less computationally intensive approximate calculation of $\Delta\Delta G_{vap}^{ST}$ for screening larger data sets and to use $\Delta\Delta G_{vap}^{BAR}$ to investigate only the most promising candidates.

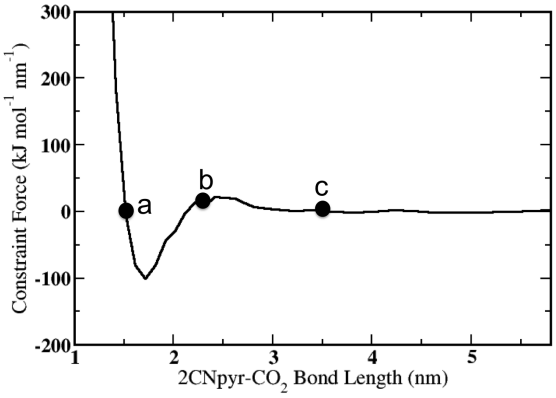

(a)

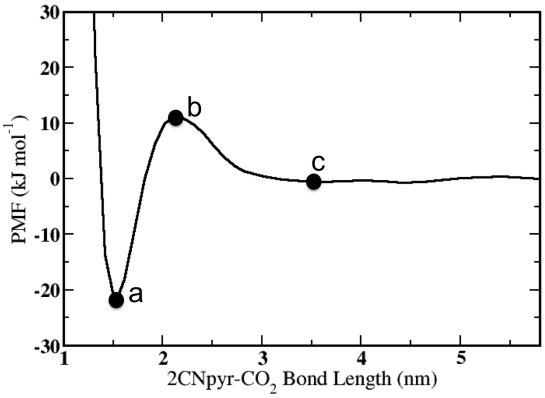

(b)

Figure 6.3. Average constraint force profile (a) and PMF (b) for at 300 K.

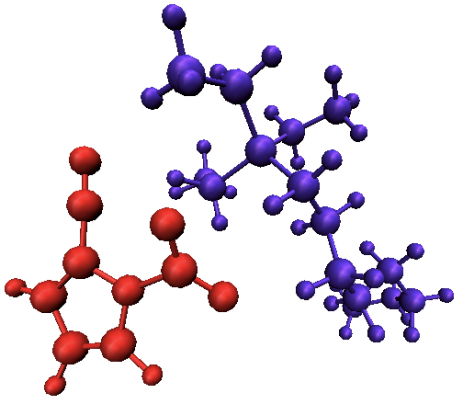

(a)

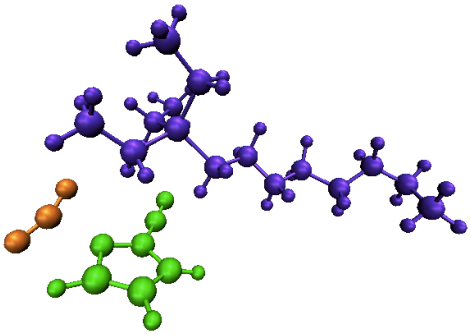

(b)

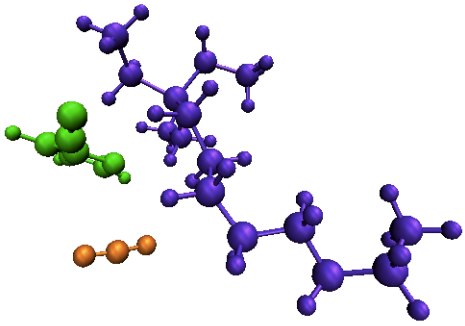

(c)

Figure 6.4. Example geometries from the 300 K PMF trajectories. Configurations a, b, c correspond to the points marked in Figures 6.3a and 6.3b.

Figures 6.3a and 6.3b show the constraint force profile and PMF profile at 300 K, respectively. Snapshots of example configurations from the PMF simulations at different constraint lengths of the C-N bond between $[2CNpyr]^-$ and CO_2 are shown in Figures 6.4a, 6.4b and 6.4c. As the CO_2 moves far enough away from the anion that the two species do not interact, the CO_2 angle approaches 180° and there is zero constraint force.

The PMF and the *anion-only* methods calculate values for ΔG°_{gas} within 4 kJ mol^{-1} of each other. The free energy of the gas phase reaction is lower for the anion only model than the PMF model at all temperatures. The calculated values for the free energy of the gas phase reaction show the expected temperature trend: increasing with increasing temperature. To leading order, the free energy of reaction should have a linear temperature dependence assuming that the enthalpy of reaction and entropy of reaction are approximately constant over the temperature range studied. An approximately linear temperature dependence is seen in calculated reaction free energies from both models. The magnitude of the Gibbs free energy of reaction in the gas phase is comparable to the solvation environment effects. In previous work, solvation effects were assumed to be negligible contributing < 5 kJ mol^{-1} to the enthalpy of reaction and were neglected in solubility predictions [126].

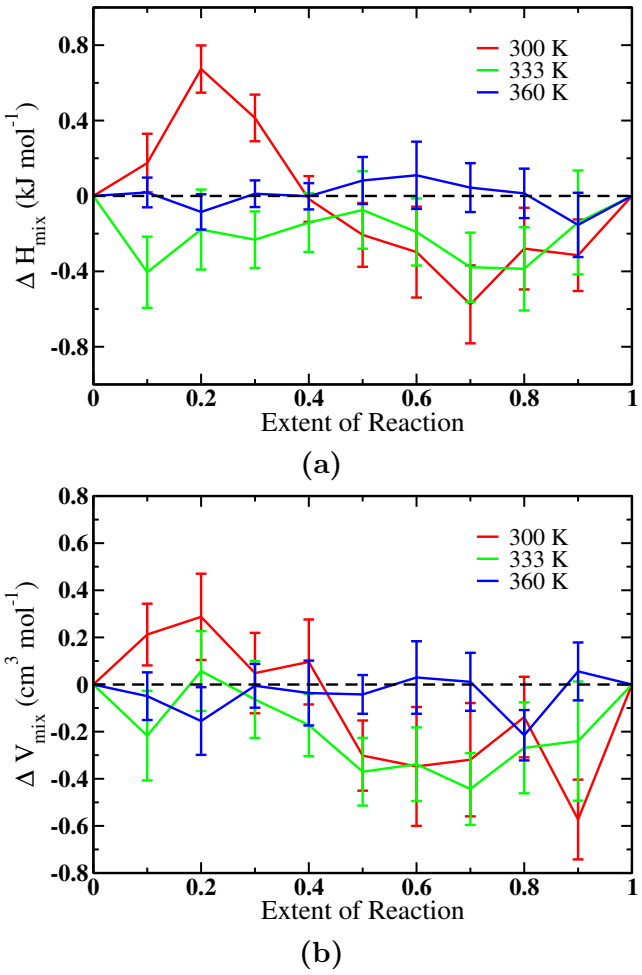

Figure 6.5. Excess enthalpy (a) and excess volume (b) for mixing reacted and unreacted $[P_{2228}][2CNpyr]$ at 300, 333, and 360 K as a function of extent of reaction. Uncertainties are based on block averaging of the enthalpies and volumes of the mixture, the unreacted IL, and the fully reacted IL.

The results for the excess enthalpy and the excess volume are shown in Figures 6.5a and 6.5b, respectively. The magnitude of the excess enthalpy is less than 0.7 kJ mol^{-1} at all temperatures over the full range of compositions. Additionally, the excess enthalpy shows contrasting behavior at different temperatures. At a given

composition, the excess enthalpy is positive for some temperatures and negative for others. Although the excess enthalpy is nonzero, it does not have an apparent trend with the extent of reaction. The small magnitude of the excess enthalpy compared to the rest of the terms in the free energy cycle suggests that the enthalpy of mixing is reasonably approximated as zero for the full range of compositions.

The excess volume shows similar behavior to the enthalpy of mixing. The magnitude of the excess volume is less than 0.6 cm^3 mol^{-1} for all temperatures over the full composition range. Analogous to the enthalpy of mixing, the excess volume is different at each temperature and shows no apparent compositional trend. Therefore, the excess volume is well approximated as zero. These results suggest that mixtures of unreacted IL and CO_2-reacted IL exhibit ideal solution behavior. Both the enthalpy of mixing and the excess volume are negligible, and therefore, it is appropriate to estimate thermodynamic properties of mixing using ideal solution theory.

6.4 Discussion

The free energy of reacting CO_2 with AHA ILs can be calculated analytically using eq. 6.18. The model parameterization for a given IL requires the calculation of three different thermodynamic properties: the vaporization free energy of the unreacted IL, the free energy of reacting IL and CO_2 in the gas phase, and the vaporization free energy of the CO_2-reacted IL. All of these parameters can be calculated without using experimental data for fitting, and therefore, it can be used to investigate ILs that lack experimental data. The free energy of reaction can be used to calculate an absorption isotherm for low pressures up to 1 bar. At these low pressures, the absorption is dominated by chemical reaction and the physical absorption capacity is negligible ($< 3\%$) [266]. CO_2 absorption isotherms can be predicted by calculating the extent of reaction that minimizes the free energy of reaction at a fixed temperature and pressure. The shape of the isotherm is determined by the quan-

tity $\left(\Delta G^{\circ}_{gas} + \Delta\Delta G_{vap}\right)$, which contains all relevant information about the solvation environment effects as well as the free energy of the gas phase reaction.

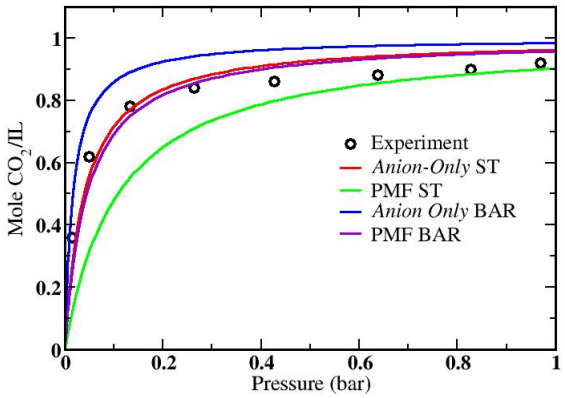

Figure 6.6. Comparison of experimental [16] and predicted isotherms at 300 K.

A comparison of predicted isotherms at 300 K is shown in Figure 6.6. The anion only model combined with the ST assumption predicts an isotherm in very close agreement with the PMF BAR isotherm and the experimental isotherm. The predicted isotherms vary significantly from differences of only a few kJ mol^{-1} in the model parameters. This sensitivity is due to the fact that the reaction equilibria has an exponential dependence on the free energy of reaction. Therefore, it is extremely challenging to predict isotherms that are in quantitative agreement with experimental results due to the accumulation in uncertainty from the calculation of each thermodynamic quantity.

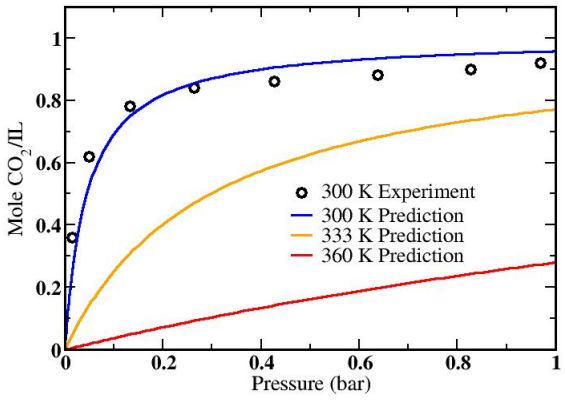

Figure 6.7. Temperature dependence of predicted isotherms using the PMF method to calculate the free energy of the gas phase reaction and the BAR method to calculate $\Delta\Delta G_{vap}$.

The combination of the PMF method to calculate the free energy of the gas phase reaction and the BAR method to calculate $\Delta\Delta G_{vap}$ represents the most robust method used to estimate the free energy of reaction. Calculated absorption isotherms using the PMF and BAR methods are shown in Figure 6.7. At 300 K, the predicted isotherm is in excellent agreement with published solubility data. There is no data to compare with at 333 and 360 K, however, the predicted isotherms do show the expected behavior that the solubility decreases with increasing temperature.

Table 6.2 shows the calculated free energy of reaction for the different methods and temperatures at a pressure of 0.9 bar. The values for the free energy of reaction at 0.9 bar are in excellent agreement with the value of -7 kJ mol^{-1} obtained by Firaha *et al.* [128]. The combination of the PMF and BAR methods not only predicts the best isotherm, but it also predicts a free energy of reaction closest Firaha's.

TABLE 6.2

FREE ENERGY OF REACTION AT 0.9 BAR

Temperature (K)	300	333	360
Anion-Only ST	-8.1	-4.6	-2.1
PMF ST	-5.6	-1.9	-1.1
Anion-Only BAR	-10.3	-7.4	-1.8
PMF BAR	-7.6	-3.9	-0.9

Values given are in kJ mol^{-1}.

6.5 Conclusions

A thermodynamic cycle was used to calculate the free energy of reacting CO_2 with an AHA IL as an analytical function of temperature, pressure, and composition. The free energy of the gas phase reaction was calculated in two ways: 1) frequency calculations for the reaction of anions with CO_2 using the rigid rotor and harmonic oscillator approximations, 2) using constraint AIMD simulations to calculate the PMF for the reaction of a single cation-anion pair with CO_2. The free energy effects of the solvation environment were modeled in a rigorous manner using CMD simulations rather than using an implicit solvent. The expression for the free energy of reaction can be used to predict CO_2 absorption isotherms in AHA ILs at low pressures where the physical solubility of CO_2 is negligible. The method is sensitive to calculated model parameters, with a few kJ mol^{-1} change in the parameters significantly affecting the shapes of predicted isotherms. The ability of the model to quantitatively predict CO_2 absorption isotherms in AHA ILs improves as more robust methods are used to calculate the free energy the gas phase reaction and the free energy contribution of solvation environment effects. Calculations using cheaper methods which depend on more assumptions don't predict isotherms as well, but they do present a way to com-

pare a larger number of ILs for screening purposes. The PMF method to calculate the free energy of the gas phase reaction allows the comparison of ILs with the same anion and different cations.

Several important findings were revealed in this study with regards to the interactions which control the CO_2 solubility in an AHA IL. The free energy effects of the solvation environment are on the order of 10 kJ mol^{-1}, which is comparable to the free energy of the gas phase reaction. We conclude that solution effects on the reaction cannot be ignored. The effects of the solvation environment can be approximated using less computationally expensive enthalpy of vaporization calculations as opposed to the direct calculation of ion solvation free energies using computationally intensive free energy methods. Calculation of the free energy of the gas phase reaction showed that the reaction thermodynamics are affected by the presence of the cation. Simulated mixtures of unreacted IL and CO_2-reacted IL exhibit ideal solution behavior. Therefore, thermodynamic properties for mixtures of these species can be assessed using ideal solution theory. The results presented in this work are important to consider in future models that attempt to predict gas solubilities in reactive liquids.

CHAPTER 7

SUMMARY

Ionic liquids (ILs) are promising solvents for a variety of industrial applications. Aprotic heterocyclic anion (AHA) ILs that are able to chemically bind CO_2 are of particular interest as solvents that might outperform current amine technologies in CO_2 separations. These ILs have several properties that make them more appealing than amines. They have low vapor pressures, which prevents solvent evaporation, along with high thermostabilities, which allows them to be used in a wide temperature range. The absorbed CO_2 can be desorbed by heating and the original IL recovered. This ability to react with CO_2 in a reversible manner allows them to be used in typical stripper/absorber configurations that are common in oil and natural gas processing. The most interesting aspect of these ILs, however, is the ability to tune both the physical and chemical properties of the ILs simultaneously by changing the chemical nature of the cations and anions. This ability to tune both the physical and chemical properties of AHA ILs offers a great design opportunity, but also a challenge because it is difficult to know *apriori* how a given change in the chemical structure of the ions will affect different liquid properties and reaction chemistries. Furthermore, there is an essentially infinite design space for pairing different anions and cations together to form an IL. It is therefore desirable to have computational methods whereby different IL properties can be estimated and understood in terms of the chemical structures of the ions.

In this dissertation, several different computational methods were used to increase our current understanding of AHA ILs. A combination of classical molecular

dynamics (MD) simulations as well as *ab initio* calculations and *ab initio* molecular dynamics (AIMD) simulations were used to calculate different chemical and physical properties of select AHA ILs. The liquid structure and dynamics of both pure ILs and IL-water mixtures were investigated using a series of MD simulations. The liquid structure functions were both measured and computed for a series of ILs made from systematically pairing different cations and anions. A method was created to calculate CO_2 absorption isotherms. Each of these works revealed new information about the behavior of AHA IL systems.

In the first work of this dissertation, MD simulations were used to investigate how water effects both the structure and dynamics of various CO_2-reactive ILs having either azolide or phenolate anions. MD simulations of both pure ILs and 1:1 mole ratio water/IL were simulated for a series of ILs having a triethyl-octyl-phosphonium cation ($[P_{2228}]^+$) paired with the anions 2-cyanopyrrolide ($[2CNpyr]^-$), 1,2,3-triazolide ($[3Triaz]^-$), and phenolate ($[PhO]^-$). These simulations showed that the ion self-diffusivities in the $[2CNpyr]^-$ and $[3Triaz]^-$ approximately doubled when water was added, whereas the dynamics in the $[PhO]^-$ system were practically unaffected by the added water. Simulation studies and experiments for other ILs have shown that the dynamics will increase when water is added. These earlier simulation studies concluded that the dynamics increase when water is added due to a decrease in counterion interactions. If the counterion attraction weakens, it allows the ions to translate and rotate more freely, and therefore, the dynamics will increase. In this work, we found a similar effect occurring in the $[2CNpyr]^-$ and $[3Triaz]^-$ systems. Structural analysis showed that water will primarily interact with the anions in the system, forming hydrogen bonds with the negatively charged anion atoms which the positively charged cation atoms are attracted to. The interactions between water and the anions are quite strong, and the water will tend to occupy space between the negative anion atoms and the positive cation atoms. This results in reduced

counterion attraction due to the electrostatic screening facilitated by the water, and results in increased system dynamics.

Structural analysis shows that a water also reduces counterion interactions in the $[PhO]^-$ systems. Water forms intimate contacts with the $[PhO]^-$ oxygen atom which has the majority of the anionic charge. Structural analysis reveals a change in the phenolate systems that does not occur in the other ILs where the $[PhO]^-$ anions form associated clusters with water acting to bridge adjacent anions. The formation of these associated clusters prevents the the dynamics from increasing when water is added because it restricts both the cation motions and anion motions.

The behavior of wet CO_2-reactive ILs can be understood in terms of the abilities of the anions to form hydrogen bonds with water. Hydrogen bonding analysis revealed that the amount of hydrogen bonding where water acts as a hydrogen donor while the anions act as hydrogen acceptors decreases as $[PhO]^- > [3Triaz]^- > [2CNpyr]^-$. The charge on the phenolate oxygen is more negative than the charges on any of the other anion atoms. This concentrated charge allows phenolate to form the most stable hydrogen bonds with water. Radial distribution function (RDF) analysis shows that as a result, water will tend to coordinate closer to the $[PhO]^-$ anions than any of the other anions. Likewise, water will cluster the least in the $[PhO]^-$ system and the most in the $[2CNpyr]^-$ system. The ability of the anion to stabilize water through hydrogen bonding interactions determines how water will interact in a given IL. If the anions can stabilize water via hydrogen bonding, water may form associated clusters with the anions. If the anions have less ability to form stable hydrogen bonds with water, then water will have a higher tendency to self aggregate.

The hydrogen bonding behavior between water and the anions also explains the IL affinity for water. Henry's law constants for water in each IL were determined by calculating the infinite dilution free energy of solvation. The solvation free energies were lowest for $[PhO]^-$ and highest for $[2CNpyr]^-$, following the same trend as the

number of hydrogen bonds formed where water acts as a hydrogen donor while the anions act as hydrogen acceptors. Furthermore, decomposition of the infinite dilution solvation free energy into Coulombic and Lennard-Jones (LJ) contributions revealed that the the LJ contribution was nearly the same for all ILs, and that the Coulombic contribution is primarily accountable for the differences in water affinity between the ILs. Therefore, the primary conclusion of this work is that the hydrogen bonding interactions depend on the charge magnitude of the negative anion atoms. Anions with more negative atoms will form stronger interactions with water leading to increased hydrogen bonding. When anion-water hydrogen bonding interactions are sufficiently strong, the anions will form associated clusters with water, and the dynamics will not increase as much as they otherwise would. Therefore, IL-water interactions can be tuned through choice of anion to control hydrogen bonding interactions and thus the water solubility to give optimal performance in a given application.

In the second work of this dissertation, the liquid structure function was both measured using X-ray scattering experiments and calculated from molecular dynamics simulations for several AHA ILs. The ILs examined consisted of a combination of two different cations, triethyl-octyl-phosphonium and trihexyl-tetradecyl-phosphonium ($[P_{66614}]^+$), and two different anions, $[2CNpyr]^-$ and 1,2,4-triazolide ($[4Triaz]^-$). Changes in the liquid structure function from both cation and anion substitution were investigated as well as changes in the liquid structure function from reaction with CO_2. The structure functions calculated from (MD) simulations were able to reproduce the experimental structure functions to a reasonable degree, and they were further partitioned to provide additional insights on the interactions responsible for the observed structure function features.

Both the simulations and experiments showed that for a given cation, the structure functions are very similar for different anions. Analysis of spatial distribution functions (SDFs) that show the high probability 3-dimensional orientations of dif-

ferent species were able to explain this observation. Regardless of the anion type, the anions will tend to occupy four high probability lobes between the short alkyl chains of the phosphonium cations. While SDFs for a central anion are different as determined by the charge distribution of the anion, the distribution of anions around cations is nearly the same. Therefore, the partitioning of the IL into polar and nonpolar domains as well as the alternation of charged species within the polar domain is relatively insensitive to the anions. The structure function does, however, change significantly from cation substitution. The cations are primarily responsible for the liquid ordering observed in the liquid structure function because they are much larger than the anions and they have both polar and nonpolar components that cause the formation of microheterogeneous polar and nonpolar domains within the IL. Many of the features in the liquid structure function become more pronounced when the $[P_{66614}]^+$ cation is substituted for $[P_{2228}]^+$ because the nonpolar cation components become sufficiently large for a continuous percolating nonpolar domain to form. When the nonpolar domain forms a continuous network, the alternation of polar and nonpolar domains becomes highly regular, giving rise to more pronounced features in the liquid structure function.

The reaction with CO_2 did not have a significant effect on the liquid structure function for any of the ILs studied. Similar to the case of the anion substitution, the main reason that the liquid structure function does not change much upon reaction with CO_2 is because the reacted anions occupy the same four high probability lobes between the short alkyl chains of the cations. The reaction with CO_2 does cause a change in the anion-anion partial structure functions because the anions grow in size by three heavy atoms. The fact that the liquid structure function does not change appreciably upon reaction with CO_2 helps to explain the fact that the viscosities of AHA ILs do not change much upon reaction with CO_2. When the ILs react with CO_2, the spatial orientations of the ions with respect to each other do not change

much, and therefore, the interionic interactions giving rise to the viscosity do not change much.

The IL structure functions investigated in this work demonstrated the same three primary features which have been seen before in other classes of ILs. There is a pre-peak corresponding to the long range ordering caused by the alternation of polar and nonpolar domains, a charge alternation feature due to the alternation of counterions within the polar domain, and an adjacency interaction peak due to a multitude of interactions between adjacent species. The structure functions presented in this work help to explain the viscosity behavior of AHA ILs upon reaction with CO_2 and also how the liquid organization changes from ion substitution.

In the third and final work of this dissertation, a method was created for calculating CO_2 absorption isotherms in AHA ILs. The method was developed and applied to $[P_{2228}][2CNpyr]$ to examine the CO_2 solubility dependence on the temperature and pressure. The reaction equilibrium between CO_2 and the IL was determined by calculating the Gibbs free energy of reaction. The method works by taking advantage of the fact that free energy is a state function, and therefore, a thermodynamic path can be taken to get the free energy of reaction instead of calculating the Gibbs free energy of reaction directly in the bulk IL. The thermodynamic cycle works by accounting for solution effects on the reaction free energy using classical MD simulations. This allows the free energy of the gas phase reaction, which must be calculated using *ab initio* methods, to be calculated for small systems consisting of an anion and CO_2 or a cation-anion pair and CO_2. Calculating the gas phase contribution to the total free energy of reaction allows higher level electronic structure calculations to be performed than could be done for a bulk liquid.

The expression for the free energy of reaction derived in this work depends on three thermodynamic properties that can be calculated without any fitting to empirical data, which allows the method to be used in a generally predictive way. The

model parameters that need to be calculated are the enthalpy of vaporization for the unreacted IL, the free energy of the gas phase reaction with CO_2, and the enthalpy of vaporization for the CO_2-reacted IL. The enthalpy of vaporization is readily calculated using MD to simulate the liquid and vapor phases. The results for the enthalpy of vaporization of the unreacted and CO_2-reacted ILs showed that the reacted IL always has a higher enthalpy of vaporization. The difference in the enthalpy of vaporization of the unreacted and CO_2-reacted ILs was on the order of 10 kJ mol^{-1}, which means that solution effects are non-negligible. Several researchers have calculated reaction enthalpies for simple gas phase reactions of the anions with CO_2 and attempted to compare these results to reaction enthalpies that are fit to experimental data. However, this work illustrates that there is no reason to expect that the two will be the same when solution effects are neglected in the calculation.

Another important finding in this work is that the free energy of vaporization for an ion pair can be estimated from the enthalpy of vaporization and and the translational entropy of an ideal gas molecule given by the Sackur-Tetrode equation. The vaporization free energy of an ion pair was calculated using rigorous MD free energy methods which numerically sample the entropy. The results for the free energy of vaporization using the mentioned simplifying assumption were in good agreement with the values obtained from the free energy method, differing by less than three kJ mol^{-1}. Therefore, the assumption can be used to calculate the free energy of vaporizing an ion pair using far fewer simulations than are required for the free energy method.

The free energy of the gas phase reaction was calculated using two different methods. The first way was to assume the cation does not play a role in the reaction, and to calculate the free energies of the anion, CO_2, and the CO_2-reacted anion. In the second method, *ab initio* molecular dynamics (AIMD) simulations of a single ion pair with a single CO_2 were used to compute the potential of mean force (PMF) to pull

the CO_2 off of the anion. The PMF calculations were run in an attempt to account for the cations effect on the free energy of the gas phase reaction, as it is known that ILs consisting of the same AHA paired with different cations will have different absorption capacities. The results for the free energy of the gas phase reaction showed that the *anion-only* model consistently gave reaction free energies that were lower than those calculated from the PMF. The free energy of the gas phase reaction was comparable in magnitude to the difference in the vaporization enthalpies of the reacted and unreacted anions, which further indicates that solution effects should not be ignored when calculating the reaction equilibrium between IL and CO_2. Previous studies have assumed solution effects are negligible and have attempted to calculate reaction equilibria based of of the gas phase reaction. We now know that this is an invalid approximation if quantitative results are sought.

Simulated mixtures of reacted an unreacted IL exhibit ideal solution behavior. Both the enthalpy of mixing and the excess volume are negligible over the complete composition range. Therefore, it was determined in this work that the thermodynamic properties of mixing reacted and unreacted IL can be approximated using ideal solution theory. The fact that reacted and unreacted ILs mix in an ideal fashion further helps to explain why the viscosity does not change much upon reaction with CO_2.

The derived expression for the free energy of reaction as a function of temperature, pressure, and composition was used to calculate CO_2 absorption isotherms. Points along the isotherm were determined by solving for the extent of reaction that minimizes the free energy of reaction at a given temperature and pressure. The resulting isotherms were able to do a reasonable job of predicting the absorption isotherms. At 300 K, the predicted isotherms did an excellent job of reproducing the experimental isotherms. As the temperature increased from 300 to 360 K, the agreement between the experimental and predicted isotherms decreased. We have concluded that it is

extremely challenging to quantitatively predict the reaction equilibria due to the fact that it depends exponentially on the free energy of reaction, and the free energy of reaction accumulates uncertainty from the calculation of each of the model parameters. A sensitivity analysis of the isotherm prediction at 300 K showed that the difference between a highly reactive IL and a nonreactive IL is only a different of about 16 kJ/mol in model parameters. This sensitivity does not come as a complete surprise as IL absorption capacities will change significantly from slight chemical alterations of the anions. The method does present a robust means to assess reactivity within a given family of ILs, even though quantitative prediction is quite difficult.

In this dissertation a combination of classical MD simulations, *ab initio* calculations, and AIMD simulations were used to investigate the behavior of several different AHA ILs. These simulations revealed that hydrogen bonding interactions between water and the anions determines how the properties of an IL will change when it is mixed with water. Anions can therefore be tuned to control the IL water affinity so that they perform well in the presence of water for a given application. The analysis used to investigate the IL-water mixtures can be applied to assess how other cosolvents might affect the IL behavior. Computed liquid structure functions were able to reproduce experimental structure functions and shed light on the liquid ordering. The liquid structure functions were mostly insensitive to the anions and whether or not they were reacted with CO_2. The different anions do not change the liquid structure function because they are relatively small in comparison to the cation, and they will tend to form the same interactions with the cation whether or not they are reacted with CO_2. The fact that the liquid structure function does not change much upon reaction with CO_2 helps explain the fact that the viscosities of AHA ILs are not significantly changed upon reaction with CO_2, because the interaction giving rise to the viscosity do not change. A method was created to predict CO_2 absorption isotherms by calculating the free energy of reaction using a thermodynamic

cycle. The method is capable of predicting isotherms that agree well with experimental data. The predicted isotherms are extremely sensitive to calculated model parameters, and therefore accurate quantitative prediction is a challenging task due to the accumulation in uncertainty from each of the calculated model parameters. Effects of the solvation environment on the free energy of reaction that have been neglected in previous studies were shown to significantly effect the reaction energetics. The enthalpy of reaction and the free energy of reaction should not be compared to experimental results unless the effects of the solvation environment are properly accounted for. Therefore, future studies of the reaction of CO_2 with ILs could benefit from using higher levels of theory such as AIMD simulations, QM/MM hybrid simulations, or reactive Monte-Carlo simulations that explicitly account for the solvation environment. The methods used in this dissertation present a means to compare different ILs within the same family, and to select ILs with the best estimated properties prior to synthesis and experiment. Simulations will continue to play a an important role in both designing and understanding CO_2-reactive ILs.

APPENDIX A

ION STRUCTURES AND FORCE FIELD PARAMETERS

A.1 $[P_{2228}]^+$ Force Field Parameters

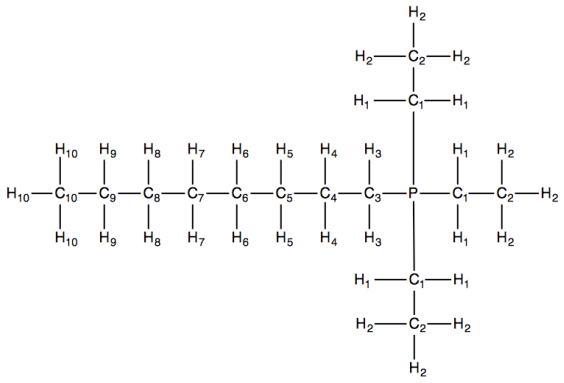

Figure A.1. $[P_{2228}]^+$ atom labels.

TABLE A.1

$[P_{2228}]^+$ ATOM TYPES, PARTIAL CHARGES, AND LENNARD-JONES PARAMETERS

Atom	Atom Type	Atom Charge	σ (nm)	ϵ (kJ mol^{-1})
P	p5	0.11897	3.74E-01	8.37E-01
C1	c3	0.0136	3.40E-01	4.58E-01
C2	c3	-0.18742	3.40E-01	4.58E-01
H1	hc	0.0539	2.65E-01	6.57E-02
H2	hc	0.07926	2.65E-01	6.57E-02
C3	c3	-0.13088	3.40E-01	4.58E-01
C4	c3	0.00301	3.40E-01	4.58E-01
H3	hc	0.08212	2.65E-01	6.57E-02
C5	c3	-0.05101	3.40E-01	4.58E-01
H4	hc	0.03558	2.65E-01	6.57E-02
H5	hc	0.02279	2.65E-01	6.57E-02
C6	c3	0.06886	3.40E-01	4.58E-01
C7	c3	0.04349	3.40E-01	4.58E-01
H6	hc	-0.01804	2.65E-01	6.57E-02
C8	c3	-0.03117	3.40E-01	4.58E-01
H7	hc	-0.01728	2.65E-01	6.57E-02
H8	hc	0.00151	2.65E-01	6.57E-02
C9	c3	0.15691	3.40E-01	4.58E-01
C10	c3	-0.22012	3.40E-01	4.58E-01
H9	hc	-0.02327	2.65E-01	6.57E-02
H10	hc	0.05328	2.65E-01	6.57E-02

TABLE A.2

$[P_{2228}]^+$ BOND TYPES

Bond Type	r_0 (nm)	K_r (kJ mol^{-1} nm^{-2})
c3-c3	1.09E-01	2.82E+05
p5-p5	1.81E-01	2.17E+05
c3-c3	1.54E-01	2.54E+05

TABLE A.3

$[P_{2228}]^+$ ANGLE TYPES

Angle Type	θ_0 (deg)	K_θ (kJ mol^{-1} rad^{-2})
p5-c3-hc	1.10E+02	3.56E+02
c3-c3-hc	1.10E+02	3.88E+02
hc-c3-hc	1.08E+02	3.30E+02
p5-c3-c3	1.12E+02	5.14E+02
c3-p5-c3	1.06E+02	4.94E+02
c3-c3-c3	1.11E+02	5.29E+02

TABLE A.4

$[P_{2228}]^+$ RB DIHEDRAL TYPES

Dihedral Type	C0	C1	C2	C3	C4	C5
p5-c3-c3-hc	0.6527	1.95811	0	-2.61082	0	0
c3-p5-c3-hc	0.09205	0.27614	0	-0.36819	0	0
hc-c3-c3-hc	0.6276	1.8828	0	-2.5104	0	0
c3-c3-c3-hc	0.66944	2.00832	0	-2.67776	0	0
hc-c3-c3-c3	0.66944	2.00832	0	-2.67776	0	0
p5-c3-c3-c3	0.6527	1.95811	0	-2.61082	0	0
c3-p5-c3-c3	0.09205	0.27614	0	-0.36819	0	0
c3-c3-c3-c3	3.68192	3.09616	-2.092	-3.01248	0	0

Dihedral coefficients are in units of kJ mol^{-1}.

A.2 $[P_{66614}]^+$ Force Field Parameters

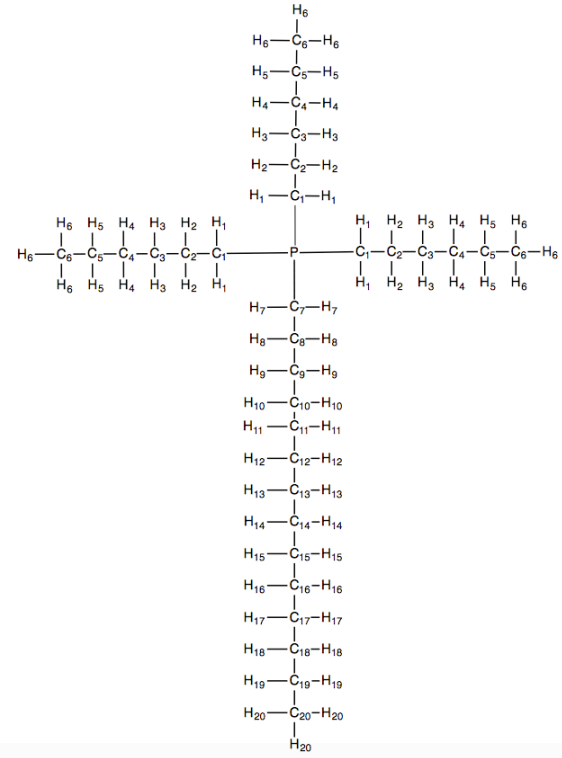

Figure A.2. $[P_{66614}]^+$ atom labels.

TABLE A.5:

$[P_{66614}]^+$ ATOM TYPES, PARTIAL CHARGES, AND LENNARD-JONES PARAMETERS

Atom	Atom Type	Atom Charge	σ (nm)	ϵ (kJ mol^{-1})
P1	p5	0.10573	3.74E-01	8.37E-01
C1	c3	-0.08263	3.40E-01	4.58E-01
H1	hc	0.06444	2.65E-01	6.57E-02

TABLE A.5: *Continued*

Atom	Atom Type	Atom Charge	σ (nm)	ϵ (kJ mol^{-1})
C2	c3	0.02808	3.40E-01	4.58E-01
H2	hc	0.03346	2.65E-01	6.57E-02
C3	c3	-0.0852	3.40E-01	4.58E-01
H3	hc	0.03248	2.65E-01	6.57E-02
C4	c3	-0.03781	3.40E-01	4.58E-01
H4	hc	0.01331	2.65E-01	6.57E-02
C5	c3	0.13064	3.40E-01	4.58E-01
H5	hc	-0.01337	2.65E-01	6.57E-02
C6	c3	-0.18006	3.40E-01	4.58E-01
H6	hc	0.04629	2.65E-01	6.57E-02
C7	c3	-0.05075	3.40E-01	4.58E-01
H7	hc	0.05424	2.65E-01	6.57E-02
C8	c3	-0.00971	3.40E-01	4.58E-01
H8	hc	0.04036	2.65E-01	6.57E-02
C9	c3	-0.05098	3.40E-01	4.58E-01
H9	hc	0.02761	2.65E-01	6.57E-02
C10	c3	-0.01226	3.40E-01	4.58E-01
H10	hc	0.00426	2.65E-01	6.57E-02
C11	c3	0.03756	3.40E-01	4.58E-01
H11	hc	-0.00537	2.65E-01	6.57E-02
C12	c3	0.00724	3.40E-01	4.58E-01
H12	hc	-0.00134	2.65E-01	6.57E-02
C13	c3	0.00769	3.40E-01	4.58E-01
H13	hc	-0.00355	2.65E-01	6.57E-02

TABLE A.5: *Continued*

Atom	Atom Type	Atom Charge	σ (nm)	ϵ (kJ mol^{-1})
C14	c3	0.01152	3.40E-01	4.58E-01
H14	hc	-0.00525	2.65E-01	6.57E-02
C15	c3	0.0164	3.40E-01	4.58E-01
H15	hc	-0.0055	2.65E-01	6.57E-02
C16	c3	0.02982	3.40E-01	4.58E-01
H16	hc	-0.00941	2.65E-01	6.57E-02
C17	c3	-0.00285	3.40E-01	4.58E-01
H17	hc	-0.0053	2.65E-01	6.57E-02
C18	c3	-0.00453	3.40E-01	4.58E-01
H18	hc	-0.00134	2.65E-01	6.57E-02
C19	c3	0.10945	3.40E-01	4.58E-01
H19	hc	-0.02009	2.65E-01	6.57E-02
C20	c3	-0.13306	3.40E-01	4.58E-01
H20	hc	0.0275	2.65E-01	6.57E-02

The bond, andgle, and dihedral types for $[P_{66614}]^+$ are the same as the $[P_{2228}]^+$ types.

A.3 $[2CNpyr]^-$ Force Field Parameters

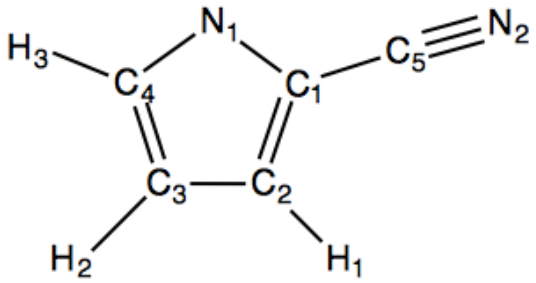

Figure A.3. $[2CNpyr]^-$ atom lables.

TABLE A.6

[2CNpyr]$^-$ ATOM TYPES, PARTIAL CHARGES, AND LENNARD-JONES PARAMETERS

Atom	Atom Type	Atom Charge	σ (nm)	ϵ (kJ mol^{-1})
C1	cd	0.23755	3.40E-01	3.60E-01
C2	cd	-0.29038	3.40E-01	3.60E-01
H1	ha	0.0985	2.60E-01	6.28E-02
C3	cc	-0.25231	3.40E-01	3.60E-01
H2	ha	0.07899	2.60E-01	6.28E-02
C4	cc	0.06303	3.40E-01	3.60E-01
H3	h4	0.03045	2.51E-01	6.28E-02
N1	nc	-0.5061	3.25E-01	7.11E-01
C5	ch	0.23445	3.40E-01	8.79E-01
N2	n1	-0.49418	3.25E-01	7.11E-01

TABLE A.7

[2CNpyr]$^-$ BOND TYPES

Bond Type	r_0 (nm)	K_r (kJ mol^{-1} nm^{-2})
cc-cc	1.08E-01	2.93E+05
cc-cc	1.09E-01	2.91E+05
cc-cc	1.43E-01	3.50E+05
cc-cc	1.38E-01	3.61E+05
cc-cc	1.37E-01	4.22E+05
cd-cd	1.43E-01	3.50E+05
ch-ch	1.14E-01	8.32E+05
ch-ch	1.43E-01	3.52E+05
nc-nc	1.34E-01	4.14E+05

TABLE A.8

$[2CNpyr]^-$ ANGLE TYPES

Angle Type	θ_0 (deg)	K_θ (kJ mol^{-1} rad^{-2})
cc-cc-ha	1.19E+02	3.97E+02
h4-cc-cc	1.29E+02	3.81E+02
h4-cc-nc	1.20E+02	4.18E+02
cc-cd-ha	1.23E+02	4.05E+02
ha-cc-cd	1.23E+02	4.05E+02
ha-cd-cd	1.22E+02	3.93E+02
cc-cc-cd	1.14E+02	5.70E+02
cc-nc-cd	1.07E+02	5.90E+02
cc-cc-nc	1.13E+02	5.85E+02
cc-cd-cd	1.14E+02	5.70E+02
cd-cd-ch	1.27E+02	5.30E+02
cd-cd-nc	1.13E+02	5.95E+02
ch-cd-nc	1.15E+02	6.28E+02
n1-ch-cd	1.79E+02	4.97E+02

TABLE A.9

[2CNpyr]$^-$ PERIODIC DIHEDRAL TYPES

Dihedral Types	$\phi_0(deg)$	K_ϕ (kJ mol^{-1})	n
cc-cc-cd-ha	180	16.735	2
h4-cc-cc-ha	180	16.735	2
h4-cc-cc-cd	180	16.735	2
h4-cc-nc-cd	180	19.873	2
nc-cc-cc-ha	180	16.735	2
ha-cc-cd-ha	180	16.735	2
ha-cc-cd-cd	180	16.735	2
ha-cd-cd-ch	180	16.735	2
ha-cd-cd-nc	180	16.735	2
cc-cc-cd-cd	180	16.735	2
cc-nc-cd-cd	180	19.873	2
cc-nc-cd-ch	180	19.873	2
cc-cc-nc-cd	180	19.873	2
cc-cd-cd-ch	180	16.735	2
cc-cd-cd-nc	180	16.735	2
nc-cc-cc-cd	180	16.735	2
cd-cd-ch-n1	180	0	2
n1-ch-cd-nc	180	0	2
cd-ch-cd-nc	180	4.602	2
cc-cd-cd-ha	180	4.602	2
cc-cd-cc-ha	180	4.602	2
nc-cc-h4-cc	180	4.602	2

A.4 $[2CNpyr:CO_2]^-$ Force Field Parameters

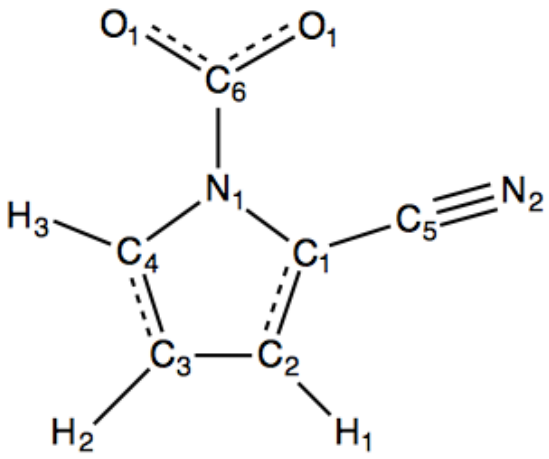

Figure A.4. $[2CNpyr:CO_2]^-$ atom lables.

TABLE A.10

$[2CNpyr:CO_2]^-$ ATOM TYPES, PARTIAL CHARGES, AND LENNARD-JONES PARAMETERS

Atom	Atom Type	Atom Charge	σ (nm)	ϵ (kJ mol^{-1})
N1	n	0.209	3.25E-01	7.11E-01
C1	cc	-0.168	3.40E-01	3.60E-01
C2	cd	-0.243	3.40E-01	3.60E-01
C3	cd	-0.086	3.40E-01	3.60E-01
C4	cc	-0.258	3.40E-01	3.60E-01
C5	cg	0.43	3.40E-01	8.79E-01
N2	n1	-0.483	3.25E-01	7.11E-01
H1	ha	0.124	2.60E-01	6.28E-02
H2	ha	0.079	2.60E-01	6.28E-02
H3	h4	0.133	2.51E-01	6.28E-02
C6	c	0.503	3.40E-01	3.60E-01
O1	o	-0.52	2.96E-01	8.79E-01

TABLE A.11

$[2CNpyr:CO_2]^-$ BOND TYPES

Bond Type	r_0 (nm)	K_r (kJ mol^{-1} nm^{-2})
cd-cd	0.10863461	2.91E+05
cc-cc	0.10834512	2.93E+05
n-n	0.13829185	3.56E+05
n-n	0.15555301	1.18E+05
cc-cc	0.13993598	4.22E+05
cc-cc	0.14210459	3.52E+05
cd-cd	0.14167007	3.50E+05
cg-cg	0.11670137	8.32E+05
c-c	0.12328292	5.42E+05

TABLE A.12

$[2CNpyr:CO_2]^-$ ANGLE TYPES

Angle Type	θ_0 (deg)	K_θ (kJ mol^{-1} rad^{-2})
n-cc-h4	118.718416	4.22E+02
cc-cd-ha	124.93837	4.05E+02
cd-cd-ha	127.067685	3.94E+02
cd-cd-ha	128.08768	3.94E+02
cd-cc-h4	131.708677	3.95E+02
cc-cd-ha	126.24297	4.05E+02
n-cc-cd	108.354476	5.92E+02
n-cc-cg	126.343236	6.00E+02
n-cc-cd	109.572905	5.92E+02
n-c-o	112.47133	6.35E+02
n-c-o	111.972127	6.35E+02
cc-n-cc	108.409324	5.76E+02
cc-n-c	127.86233	5.46E+02
cc-cd-cd	106.973948	5.70E+02
cc-cg-n1	170.874849	4.97E+02
cd-cc-cg	125.302287	5.43E+02
cd-cd-cc	106.689344	5.70E+02
cc-n-c	123.728344	5.46E+02
o-c-o	135.556542	9.13E+02

TABLE A.13

$2CNpyr{:}CO_2]^-$ RB DIHEDRAL TYPES

Dihedral Type	C0	C1	C2	C3	C4	C5
n-cc-cd-ha	33.472	0	-33.472	0	0	0
cc-n-cc-h4	13.8072	0	-13.8072	0	0	0
cc-cd-cd-ha	33.472	0	-33.472	0	0	0
cd-cd-cc-h4	33.472	0	-33.472	0	0	0
cg-cc-cd-ha	33.472	0	-33.472	0	0	0
ha-cd-cd-ha	33.472	0	-33.472	0	0	0
ha-cd-cc-h4	33.472	0	-33.472	0	0	0
c-n-cc-h4	13.8072	0	-13.8072	0	0	0
cc-cd-cd-ha	9.2048	0	-9.2048	0	0	0
n-cc-h4-cd	9.2048	0	-9.2048	0	0	0
n-cc-cd-cd	33.472	0	-33.472	0	0	0
n-cc-cg-n1	0	0	0	0	0	0
cc-n-cc-cd	13.8072	0	-13.8072	0	0	0
cc-cd-cd-cc	33.472	0	-33.472	0	0	0
c-n-cc-cd	13.8072	0	-13.8072	0	0	0
cd-cc-cg-n1	0	0	0	0	0	0
cd-cd-cc-cg	33.472	0	-33.472	0	0	0
cc-n-cc-cg	13.8072	0	-13.8072	0	0	0
c-n-cc-cg	13.8072	0	-13.8072	0	0	0
cc-n-cc-c	9.2048	0	-9.2048	0	0	0
n-cc-cg-cd	9.2048	0	-9.2048	0	0	0
n-o-c-o	9.2048	0	-9.2048	0	0	0

Dihedral coefficients are in units of kJ mol^{-1}.

TABLE A.14

$[2CNpyr:CO_2]^-$ HAND FIT CO_2 PERIODIC DIHEDRAL TYPES

Dihedral Type	$\phi_0(deg)$	K_ϕ (kJ mol^{-1})	n
cc-n-c-o	180	6.142	2

A.5 $[4Triaz]^-$ Force Field Parameters

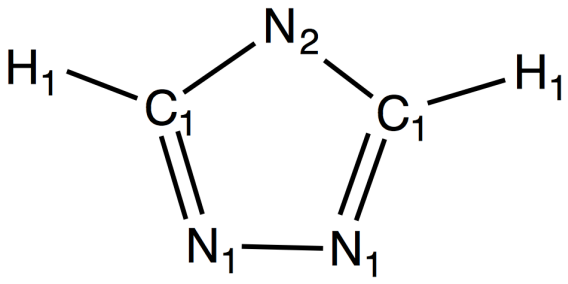

Figure A.5. $[4Triaz]^-$ atom labels.

TABLE A.15

[4Triaz]$^-$ ATOM TYPES, PARTIAL CHARGES, AND LENNARD-JONES PARAMETERS

Atom	Atom Type	Atom Charge	σ (nm)	ϵ (kJ mol^{-1})
N1	nd	-0.46596	3.25E-01	7.11E-01
C1	cc	0.52657	3.40E-01	3.60E-01
N2	nd	-0.7457	3.25E-01	7.11E-01
H1	h5	-0.08776	2.42E-01	6.28E-02

TABLE A.16

[4Triaz]$^-$ BOND TYPES

Bond Type	r_0 (nm)	K$_r$ (kJ mol^{-1} nm^{-2})
cc-cc	1.08E-01	2.98E+05
nd-nd	1.38E-01	4.07E+05
nd-nd	1.34E-01	4.14E+05

TABLE A.17

[4Triaz]$^-$ ANGLE TYPES

Angle Type	θ_0 (deg)	K_θ (kJ mol^{-1} rad^{-2})
nd-cc-h5	1.25E+02	4.19E+02
nd-nd-cc	1.08E+02	6.02E+02
nd-cc-nd	1.28E+02	5.93E+02
cc-nd-cc	1.16E+02	5.77E+02

TABLE A.18

[4Triaz]$^-$ RB DIHEDRAL TYPES

Dihedral Type	C0	C1	C2	C3	C4	C5
nd-nd-cc-h5	39.748	0	-39.748	0	0	0
cc-nd-cc-h5	39.748	0	-39.748	0	0	0
h5-nd-cc-nd	9.2048	0	-9.2048	0	0	0
nd-nd-cc-nd	39.748	0	-39.748	0	0	0
nd-cc-nd-cc	39.748	0	-39.748	0	0	0
cc-nd-nd-cc	33.472	0	-33.472	0	0	0

Dihedral coefficients are in units of kJ mol^{-1}.

A.6 $[4\text{Triaz:}CO_2(N_1)]^-$ Force Field Parameters

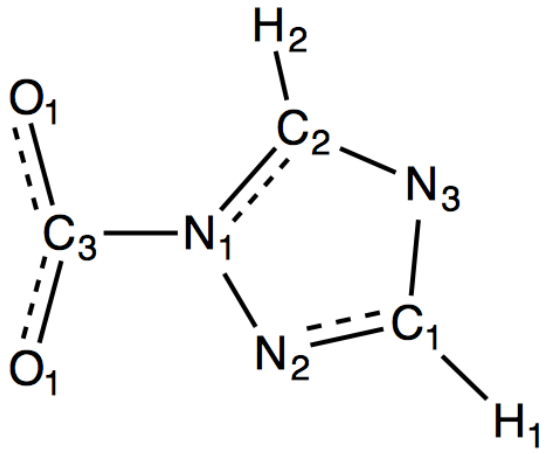

Figure A.6. $[4\text{Triaz:}CO_2(N_1)]^-$ atom lables.

TABLE A.19

$[4\text{Triaz:}CO_2(N_1)]^-$ ATOM TYPES, PARTIAL CHARGES, AND LENNARD-JONES PARAMETERS

Atom	Atom Type	Atom Charge	σ (nm)	ϵ (kJ mol^{-1})
N1	n	0.192	3.25E-01	7.11E-01
N2	nc	-0.55872	3.25E-01	7.11E-01
C1	cd	0.15925	3.40E-01	3.60E-01
N3	nd	-0.46652	3.25E-01	7.11E-01
C2	cc	0.35259	3.40E-01	3.60E-01
H1	h5	0.01133	2.42E-01	6.28E-02
H2	h5	0.04976	2.42E-01	6.28E-02
C3	c	0.55805	3.40E-01	3.60E-01
O1	o	-0.54887	2.96E-01	8.79E-01

TABLE A.20

$[4\text{Triaz:}CO_2(N_1)]^-$ BOND TYPES

Bond Type	r_0 (nm)	K_r (kJ mol^{-1} nm^{-2})
cd-cd	1.09E-01	2.98E+05
n-n	1.36E-01	4.39E+05
n-n	1.36E-01	3.56E+05
n-n	1.58E-01	1.05E+05
nc-nc	1.35E-01	4.14E+05
cd-cd	1.37E-01	3.61E+05
nd-nd	1.35E-01	4.14E+05
c-c	1.24E-01	5.42E+05

TABLE A.21

$[4\text{Triaz:}CO_2(N_1)]^-$ ANGLE TYPES

Angle Type	θ_0 (deg)	K_θ (kJ mol^{-1} rad^{-2})
n-cc-h5	1.22E+02	4.26E+02
nc-cd-h5	1.21E+02	4.19E+02
nd-cd-h5	1.23E+02	4.12E+02
nd-cc-h5	1.27E+02	4.19E+02
n-nc-cd	1.02E+02	5.81E+02
n-cc-nd	1.11E+02	5.96E+02
n-c-o	1.13E+02	6.35E+02
n-c-o	1.10E+02	6.35E+02
nc-n-cc	1.10E+02	5.87E+02
nc-n-c	1.25E+02	5.62E+02
nc-cd-nd	1.15E+02	6.14E+02
cd-nd-cc	1.01E+02	5.95E+02
cc-n-c	1.25E+02	5.46E+02
o-c-o	1.37E+02	1.02E+03

TABLE A.22

4Triaz:$CO_2(N_1)]^-$ RB DIHEDRAL TYPES

Dihedral Type	C0	C1	C2	C3	C4	C5
n-nc-cd-h5	39.748	0	-39.748	0	0	0
nc-n-cc-h5	13.8072	0	-13.8072	0	0	0
cd-nd-cc-h5	39.748	0	-39.748	0	0	0
cc-nd-cd-h5	39.748	0	-39.748	0	0	0
c-n-cc-h5	13.8072	0	-13.8072	0	0	0
h5-nc-cd-nd	9.2048	0	-9.2048	0	0	0
h5-n-cc-nd	9.2048	0	-9.2048	0	0	0
n-nc-cd-nd	39.748	0	-39.748	0	0	0
n-cc-nd-cd	39.748	0	-39.748	0	0	0
nc-n-cc-nd	13.8072	0	-13.8072	0	0	0
nc-cd-nd-cc	39.748	0	-39.748	0	0	0
cc-n-nc-cd	40.1664	0	-40.1664	0	0	0
c-n-nc-cd	40.1664	0	-40.1664	0	0	0
c-n-cc-nd	13.8072	0	-13.8072	0	0	0
nc-n-cc-c	9.2048	0	-9.2048	0	0	0
n-o-c-o	9.2048	0	-9.2048	0	0	0

Dihedral coefficients are in units of kJ mol^{-1}.

TABLE A.23

[4Triaz:$CO_2(N_1)$]$^-$ HAND FIT CO_2 PERIODIC DIHEDRAL TYPES

Dihedral Type	$\phi_0(deg)$	K_ϕ (kJ mol^{-1})	n
nc-n-c-o	180	3.654	2
cc-n-c-o	180	3.654	2

A.7 [4Triaz:$CO_2(N_3)$]$^-$ Force Field Parameters

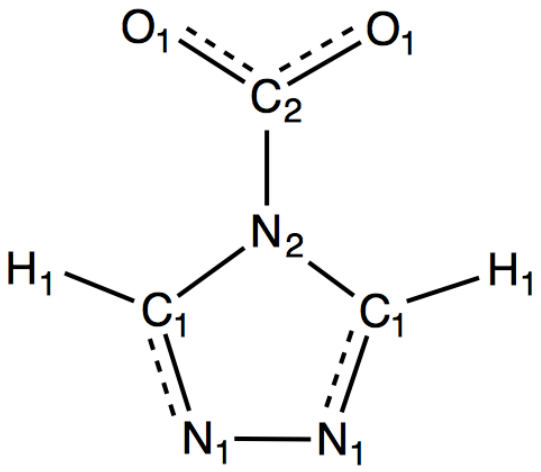

Figure A.7. [4Triaz:$CO_2(N_3)$]$^-$ atom labels.

TABLE A.24

$[4\text{Triaz:}CO_2(N_3)]^-$ ATOM TYPES, PARTIAL CHARGES, AND LENNARD-JONES PARAMETERS

Atom	Atom Type	Atom Charge	σ (nm)	ϵ (kJ mol^{-1})
N1	nc	-0.34734	3.25E-01	7.11E-01
C1	cd	0.1903	3.40E-01	3.60E-01
N2	n	0.00171	3.25E-01	7.11E-01
H1	h5	0.03503	2.42E-01	6.28E-02
C2	c	0.50545	3.40E-01	3.60E-01
O1	o	-0.53157	2.96E-01	8.79E-01

TABLE A.25

$[4\text{Triaz:}CO_2(N_3)]^-$ BOND TYPES

Bond Type	r_0 (nm)	K_r (kJ mol^{-1} nm^{-2})
cd-cd	1.09E-01	2.98E+05
nc-nc	1.39E-01	4.07E+05
nc-nc	1.34E-01	4.14E+05
cd-cd	1.36E-01	3.56E+05
n-n	1.56E-01	1.23E+05
c-c	1.24E-01	5.42E+05

TABLE A.26

$[4Triaz{:}CO_2(N_3)]^-$ ANGLE TYPES

Angle Type	θ_0 (deg)	K_θ (kJ mol^{-1} rad^{-2})
nc-cd-h5	122.52	4.19E+02
nc-cd-h5	126.18	4.19E+02
n-cd-h5	122.52	4.25E+02
n-cd-h5	126.18	4.25E+02
nc-nc-cd	106.51	6.06E+02
nc-cd-n	111.3	5.94E+02
cd-n-cd	104.38	5.76E+02
cd-n-c	127.81	5.46E+02
n-c-o	111.91	6.35E+02
o-c-o	136.18	1.02E+03

TABLE A.28

$[4Triaz{:}CO_2(N_3)]^-$ HAND FIT CO_2 PERIODIC DIHEDRAL TYPES

Dihedral Type	$\phi_0(deg)$	K_ϕ (kJ mol^{-1})	n
cd-n-c-o	180	4.6064	2

TABLE A.27

[4Triaz:$CO_2(N_3)$]$^-$ RB DIHEDRAL TYPES

Dihedral Type	C0	C1	C2	C3	C4	C5
nc-nc-cd-h5	39.748	0	-39.748	0	0	0
cd-n-cd-h5	13.8072	0	-13.8072	0	0	0
h5-cd-n-c	13.8072	0	-13.8072	0	0	0
h5-n-cd-nc	9.2048	0	-9.2048	0	0	0
nc-cd-n-h5	9.2048	0	-9.2048	0	0	0
nc-nc-cd-n	39.748	0	-39.748	0	0	0
nc-cd-n-cd	13.8072	0	-13.8072	0	0	0
nc-cd-n-c	13.8072	0	-13.8072	0	0	0
cd-nc-nc-cd	33.472	0	-33.472	0	0	0
c-cd-n-cd	9.2048	0	-9.2048	0	0	0
n-o-c-o	9.2048	0	-9.2048	0	0	0

Dihedral coefficients are in units of kJ mol^{-1}.

A.8 $[3Triaz]^-$ Force Field Parameters

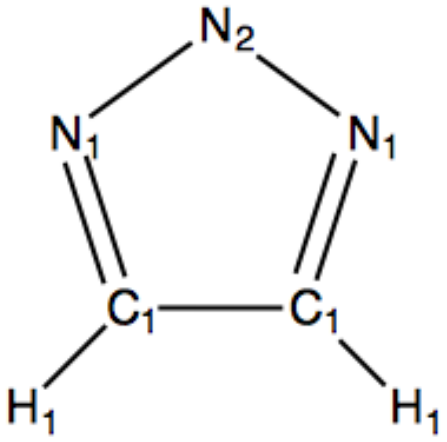

Figure A.8. $[3Triaz]^-$ atom types.

TABLE A.29

[3Triaz]$^-$ ATOM TYPES, PARTIAL CHARGES, AND LENNARD-JONES PARAMETERS

Atom	Atom Type	Atom Charge	σ (nm)	ϵ (kJ mol^{-1})
N1	nc	-0.3731	3.25E-01	7.11E-01
N2	nc	-0.18896	3.25E-01	7.11E-01
C1	cd	0.11998	3.40E-01	3.60E-01
H1	h4	-0.0524	2.51E-01	6.28E-02

TABLE A.30

[3Triaz]$^-$ BOND TYPES

Bond Type	r_0 (nm)	k (kJ mol^{-1} nm^{-2})
cd-cd	1.08E-01	2.93E+05
nc-nc	1.38E-01	4.07E+05
nc-nc	1.34E-01	4.14E+05
cd-cd	1.43E-01	3.50E+05

TABLE A.31

[3Triaz]$^-$ ANGLE TYPES

Angle Type	θ_0 (deg)	K_θ (kJ mol^{-1} rad^{-2})
nc-cd-h4	1.19E+02	4.30E+02
cd-cd-h4	1.29E+02	3.81E+02
nc-nc-nc	1.09E+02	6.54E+02
nc-cd-cd	1.13E+02	5.95E+02
nc-nc-cd	1.06E+02	6.06E+02

TABLE A.32

[3Triaz]$^-$ RB DIHEDRAL TYPES

Dihedral	C0	C1	C2	C3	C4	C5
nc-cd-cd-h4	33.472	0	-33.472	0	0	0
nc-nc-cd-h4	39.748	0	-39.748	0	0	0
h4-cd-cd-h4	33.472	0	-33.472	0	0	0
cd-h4-cd-nc	9.2048	0	-9.2048	0	0	0
nc-cd-h4-cd	9.2048	0	-9.2048	0	0	0
nc-nc-nc-cd	33.472	0	-33.472	0	0	0
nc-cd-cd-nc	33.472	0	-33.472	0	0	0
nc-nc-cd-cd	39.748	0	-39.748	0	0	0
cd-nc-nc-nc	33.472	0	-33.472	0	0	0

Dihedral coefficients are in units of kJ mol^{-1}.

A.9 $[PhO]^-$ Force Field Parameters

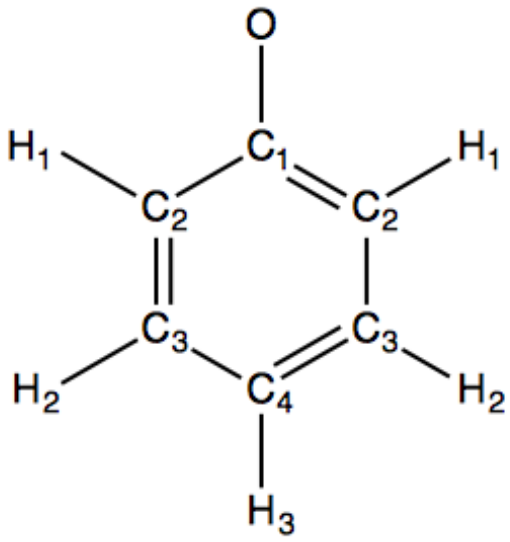

Figure A.9. $[PhO]^-$ atom types.

TABLE A.33

$[PhO]^-$ ATOM TYPES, PARTIAL CHARGES, AND LENNARD-JONES PARAMETERS

Atom	Atom Type	Atom Charge	σ (nm)	ϵ (kJ mol^{-1})
C4	ca	-0.339	3.40E-01	3.60E-01
C3	ca	-0.063	3.40E-01	3.60E-01
C2	ca	-0.34	3.40E-01	3.60E-01
C1	ca	0.5527	3.40E-01	3.60E-01
H3	ha	0.081	2.60E-01	6.28E-02
H2	ha	0.068	2.60E-01	6.28E-02
H1	ha	0.095	2.60E-01	6.28E-02
O	o	-0.8147	2.96E-01	8.79E-01

TABLE A.34

$[PhO]^-$ BOND TYPES

Bond Type	r_0 (nm)	k (kJ mol^{-1} nm^{-2})
ca-ca	1.09E-01	2.88E+05
ca-ca	1.39E-01	4.00E+05
ca-ca	1.23E-01	5.10E+05

TABLE A.35

$[PhO]^-$ ANGLE TYPES

Angle Type	θ_0 (deg)	K_θ (kJ mol^{-1} rad^{-2})
ca-ca-ha	1.20E+02	4.06E+02
ca-ca-ca	1.20E+02	5.62E+02
ca-ca-o	1.23E+02	6.01E+02

TABLE A.36

$[PhO]^-$ RB DIHEDRAL TYPES

Dihedral	C0	C1	C2	C3	C4	C5
ca-ca-ca-ha	30.334	0	-30.334	0	0	0
ha-ca-ca-ca	30.334	0	-30.334	0	0	0
ha-ca-ca-ha	30.334	0	-30.334	0	0	0
ha-ca-ca-o	30.334	0	-30.334	0	0	0
ha-ca-ca-ca	9.2048	0	-9.2048	0	0	0
ca-ca-ca-ha	9.2048	0	-9.2048	0	0	0
ca-ca-ca-ca	30.334	0	-30.334	0	0	0
ca-ca-ca-o	30.334	0	-30.334	0	0	0
ca-ca-ca-o	9.2048	0	-9.2048	0	0	0

Dihedral coefficients are in units of kJ mol^{-1}.

APPENDIX B

SUPPLEMENTAL PLOTS: ANION DEPENDENT DYNAMICS AND WATER SOLUBILITY EXPLAINED BY HYDROGEN BONDING INTERACTIONS IN MIXTURES OF WATER AND APROTIC HETEROCYCLIC ANION IONIC LIQUIDS

B.1 Dry Vs. Wet MSDs

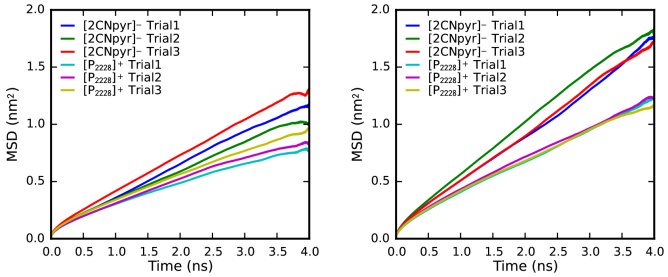

(a) Dry $[2CNpyr]^-$ **(b)** Wet $[2CNpyr]^-$

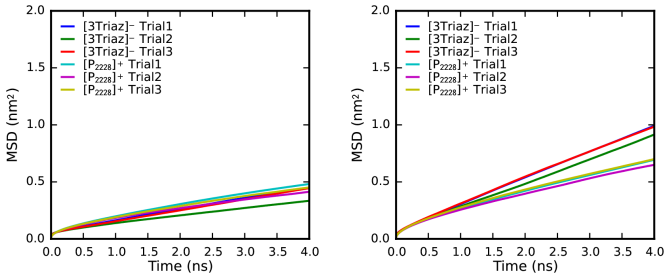

(c) Dry $[3Triaz]^-$ **(d)** Wet $[3Triaz]^-$

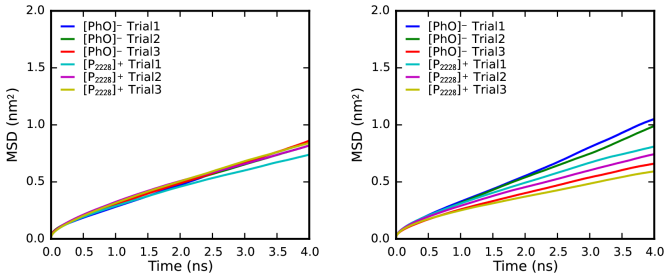

(e) Dry $[PhO]^-$ **(f)** Wet $[PhO]^-$

Figure B.1. MSDs for the dry systems shown on the left and the corresponding wet systems shown on the right.

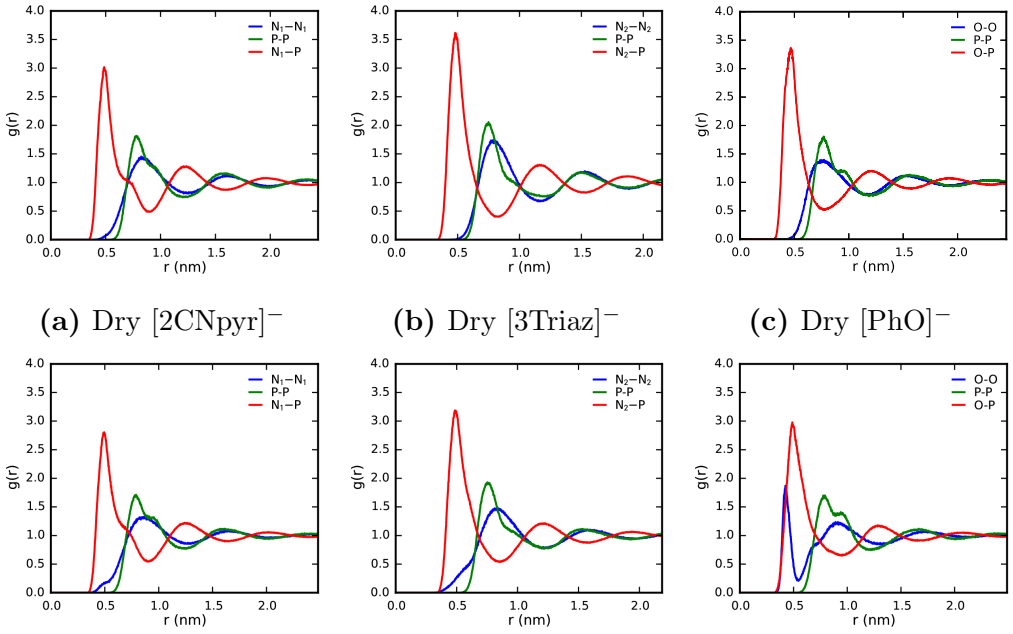

(a) Dry $[2CNpyr]^-$ **(b)** Dry $[3Triaz]^-$ **(c)** Dry $[PhO]^-$

(d) Wet $[2CNpyr]^-$ **(e)** Wet $[3Triaz]^-$ **(f)** Wet $[PhO]^-$

Figure B.2. RDFs of dry systems (top) and the corresponding wet systems (bottom). Heavy atoms are selected to represent each molecule: The phosphorus atom on the cation (P), the ring nitrogen on $[2CNpyr]^-$ (N_1), the unique nitrogen on $[3Triaz]^-$ (N_2), and the oxygen on $[PhO]^-$ (O).

B.3 Hydrogen Bonding Contour Plots

The following section shows correlated distribution functions (CDFs) between the hydrogen bonding distance and the hydrogen bonding angle for all of the wet ILs. All hydrogen bonding CDFs were calculated using TRAVIS [14] and rendered using Mathematica.

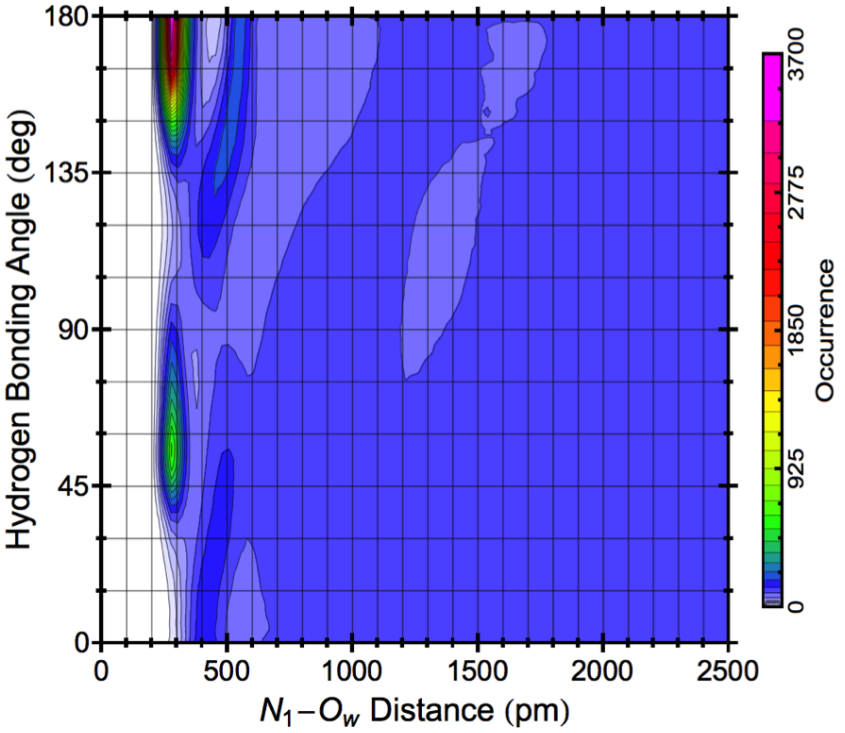

Figure B.3. Wet $[P_{2228}][2CNpyr]$ contour plot of correlated distribution function of N_1-O_W distance with the hydrogen bonding angle between N_1 and H_2O.

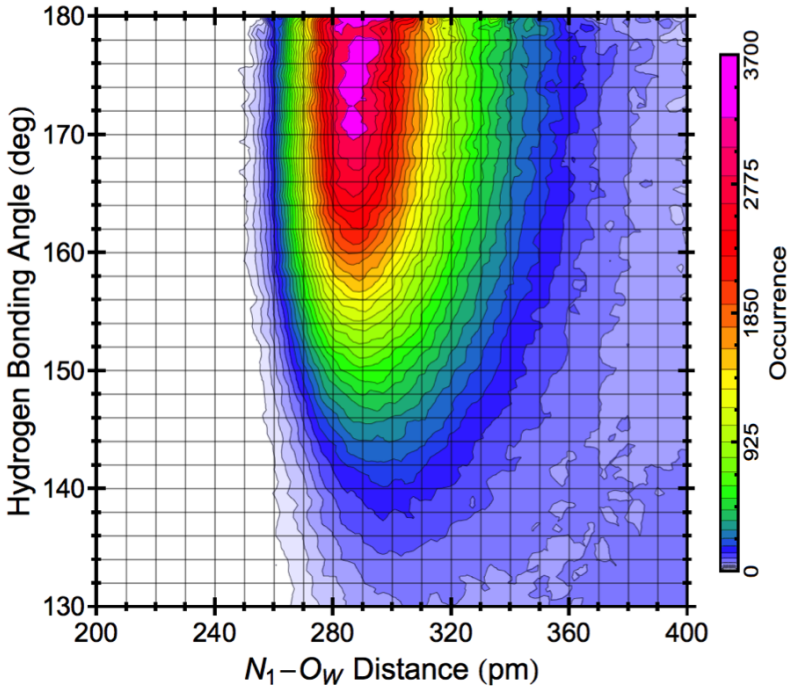

Figure B.4. Wet [P_{2228}][2CNpyr] contour plot for the correlated distribution function of N_1-O_W distance with the hydrogen bonding angle between N_1 and H_2O highlighting hydrogen bonding region.

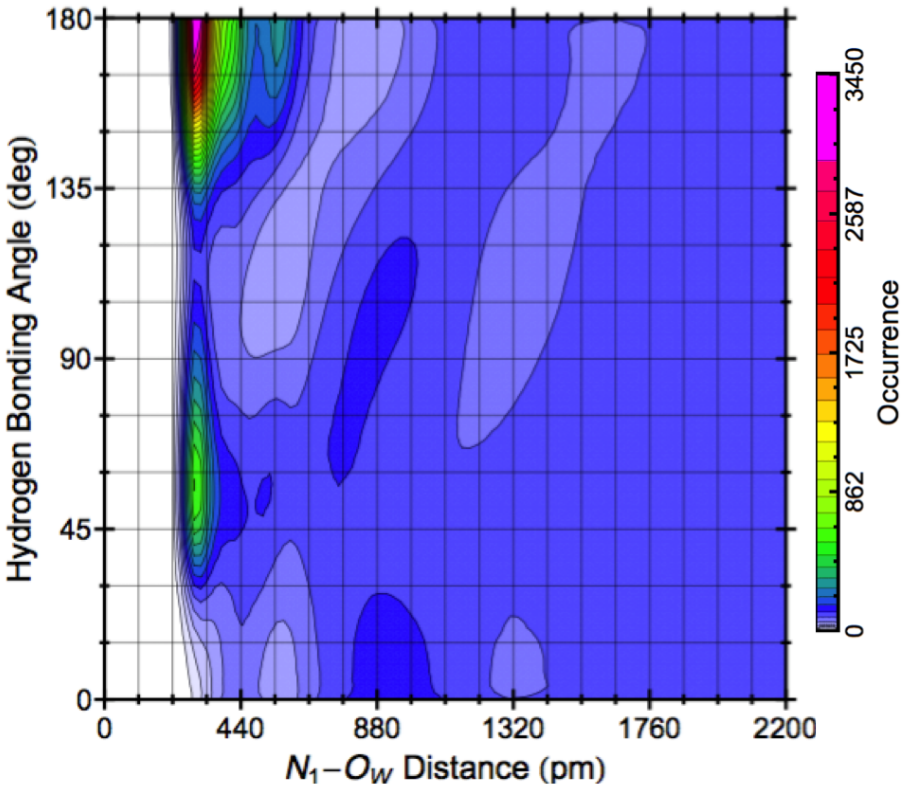

Figure B.5. Wet $[P_{2228}][3Triaz]$ contour plot of correlated distribution function of N_1-O_W distance with the hydrogen bonding angle between N_1 and H_2O.

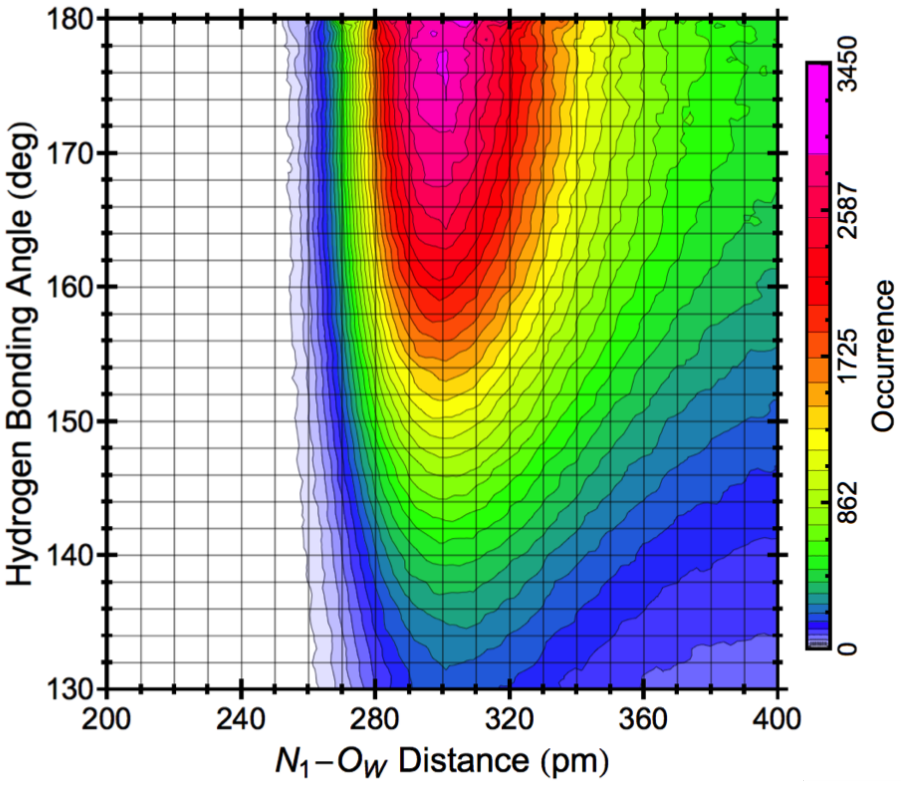

Figure B.6. Contour plot of correlated distribution function of N_1-O_W distance with the hydrogen bonding angle between N_1 and H_2O highlighting hydrogen bonding region in wet $[P_{2228}][3Triaz]$.

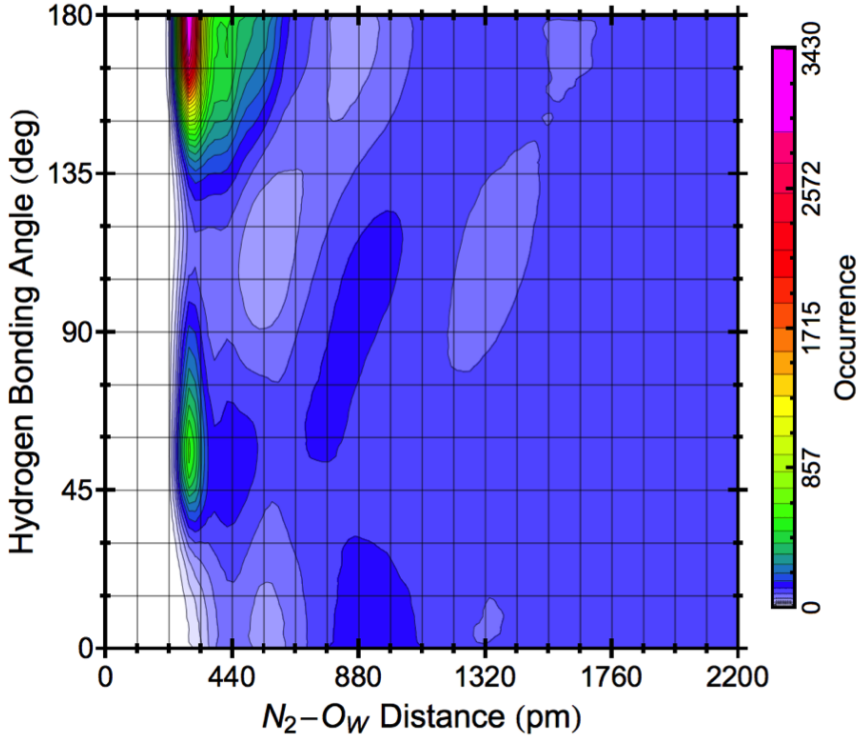

Figure B.7. Wet [P_{2228}][3Triaz] contour plot for the correlated distribution function of N_2-O_W distance with the hydrogen bonding angle between N_2 and H_2O.

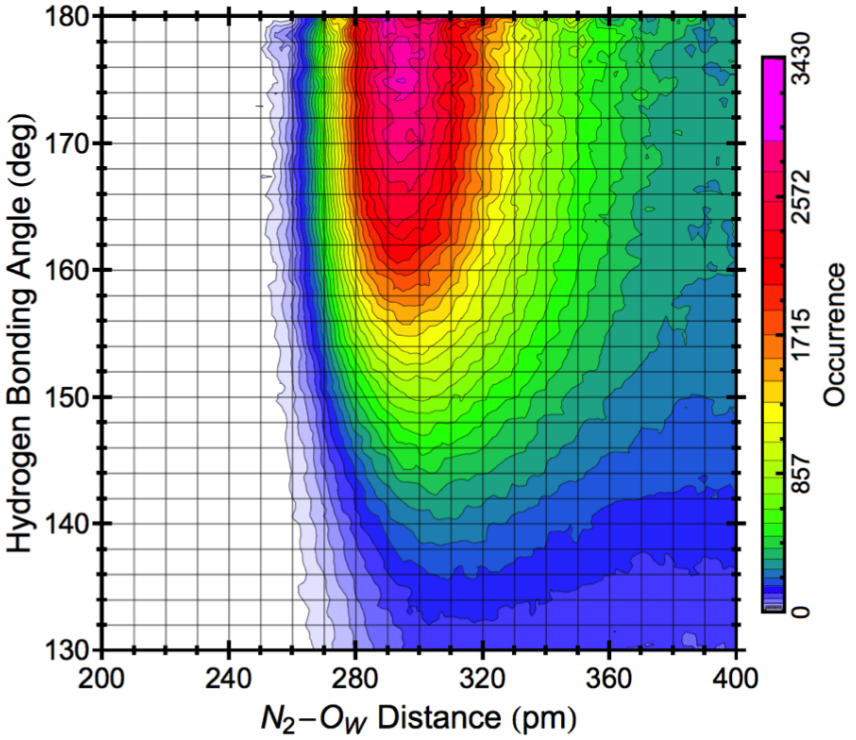

Figure B.8. Contour plot of correlated distribution function of N_2-O_W distance with the hydrogen bonding angle between N_2 and H_2O highlighting hydrogen bonding region in wet $[P_{2228}][3Triaz]$.

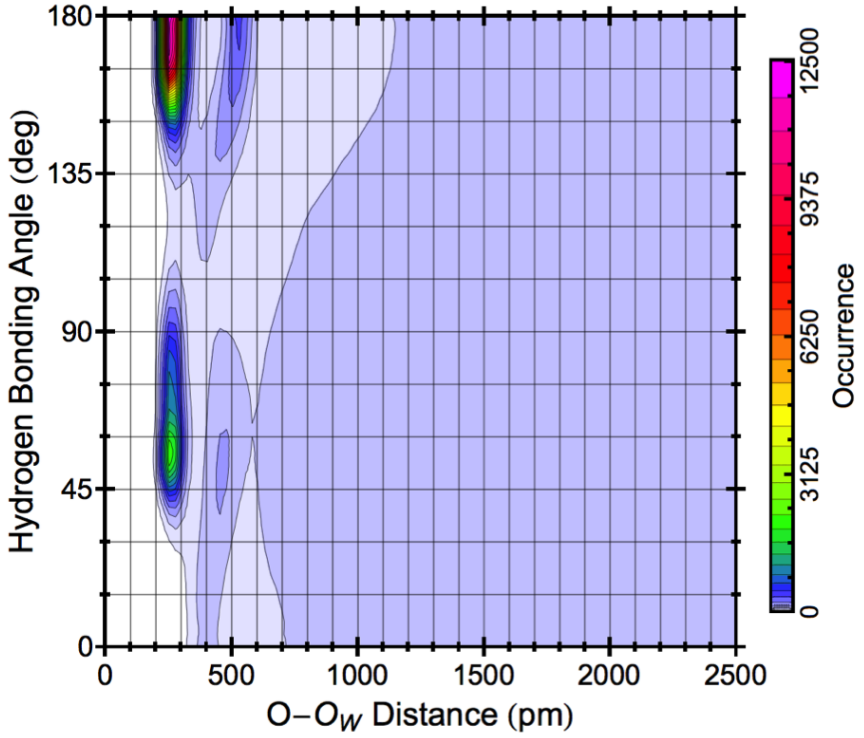

Figure B.9. Contour plot of correlated distribution function of O-O_W distance with the hydrogen bonding angle between O and H_2O in wet $[P_{2228}][PhO]$.

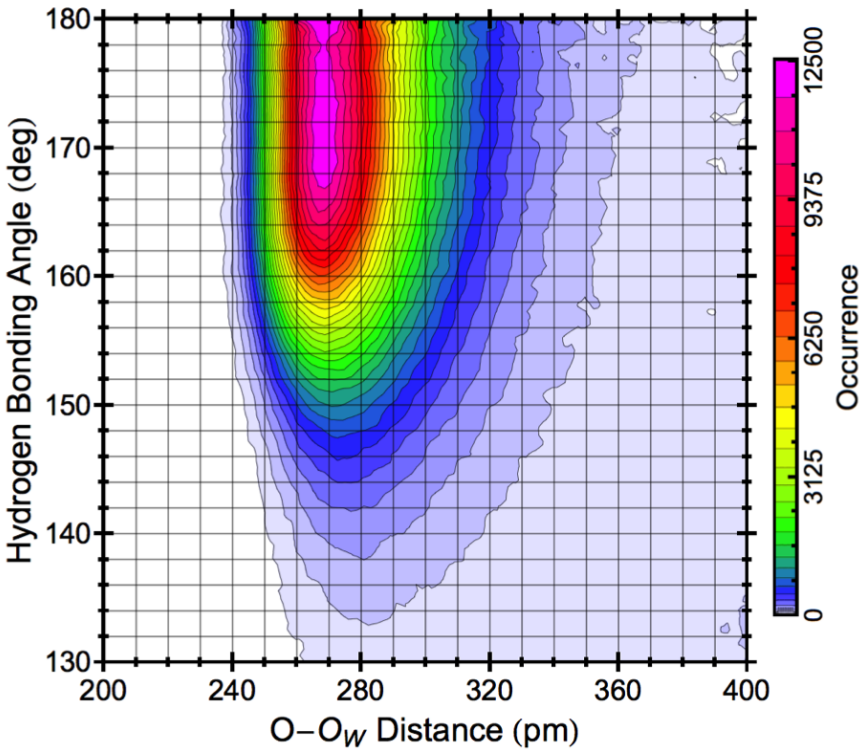

Figure B.10. Contour plot of correlated distribution function of O-O_W distance with the hydrogen bonding angle between O and H_2O highlighting hydrogen bonding region in wet $[P_{2228}][PhO]$.

APPENDIX C

SUPPLEMENTAL PLOTS: LIQUID STRUCTURE OF CO2-REACTIVE APROTIC HETEROCYCLIC ANION IONIC LIQUIDS FROM X-RAY SCATTERING AND MOLECULAR DYNAMICS

C.1 Supplementary Results

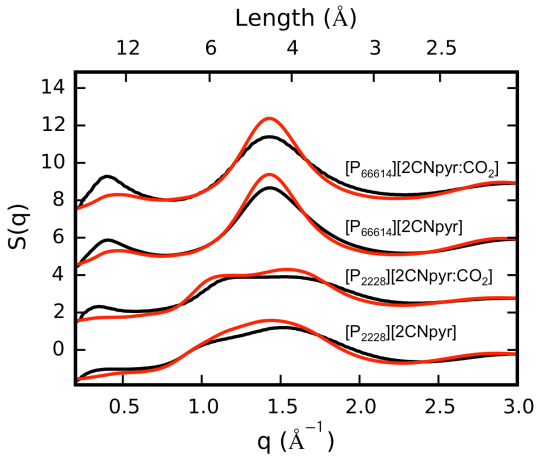

Figure C.1. Comparison of experimental (black) and simulated (red) total structure functions at small q values for $[2CNpyr]^-$ ILs. The primary abscissa (bottom) is in reciprocal space while the secondary abscissa (top) shows the corresponding real space distance.

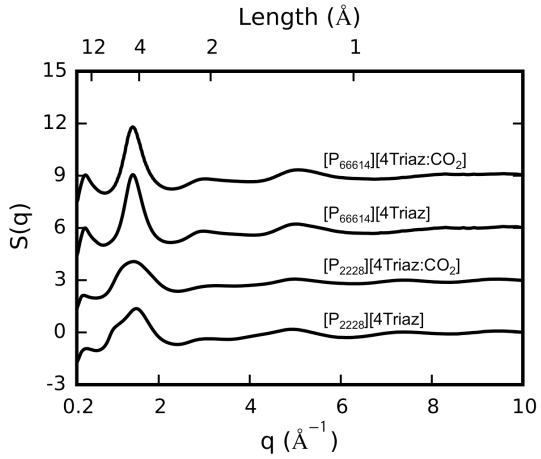

Figure C.2. Room temperature (295 K) experimental structure functions for $[4Triaz]^-$ ILs. The plots are offset by 0, 3, 6, and 9 for $[P_{2228}][4Triaz]$, $[P_{2228}][4Triaz:CO_2]$, $[P_{66614}][4Triaz]$, and $[P_{66614}][4Triaz:CO_2]$, respectively. The primary abscissa (bottom) is in reciprocal space while the secondary abscissa (top) shows the corresponding real space distance.

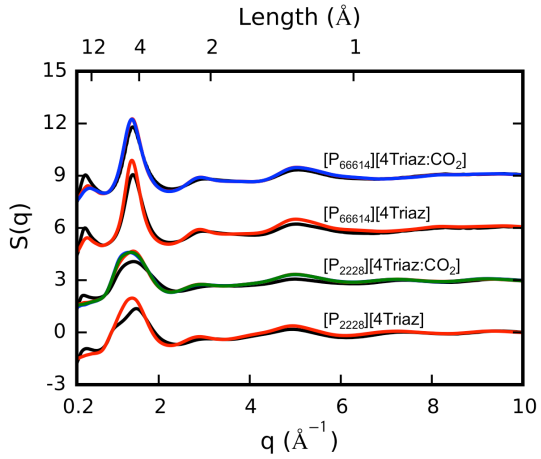

Figure C.3. Comparison of experimental (black) and simulated (colored) structure functions for $[4Triaz]^-$ ILs. The plots are offset by 0, 3, 6, and 9 for $[P_{2228}][4Triaz]$, $[P_{2228}][4Triaz{:}CO_2]$, $[P_{66614}][4Triaz]$, and $[P_{66614}][4Triaz{:}CO_2]$, respectively. Simulated structure functions are shown for $[4Triaz{:}CO_2(N_1)]^-$ (red), $[4Triaz{:}CO_2(N_1)]^-$ (blue), and a 50/50 mix of the two reaction sites (green). The mixture of reaction sites was not considered in the $[P_{66614}]^+$ ILs. The primary abscissa (bottom) is in reciprocal space while the secondary abscissa (top) shows the corresponding real space distance.

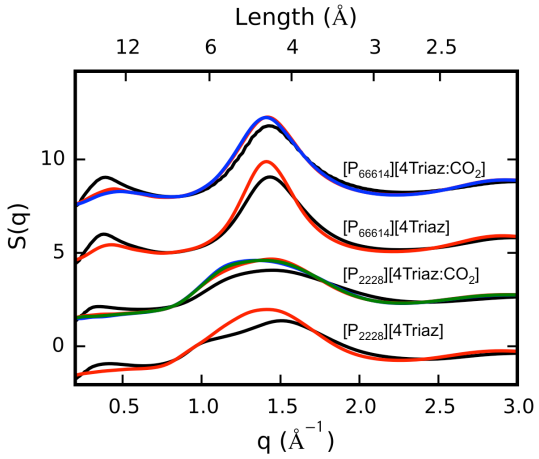

Figure C.4. Comparison of experimental (black) and simulated (colored) total structure functions at small q values for $[4\text{Triaz}]^-$ ILs. Simulated structure functions are shown for $[4\text{Triaz:CO}_2(\text{N}_1)]^-$ (red), $[4\text{Triaz:CO}_2(\text{N}_1)]^-$ (blue), and a 50/50 mix of the two reaction sites (green). The mixture of reaction sites was not considered in the $[\text{P}_{66614}]^+$ ILs. The primary abscissa (bottom) is in reciprocal space while the secondary abscissa (top) shows the corresponding real space distance.

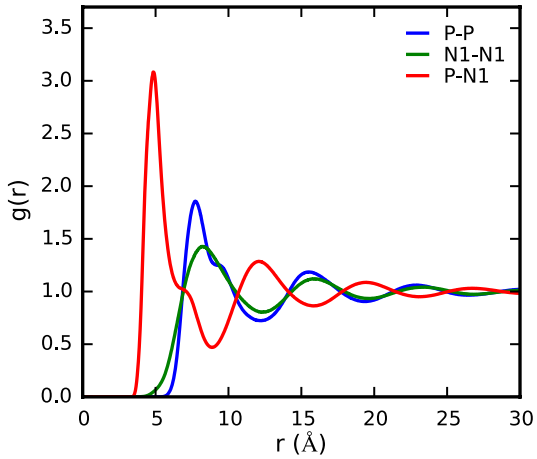

(a) $[P_{2228}][2CNpyr]$

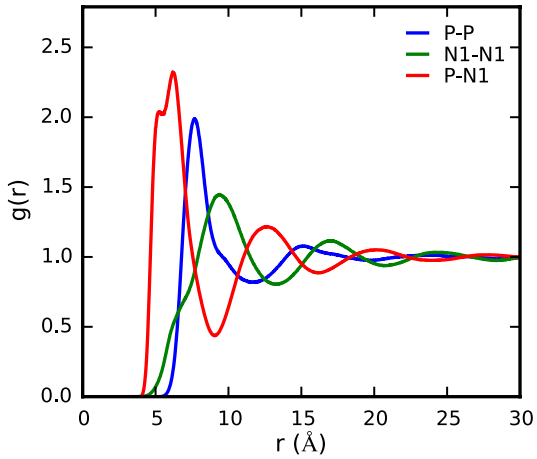

(b) $[P_{2228}][2CNpyr{:}CO_2]$

Figure C.5. Interionic RDFs for reacted and unreacted $[P_{2228}][2CNpyr]$.

APPENDIX D

SUPPLEMENTARY RESULTS: CALCULATING CO_2 SOLUBILITIES IN CO_2-REACTIVE APROTIC HETEROCYCLIC ANION IONIC LIQUIDS

D.1 Vaporization and Solvation Results

TABLE D.1

SUMMARY OF RESULTS FOR ENTHALPY OF VAPORIZATION CALCULATIONS

System	Temp (K)	H_g	±	H_l	±	ΔH_{vap}	±
$[P_{2228}][2CNpyr]$	300	392.7	0.2	230.1	0.1	165.1	0.2
$[P_{2228}][2CNpyr:CO_2]$	300	427.4	0.3	258.1	0.2	171.8	0.3
$[P_{2228}][2CNpyr]$	333	429.9	0.3	274.6	0.2	158.0	0.3
$[P_{2228}][2CNpyr:CO_2]$	333	467.9	0.3	304.9	0.2	165.8	0.4
$[P_{2228}][2CNpyr]$	360	460.3	0.1	310.4	0.0	152.9	0.1
$[P_{2228}][2CNpyr:CO_2]$	360	500.8	0.3	343.0	0.2	160.7	0.3

Uncertainties in liquid phase enthalpies (H_l) are based on block averaging of the production trajectories. Uncertainties in the vapor phase enthalpies (H_g) are based on the standard deviation of the average enthalpies of ten independent simulations.

TABLE D.2

SUMMARY OF RESULTS FOR INDIVIDUAL ION SOLVATION FREE ENERGIES

System	T (K)	Ion	ΔG^{Q}_{solv}	±	ΔG^{vdW}_{solv}	±	ΔG_{solv}	±
$[P_{2228}][2CNpyr]$	300	$[P_{2228}]^+$	-97.9	0.7	-31.1	0.5	-128.96	0.9
$[P_{2228}][2CNpyr]$	300	$[2CNpyr]^-$	-136.6	0.8	-19.3	0.3	-155.86	0.9
$[P_{2228}][2CNpyr:CO_2]$	300	$[P_{2228}]^+$	-103.2	0.8	-30.9	1.1	-134.06	1.3
$[P_{2228}][2CNpyr:CO_2]$	300	$[2CNpyr:CO_2]^-$	-127.5	1.1	-31.9	0.8	-159.36	1.4
$[P_{2228}][2CNpyr]$	333	$[P_{2228}]^+$	-98.1	0.7	-26.2	0.4	-124.29	0.8
$[P_{2228}][2CNpyr]$	333	$[2CNpyr]^-$	-134.3	0.7	-17.2	0.1	-151.52	0.7
$[P_{2228}][2CNpyr:CO_2]$	333	$[P_{2228}]^+$	-103.0	0.4	-27.5	0.5	-130.47	0.6
$[P_{2228}][2CNpyr:CO_2]$	333	$[2CNpyr:CO_2]^-$	-127.9	1.0	-28.1	0.4	-155.98	1.0
$[P_{2228}][2CNpyr]$	360	$[P_{2228}]^+$	-98.0	0.4	-23.0	0.5	-120.98	0.6
$[P_{2228}][2CNpyr]$	360	$[2CNpyr]^-$	-133.2	0.4	-15.6	0.2	-148.82	0.4
$[P_{2228}][2CNpyr:CO_2]$	360	$[P_{2228}]^+$	-101.4	0.4	-23.2	0.6	-124.65	0.7
$[P_{2228}][2CNpyr:CO_2]$	360	$[2CNpyr:CO_2]^-$	-125.5	0.5	-26.5	0.2	-152	0.5

ΔG^{Q}_{solv} and ΔG^{vdW}_{solv} are the Coulombic and van der Waals contributions to the free energy of solvation, respectively. Al values given are in kJ mol^{-1}. Uncertainties are based on block averaging using g_bar in Gromacs 4.5.5.

D.2 Additional Calculated Isotherms

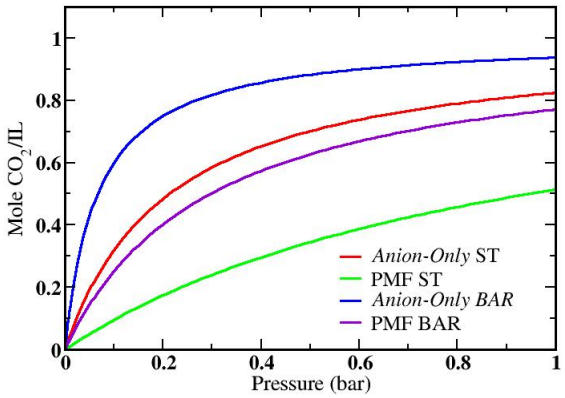

Figure D.1. All 333 K calculated CO_2 absorption isotherms.

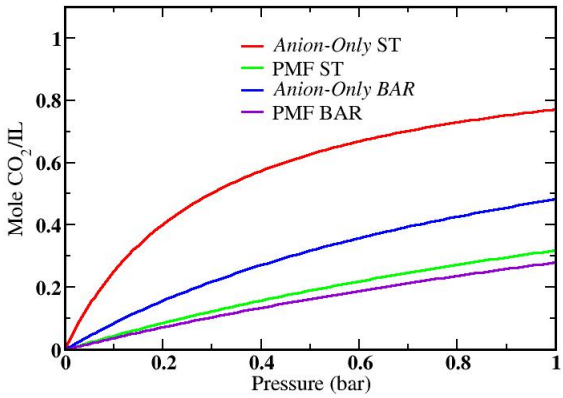

Figure D.2. All 360 K calculated CO_2 absorption isotherms.

APPENDIX E

PMF FREE ENERGY OF GAS PHASE REACTION

E.1 PMF Free Energy of Reaction Derivation

The goal of the PMF calculation is to find the standard state Gibbs free energy of the gas phase reaction between IL and CO_2 shown in eq. E.1

$$IL(g) + CO_2(g) \rightarrow IL : CO_2(g) \tag{E.1}$$

where IL represents a cation-anion pair which is considered to be a single molecular species. The PMF method discussed will be derived for the following generalized reaction shown eq. E.2.

$$A(g) + B(g) \rightarrow AB(g) \tag{E.2}$$

The total number of atoms in molecule A will be denoted as NA and the total number of atoms in B will be denoted as NB. The number of atoms in the AB molecule is simply the sum NA+NB. The reaction product of A and B is shown in figure E.1 to help clarify some of the terms used in the derivation.

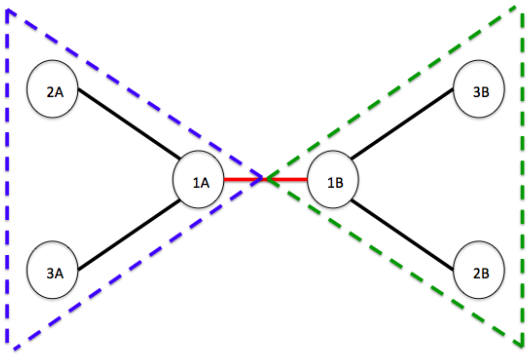

Figure E.1. An example AB molecule made from bonding an A fragment (dashed blue line) to a B fragment (dashed green line). Atoms are indicated by open circles. Bonds are indicated by solid lines. The red line between atoms 1A and 1B is the bond between the A and B fragments.

The free energy of reaction can be related to the equilibrium constant using eq. E.3 below

$$Keq = exp\left(\frac{-\Delta G^{\circ}_{rxn}}{RT}\right)\left(\frac{P^{\circ}}{\mathrm{R}T}\right)^{\Delta\nu} \tag{E.3}$$

where ΔG°_{rxn} is the standard state free energy of the gas phase reaction, R is the ideal gas law constant, T is the temperature, P° is the reference state pressure, $\Delta\nu$ is the difference in moles between the products and the reactants (-1 in this example). The standard state Gibbs free energy of reaction can be found by calculating Keq and and solving for the value of ΔG°_{rxn} at a given reference state pressure.

$$\Delta G^{\circ}_{rxn} = -\mathrm{R}T\ln\left[Keq\left(\frac{P^{\circ}}{RT}\right)^{-\Delta\nu}\right] \tag{E.4}$$

Here we will show how to calculate Keq using the potential of mean force (PMF). The equilibrium constant in eq. E.3 can also be expressed in terms of the molecular

partition functions of the reactant and product molecules shown in eq. E.5

$$Keq = \frac{\left(\frac{Q_{AB}}{V}\right)}{\left(\frac{Q_A}{V}\right)\left(\frac{Q_B}{V}\right)} \tag{E.5}$$

where Q_{AB} is the partition function of the product molecule, AB, Q_A is the partition function of the molecule A, Q_B is the partition function of the molecule B, and V is the volume. The partition functions for the reactant and product molecules can be expressed as phase space integrals by integrating the Boltzmann weighted Hamiltonian over the positions and momenta of all of the atoms in the A and B groups

$$Q_{AB} = \int\int d\vec{r}_{1A} d\vec{r}_{2A} ... d\vec{r}_{NA} d\vec{r}_{1B} d\vec{r}_{2B} ... d\vec{r}_{NB} d\vec{p}_{1A} d\vec{p}_{2A} ... d\vec{p}_{NA} d\vec{p}_{1B} d\vec{p}_{2B} ... d\vec{p}_{NB} \\ e^{-\beta H_{AB}(\vec{r}_{1A},\vec{r}_{2A},...\vec{r}_{NA},\vec{r}_{1B},\vec{r}_{2B},...\vec{r}_{NB},\vec{p}_{1A},\vec{p}_{2A},...\vec{p}_{NA},\vec{p}_{1B},\vec{p}_{2B},...\vec{p}_{NB})} \tag{E.6}$$

$$Q_A = \int\int d\vec{r}_{1A} d\vec{r}_{2A} ... d\vec{r}_{NA} d\vec{p}_{1A} d\vec{p}_{2A} ... d\vec{p}_{NA} e^{-\beta H_A(\vec{r}_{1A},\vec{r}_{2A},...\vec{r}_{NA},\vec{p}_{1A},\vec{p}_{2A},...\vec{p}_{NA})} \tag{E.7}$$

$$Q_B = \int\int d\vec{r}_{1B} d\vec{r}_{2B} ... d\vec{r}_{NB} d\vec{p}_{1B} d\vec{p}_{2B} ... d\vec{p}_{NB} e^{-\beta H_B(\vec{r}_{1B},\vec{r}_{2B},...\vec{r}_{NB},\vec{p}_{1B},\vec{p}_{2B},...\vec{p}_{NB})} \tag{E.8}$$

where β is the Boltzmann factor, $\frac{1}{k_B T}$, $\vec{r}_{1A}$ is the Cartesian coordinate of atom 1 in molecule A, $\vec{p}_{1A}$ is the momentum of the atom 1 in molecule A, H_{AB} is the Hamiltonian for molecule AB, H_A is the Hamiltonian for molecule A, H_B is the Hamiltonian for molecule B. Likewise, $\vec{r}_{1B}$ is the Cartesian coordinate of the atom 1 in molecule B and $\vec{p}_{1B}$ is the momentum of atom 1 in molecule B. When calculating the partition

function, we can split the Hamiltonian into the potential energy, U, and the Kinetic energy, K, because we have conservative forces and the potential is a function of the positions only and not the momenta.

$$H = U + K \tag{E.9}$$

Therefore a general partition function for a molecule having N atoms can be described as follows:

$$\begin{aligned} Q &= \int\int d\vec{r}^N d\vec{p}^N e^{-\beta H(\vec{r}^N,\vec{p}^N)} \\ &= \int\int d\vec{r}^N d\vec{p}^N e^{-\beta(U(\vec{r}^N)+K(\vec{p}^N))} \\ &= \int\int d\vec{r}^N d\vec{p}^N e^{-\beta U(\vec{r}^N)} e^{-\beta K(\vec{p}^N)} \\ &= \int d\vec{r}^N e^{-\beta U(\vec{r}^N)} \int d\vec{p}^N e^{-\beta K(\vec{p}^N)} \end{aligned} \tag{E.10}$$

The potential energy function $U_A(\vec{r}_{1A}, \vec{r}_{2A}, ...\vec{r}_{NA})$ for molecule A accounts for all intramolecular interactions of the atoms within molecule A. Likewise, the potential energy function $U_B(\vec{r}_{1B}, \vec{r}_{2B}, ...\vec{r}_{NB})$ for molecule B accounts for all intramolecular interactions of the atoms within molecule B. The potential $U_{AB}(\vec{r}_{1A}, \vec{r}_{2A}, ...\vec{r}_{NA}, \vec{r}_{1B}, \vec{r}_{2B}, ...\vec{r}_{NB})$ accounts for all intramolecular interaction within the A fragment (U_A), the intramolecular interactions within the B fragment, (U_B), and the interaction between the A fragment and the B fragment which will be denoted as $\chi_{AB}(\vec{r}_{1A}, \vec{r}_{2A}, ...\vec{r}_{NA}, \vec{r}_{1B}, \vec{r}_{2B}, ...\vec{r}_{NB})$. Therefore, the potential energy of AB can be written in terms of the potential of A and the potential of B shown in eq. E.11.

$$\begin{aligned} U_{AB} =& U_A(\vec{r}_{1A}, \vec{r}_{2A}, ...\vec{r}_{NA}) + U_B(\vec{r}_{1B}, \vec{r}_{2B}, ...\vec{r}_{NB}) \\ &+ \chi_{AB}(\vec{r}_{1A}, \vec{r}_{2A}, ...\vec{r}_{NA}, \vec{r}_{1B}, \vec{r}_{2B}, ...\vec{r}_{NB}) \end{aligned} \tag{E.11}$$

When the A fragment is sufficiently far away from the B fragment such that the two no longer interact, χ_{AB} is zero and the potential for AB reduces to the sum of the potentials for the A and B fragments. When integrating to calculate the partition function, we are free to choose the origin (the partition function does not depend on the reference frame of our system). Therefore we will choose the coordinates of the first atom in A, $\vec{r}_{1A}$ as the origin when calculating the partition function of A and AB. When we calculate the partition function for B, we will set the location of the first atom in B to be the origin. Additionally, we will assume for this reaction that a bond forms between the first atom of A and the first atom of B to make the molecule AB. In the following section, we will operate on our expressions for the partition functions to get a function for Keq based on eq. E.5.

$$Q_{AB} = \int d\vec{r}_{1A} \int d\vec{r}_{2A}...d\vec{r}_{NA}d\vec{r}_{1B}d\vec{r}_{2B}...d\vec{r}_{NB}d\vec{p}_{1A}e^{-\beta U_{AB}(\vec{r}_{2A},...\vec{r}_{NA},\vec{r}_{1B},\vec{r}_{2B},...\vec{r}_{NB})} \int d\vec{p}_{1A}d\vec{p}_{2A}...d\vec{p}_{NA}d\vec{p}_{1B}d\vec{p}_{2B}...d\vec{p}_{NB}d\vec{p}_{1A}e^{-\beta K(\vec{p}_{1A},\vec{p}_{2A},...\vec{p}_{NA},\vec{p}_{1B},\vec{p}_{2B},...\vec{p}_{NB})} \tag{E.12}$$

The first integral in the above expression $\int d\vec{r}_{1A}$ simply gives the volume, V. Additionally, the integral over all of the atomic momenta is a constant which we will refer to as P_{AB}. Therefore we can simplify eq. E.12 to eq. E.13.

$$Q_{AB}/V = P_{AB} \int d\vec{r}_{2A}...d\vec{r}_{NA}d\vec{r}_{1B}d\vec{r}_{2B}...d\vec{r}_{NB}e^{-\beta U_{AB}(\vec{r}_{2A},...\vec{r}_{NA},\vec{r}_{1B},\vec{r}_{2B},...\vec{r}_{NB})} \tag{E.13}$$

In similar fashion, we can get expressions for Q_A/V and Q_B/V shown in eqs. E.15

and E.16 starting with eq. E.14

$$Q_A = \int d\vec{r}_{1A} \int d\vec{r}_{2A}...d\vec{r}_{NA} e^{-\beta U_A(\vec{r}_{2A},...\vec{r}_{NA})} \int d\vec{p}_{1A} d\vec{p}_{2A}...d\vec{p}_{NA} e^{-\beta K(\vec{p}_{1A},\vec{p}_{2A},...\vec{p}_{NA})} \tag{E.14}$$

where we will refer to the integral over all the moment for molecule A as P_A. Making this substitution for the momenta integral, Q_A/V is given by eq. E.15.

$$Q_A/V = P_A \int d\vec{r}_{2A}...d\vec{r}_{NA} e^{-\beta U_A(\vec{r}_{2A},...\vec{r}_{NA})} \tag{E.15}$$

We will refer to the integral over the momenta of the atoms of molecule B as P_B. This gives us a similar expression for Q_B/V in eq. E.16.

$$Q_B/V = P_B \int d\vec{r}_{2B}...d\vec{r}_{NB} e^{-\beta U(\vec{r}_{2B},...\vec{r}_{NB})} \tag{E.16}$$

Since we are integrating over all of the atomic momenta separately, we can relate P_{AB} to P_A and P_B using eq. E.17.

$$\begin{aligned} P_{AB} &= \int d\vec{p}_{1A} d\vec{p}_{2A}...d\vec{p}_{NA} d\vec{p}_{1B} d\vec{p}_{2B}...d\vec{p}_{NB} e^{-\beta K(\vec{p}_{1A},\vec{p}_{2A},...\vec{p}_{NA},\vec{p}_{1B},\vec{p}_{2B},...\vec{p}_{NB})} \\ &= \int d\vec{p}_{1A} d\vec{p}_{2A}...d\vec{p}_{NA} e^{-\beta K(\vec{p}_{1A},\vec{p}_{2A},...\vec{p}_{NA})} \int d\vec{p}_{1B} d\vec{p}_{2B}, ...d\vec{p}_{NB} e^{-\beta K(\vec{p}_{1B},\vec{p}_{2B},...\vec{p}_{NB})} \\ &= P_A P_B \end{aligned} \tag{E.17}$$

We can integrate the potential energy term for Q_A and Q_B together in a single

integral if we introduce the constraint that the two molecules are separated enough that there is no interaction between them (χ_{AB} is 0 and there is no force between the two fragments). We shall refer to the separation at which A and B are fully dissociated and no longer interact with each other as $\vec{r}_D$. The first atom in A has been set as the origin so that the bond length between A and B is given by the magnitude of $\vec{r}_{1B}$. We can then integrate both partition functions by introducing a delta Dirac function into the integral by constraining the bond length $\vec{r}_{1B}$ (the integrand is zero for all values of $\vec{r}_{1B}$ other than the constraint length) which gives the following expression for the denominator in eq. E.5.

$$\begin{aligned}\left(\frac{Q_A}{V}\right)\left(\frac{Q_B}{V}\right) =& \left(P_A \int d\vec{r}_{2A}, ...d\vec{r}_{NA} e^{-\beta U_A(\vec{r}_{2A},...\vec{r}_{NA})}\right)\left(P_B \int d\vec{r}_{2B}, ...d\vec{r}_{NB} e^{-\beta U_B(\vec{r}_{2B},...\vec{r}_{NB})}\right) \\ =& P_A P_B \int (d\vec{r}_{2A}, ...d\vec{r}_{NA} d\vec{r}_{1B} d\vec{r}_{2B}, ...d\vec{r}_{NB} \delta\left(\vec{r}_{1B} - \vec{r}_D\right) \\ & e^{-\beta U_{AB}(\vec{r}_{2A},...\vec{r}_{NA},\vec{r}_{1B},\vec{r}_{2B},...\vec{r}_{NB})})\end{aligned} \tag{E.18}$$

Subbing eqs. E.13 and E.18 into eq. E.5 results in eq. E.19.

$$\begin{aligned}\frac{\left(\frac{Q_{AB}}{V}\right)}{\left(\frac{Q_A}{V}\right)\left(\frac{Q_B}{V}\right)} &= \frac{P_{AB} \int d\vec{r}_{2A}...d\vec{r}_{NA} d\vec{r}_{1B} dr_{2B}...d\vec{r}_{NB} e^{-\beta U_{AB}(\vec{r}_{2A},...\vec{r}_{NA},\vec{r}_{1B},\vec{r}_{2B},...\vec{r}_{NB})}}{\left(P_A \int d\vec{r}_{2A}...d\vec{r}_{NA} e^{-\beta U_A(\vec{r}_{2A},...\vec{r}_{NA})}\right)\left(P_B \int d\vec{r}_{2B}...d\vec{r}_{NB} e^{-\beta U_B(\vec{r}_{2B},...\vec{r}_{NB})}\right)} \\ &= \frac{\int d\vec{r}_{2A}...d\vec{r}_{NA} d\vec{r}_{1B} d\vec{r}_{2B}...d\vec{r}_{NB} e^{-\beta U_{AB}(\vec{r}_{2A},...\vec{r}_{NA},\vec{r}_{1B},\vec{r}_{2B},...\vec{r}_{NB})}}{\int d\vec{r}_{2A}...d\vec{r}_{NA} d\vec{r}_{1B} d\vec{r}_{2B}...d\vec{r}_{NB} \delta\left(\vec{r}_{1B} - \vec{r}_D\right) e^{-\beta U_{AB}(\vec{r}_{2A},...\vec{r}_{NA},\vec{r}_{1B},\vec{r}_{2B},...\vec{r}_{NB})}}\end{aligned} \tag{E.19}$$

Now we can relate this expression to the three dimensional PMF, $\hat{W}(\vec{r}_{1B})$, using eq. E.20

$$\frac{d\hat{W}(\vec{r}_{1B})}{d\vec{r}_{1B}} = -\left\langle \vec{F}(\vec{r}_{1B}) \right\rangle \tag{E.20}$$

where r_{1B} is the bond length between the first atom of A and the first atom of B. The average constraint force, $\left\langle \vec{F}(\vec{r}_{1B}) \right\rangle$ can be sampled using constraint dynamics. The constraint force can be integrated along $\vec{r}_{1B}$ to get a profile for $\hat{W}(\vec{r}_{1B})$. We can relate $\hat{W}(\vec{r}_{1B})$ to phase space integrals of our AB system using the following expression:

$$e^{-\beta \hat{W}(\vec{r}_{1B})} = \int d\vec{r}_{2A}...d\vec{r}_{NA}d\vec{r}_{2B}...d\vec{r}_{NB}e^{-\beta U_{AB}(\vec{r}_{2A}...\vec{r}_{NA}\vec{r}_{1B},\vec{r}_{2B}...\vec{r}_{NB})} \tag{E.21}$$

The numerator and the denominator on the right hand side of of eq. E.5 can now be expressed in terms of the PMF as shown in eq. E.22.

$$\frac{\left(\frac{Q_{AB}}{V}\right)}{\left(\frac{Q_A}{V}\right)\left(\frac{Q_B}{V}\right)} = \frac{\int d\vec{r}_{1B}e^{-\beta \hat{W}(\vec{r}_{1B})}}{e^{-\beta \hat{W}(\vec{r}_D)}} \tag{E.22}$$

It is useful to convert our expression for the three dimensional PMF, $\hat{W}(\vec{r}_{1B})$, into a one dimensional PMF that only depends on the bond length and not the orientation. Here we can change from Cartesian coordinates to spherical coordinates in order to get a PMF which only depends on radial distance by integrating over the angular coordinates. First we shall define the bond length between the A and B fragments as r_{1B}.

$$\begin{aligned} |r_{1A,1B}| &= |\vec{r}_{1B} - \vec{r}_{1A}| \\ &= |\vec{r}_{1B} - \vec{0}| \\ &= |\vec{r}_{1B}| \\ &= r_{1B} \end{aligned} \tag{E.23}$$

We can reduce our PMF from three dimensions to one dimension by integrating

the angular dependencies in our three dimensional PMF.

$$e^{-\beta\hat{W}(\vec{r}_D)} = e^{-\beta\hat{W}(r_D,\theta,\phi)} \tag{E.24}$$

We can integrate over the θ and ϕ coordinates in this case because the A and B fragments are at the dissociation distance and therefore, there is no angular dependence in the potential between the two fragments.

$$\begin{aligned} e^{-\beta W(r_D)} &= \int d\phi d\theta Sin\theta e^{-\beta\hat{W}(r_D,\theta,\phi)} \\ &= 4\pi e^{-\beta\hat{W}(\vec{r}_D)} \end{aligned} \tag{E.25}$$

where $W(r_D)$ is the one dimensional PMF evaluated at the dissociation distance. We can use a similar approach to get the numerator of eq. E.22. Here we will introduce the Jacobian for the $d\vec{r}_{1B}$ term:

$$d\vec{r}_{1B} = d\phi d\theta dr_{1B} r_{1B}^2 Sin\theta \tag{E.26}$$

Subbing the Jacobian into the numerator we get

$$\begin{aligned} \int d\vec{r}_{1B} e^{-\beta\hat{W}(\vec{r}_{1B})} &= \int dr_{1B} r_{1B}^2 d\phi d\theta Sin\theta e^{-\beta\hat{W}(r_{1B},\theta,\phi)} \\ &= \int dr_{1B} r_{1B}^2 e^{-\beta W(r_{1B})} \end{aligned} \tag{E.27}$$

In this case we do not have spherical symmetry and we are not able to determine a constant from integrating over the angular coordinates. By subbing eq. E.25 and E.27 into E.22 we get the following expression for Keq.

$$K_{eq} = 4\pi \int_0^{r^*} r_{1B}^2 e^{-\beta[W(r_{1B})-W(r_D)]} dr_{1B} \tag{E.28}$$

The integral bounds in the numerator here cover the range of distances for r_{1B} which define the state of the product molecule AB. Now we can solve for the standard state free energy of reaction shown in eq. E.29 by equating the right hand sides of eqs. E.3 and E.28.

$$\begin{aligned}\Delta G^{\circ}_{rxn} &= -RT \ln \left[Keq \left(\frac{P^{\circ}}{k_B T} \right)^{-\Delta\nu} \right] \\ &= -RT \ln \left[4\pi \int_0^{r^*} r_{1B}^2 e^{-\beta[W(r_{1B})-W(r_D)]} dr_{1B} \left(\frac{P^{\circ}}{k_B T} \right)^{-\Delta\nu} \right]\end{aligned} \tag{E.29}$$

BIBLIOGRAPHY

1. Gurkan, B. E.; de la Fuente, J. C.; Mindrup, E. M.; Ficke, L. E.; Goodrich, B. F.; Price, E. A.; Schneider, W. F.; Brennecke, J. F. Equimolar CO_2 Absorption by Anion-Functionalized Ionic Liquids. *J. Amer. Chem. Soc.* **2010,** *132,* 2116-2117.

2. Goodrich, B. F.; de la Fuente, J. C.; Gurkan, B. E.; Zadigian, D. J.; Price, E. A.; Huang, Y.; Brennecke, J. F. Experimental Measurements of Amine-Functionalized Anion-Tethered Ionic Liquids with Carbon Dioxide. *Ind. Eng. Chem. Res.* **2011,** *50,* 111-118.

3. Firaha, D. S.; Kirchner, B. Tuning the Carbon Dioxide Absorption in Amino Acid Ionic Liquids. *ChemSusChem* **2016,** *9,* 1591–1599.

4. Phan, L.; Chiu, D.; Heldebrant, D. J.; Huttenhower, H.; John, E.; Li, X.; Pollet, P.; Wang, R.; Eckert, C. A.; Liotta, C. L.; *et al.*, Switchable Solvents Consisting of Amidine/Alcohol or Guanidine/Alcohol Mixtures. *Ind. Eng. Chem. Res.* **2008,** *47,* 539-545.

5. Li, A.; Tian, Z.; Yan, T.; Jiang, D.; Dai, S. Anion-Functionalized Task-Specific Ionic Liquids: Molecular Origin of Change in Viscosity upon CO_2 Capture. *J. Phys. Chem. B* **2014,** *118,* 14880-14887.

6. Gurkan, B.; Goodrich, B. F.; Mindrup, E. M.; Ficke, L. E.; Massel, M.; Seo, S.; Senftle, T. P.; Wu, H.; Glaser, M. F.; Shah, J. K.; *et al.*, Molecular Design of High Capacity, Low Viscosity, Chemically Tunable Ionic Liquids for CO_2 Capture. *J. Phys. Chem. Lett.* **2010,** *1,* 3494-3499.

7. Seo, S.; Quiroz-Guzman, M.; DeSilva, M. A.; Lee, T. B.; Huang, Y.; Goodrich, B. F.; Schneider, W. F.; Brennecke, J. F. Chemically Tunable Ionic Liquids with Aprotic Heterocyclic Anion (AHA) for CO_2 Capture. *J. Phys. Chem. B* **2014,** *118,* 5740-5751.

8. Wang, C.; Luo, H.; Jiang, D.; Li, H.; Dai, S. Carbon Dioxide Capture by Superbase-Derived Protic Ionic Liquids. *Ang. Chem. Int. Ed.* **2010,** *122,* 6114-6117.

9. Teague, C. M.; Dai, S.; Jiang, D. Computational Investigation of Reactive to Nonreactive Capture of Carbon Dioxide by Oxygen-Containing Lewis Bases. *J. Phys. Chem. A* **2010,** *114,* 11761-11767.

10. Mercy, M.; Taylor, S. F. R.; Jacquemin, J.; Hardacre, C.; Bell, R. G.; Leeuw, N. H. D. The Addition of CO_2 to Four Superbase Ionic Liquids: A DFT Study. *Phys. Chem. Chem. Phys.* **2015,** 28674-28682.

11. Luo, X. Y.; Ding, F.; Lin, W. J.; Qi, Y. Q.; Li, H. R.; Wang, C. M. Efficient and Energy-Saving CO_2 Capture through the Entropic Effect Induced by the Intermolecular Hydrogen Bonding in Anion-Functionalized Ionic Liquids. *J. Phys. Chem. Lett.* **2014,** *5,* 381-386.

12. Liu, H.; Dai, S.; Jiang, D. Solubility of Gases in a Common Ionic Liquid from Molecular Dynamics Based Free Energy Calculations. *J. Phys. Chem. B* **2014,** *118,* 2719-2725.

13. Yoo, B.; Shah, J. K.; Zhu, Y.; Maginn, E. J. Amphiphilic Interactions of Ionic Liquids with Lipid Biomembranes: A Molecular Simulation Study. *Soft Matter* **2014,** *10,* 8641-8651.

14. Brehm, M.; Kirchner, B. TRAVIS - A Free Analyzer and Visualizer for Monte Carlo and Molecular Dynamics Trajectories. *J. Chem. Inf. Model.* **2011,** *51,* 2007–2023.

15. Humphrey, W.; Dalke, A.; Schulten, K. VMD: Visual Molecular Dynamics. *J. Mol. Graphics* **1996,** *14,* 33-38.

16. Seo, S.; DeSilva, M. A.; Xia, H.; Brennecke, J. F. Effect of Cation on Physical Properties and CO_2 Solubility for Phosphonium-Based Ionic Liquids with 2-Cyanopyrrolide Anions. *J. Phys. Chem. B* **2015,** *119,* 11807-11814.

17. Figueroa, J. D.; Fout, T.; Plasynski, S.; McIlvried, H.; Srivastava, R. D. Advances in CO_2 Capture Technology-The U.S. Department of Energy's Carbon Sequestration Program. *Int. J. Greenhouse Gas Control* **2008,** *2,* 9-20.

18. Yang, H.; Xu, Z.; Fan, M.; Gupta, R.; Slimane, R. B.; Bland, A. E.; Wright, I. Progress in Carbon Dioxide Separation and Capture: A Review. *J. Env. Sci.* **2008,** *20,* 14-27.

19. Yazaydın, A. O.; Snurr, R. Q.; Park, T.; Koh, K.; Liu, J.; LeVan, M. D.; Benin, A. I.; Jakubczak, P.; Lanuza, M.; Galloway, D. B.; *et al.*, Screening of Metal-organic Frameworks for Carbon Dioxide Capture From Flue Gas Using a Combined Experimental and Modeling Approach. *J. Amer. Chem. Soc.* **2009,** *131,* 18198-18199.

20. Bhown, A. S.; Freeman, B. C. Analysis and Status of Post-combustion Carbon Dioxide Capture Technologies. *Environ. Sci. Technol.* **2011,** *45,* 8624-8632.

21. Samanta, A.; Zhao, A.; Shimizu, G. K.; Sarkar, P.; Gupta, R. Post-combustion CO_2 Capture Using Solid Sorbents: A Review. *Ind. Eng. Chem. Res.* **2011,** *51,* 1438-1463.

22. Sumida, K.; Rogow, D. L.; Mason, J. A.; McDonald, T. M.; Bloch, E. D.; Herm, Z. R.; Bae, T.; Long, J. R. Carbon Dioxide Capture in MetalOrganic Frameworks. *Chem. Rev.* **2012,** *112,* 724-781.

23. Creamer, A. E.; Gao, B. Carbon-based Adsorbents for Post-combustion CO_2 Capture: A Critical Review. *Environ. Sci. Technol.* **2016,** .

24. Pera-Titus, M.; Giroir-Fendler, A. Perovskite Membranes for CO_2 Capture-Current Trends and Future Prospects. *Perovskites and Related Mixed Oxides Concepts and Applications* **2016,** 881-928.

25. Luo, X.; Wang, C. The Development of Carbon Capture by Functionalized Ionic Liquids. *Curr. Opin. Green Sust. Chem.* **2017,** *3,* 33-38.

26. Solomon, S.; Qin, D.; Manning, M.; Chen, Z.; Marquis, M.; Averyt, K.; Tignor, M.; Miller, H. . In *Contribution of Working Group I to the Fourth Assessment Report of the Intergovernmental Panel on Climate Change*; Cambridge University Press: 2007.

27. Pachauri, R. K.; Allen, M. R.; Barros, V.; Broome, J.; Cramer, W.; Christ, R.; Church, J.; Clarke, L.; Dahe, Q.; Dasgupta, P.; *et al.*, *Climate Change 2014: Synthesis Report. Contribution of Working Groups I, II and III to the Fifth Assessment Report of the Intergovernmental Panel on Climate Change;* IPCC: 2014.

28. EPA, "EPA Proposes First Guidelines to Cut Carbon Pollution from Existing Power Plants/Clean Power Plan is Flexible Proposal to Ensure a Healthier Environment, Spur Innovation and Strengthen the Economy", 2-14.

29. Stern, N. H. *The Economics of Climate Change: The Stern Review;* cambridge University press: 2007.

30. Tol, R. S. The Marginal Damage Costs of Carbon Dioxide Emissions: An Assessment of the Uncertainties. *Energy Pol.* **2005,** *33,* 2064-2074.

31. Haszeldine, R. S. Carbon Capture and Storage: How Green Can Black Be? *Science* **2009,** *325,* 1647-1652.

32. Rochelle, G. T. Amine Scrubbing for CO_2 Capture. *Science* **2009,** *325,* 1652-1654.

33. Fisher, K.; Searcy, K.; Rochelle, G.; Ziaii, S.; Schubert, C. "Advanced Amine Solvent Formulations and Process Integration for Near-Term CO_2. Capture Success; Report Submitted to US Department of Energy; 2007", .

34. Brennecke, J. F.; Gurkan, B. E. Ionic Liquids for CO_2 Capture and Emission Reduction. *J. Phys. Chem. Lett.* **2010,** *1,* 3459-3464.

35. Shiflett, M. B.; Drew, D. W.; Cantini, R. A.; Yokozeki, A. Carbon Dioxide Capture Using Ionic Liquid 1-Butyl-3-methylimidazolium Acetate. *Energy Fuels* **2010,** *24,* 5781-5789.

36. Vaidya, P. D.; Kenig, E. Y. CO_2-Alkanolamine Reaction Kinetics: A Review of Recent Studies. *Chem. Eng. Technol.* **2007,** *30,* 1467-1474.

37. McCann, N.; Phan, D.; Wang, X.; Conway, W.; Burns, R.; Attalla, M.; Puxty, G.; Maeder, M. Kinetics and Mechanism of Carbamate Formation from CO_2 (aq), Carbonate Species, and Monoethanolamine in Aqueous Solution. *J. Phys. Chem. A* **2009,** *113,* 5022-5029.

38. Xie, H.; Zhou, Y.; Zhang, Y.; Johnson, J. K. Reaction Mechanism of Monoethanolamine with CO_2 in Aqueous Solution from Molecular Modeling. *J. Phys. Chem. A* **2010,** *114,* 11844-11852.

39. Sakwattanapong, R.; Aroonwilas, A.; Veawab, A. Behavior of Reboiler Heat Duty for CO_2 Capture Plants Using Regenerable Single and Blended Alkanolamines. *Ind. Eng. Chem. Res.* **2005,** *44,* 4465-4473.

40. Oyenekan, B. A.; Rochelle, G. T. Energy Performance of Stripper Configurations for CO_2 Capture by Aqueous Amines. *Ind. Eng. Chem. Res.* **2006,** *45,* 2457-2464.

41. Goto, K.; Yogo, K.; Higashii, T. A Review of Efficiency Penalty in a Coal-fired Power Plant with Post-combustion CO_2 Capture. *Appl. Energy* **2013,** *111,* 710-720.

42. Goff, G. S.; Rochelle, G. T. Monoethanolamine Degradation: O_2 Mass Transfer Effects under CO_2 Capture Conditions. *Ind. Eng. Chem. Res.* **2004,** *43,* 6400-6408.

43. Davis, J.; Rochelle, G. Thermal Degradation of Monoethanolamine at Stripper Conditions. *Energy Procedia* **2009,** *1,* 327-333.

44. Supap, T.; Idem, R.; Tontiwachwuthikul, P.; Saiwan, C. Kinetics of Sulfur Dioxide- and Oxygen-induced Degradation of Aqueous Monoethanolamine Solution During CO_2 Absorption from Power Plant Flue Gas Streams. *Int. J. Greenhouse Gas Control* **2009,** *3,* 133-142.

45. Lepaumier, H.; Picq, D.; Carrette, P. New Amines for CO_2 Capture. I. Mechanisms of Amine Degradation in the Presence of CO_2. *Ind. Eng. Chem. Res.* **2009,** *48,* 9061-9067.

46. Rau, A. B.; Rubin, E. S. A Technical, Economic, and Environmental Assessment of Amine-Based CO_2 Capture Technology for Power Plant Greenhouse Gas Control. *Environ. Sci. Technol.* **2002,** *36,* 4467-4475.

47. Nguyen, T.; Hilliard, M.; Rochelle, G. T. Amine Volatility in CO_2 Capture. *Int. J. Greenhouse Gas Control* **2010,** *4,* 707-715.

48. Nguyen, T.; Hilliard, M.; Rochelle, G. Volatility of Aqueous Amines in CO_2 Capture. *Energy Procedia* **2011,** *4,* 1624-1630.

49. Mertens, J.; Lepaumier, H.; Desagher, D.; Thielens, M.-L. Understanding Ethanolamine (MEA) and Ammonia Emissions from Amine Based Post Combustion Carbon Capture: Lessons Learned from Field Tests. *Int. J. Greenhouse Gas Control* **2013,** *13,* 72-77.

50. Strazisar, B. R.; Anderson, R. R.; White, C. M. Degradation Pathways for Monoethanolamine in a CO_2 Capture Facility. *Energy Fuels* **2003,** *17,* 1034-1039.

51. Goff, G. S.; Rochelle, G. T. Monoethanolamine Degradation: O_2 Mass Transfer Effects Under CO_2 Capture Conditions. *Ind. Eng. Chem. Res.* **2004,** *43,* 6400-6408.

52. Kladkaew, N.; Idem, R.; Tontiwachwuthikul, P.; Saiwan, C. Corrosion Behavior of Carbon Steel in the Monoethanolamine- H_2O- CO_2- O_2- SO_2 System: Products, Reaction Pathways, and Kinetics. *Ind. Eng. Chem. Res.* **2009,** *48,* 10169-10179.

53. Seddon, K. R. Ionic Liquids for Clean Technology. *J. Chem. Technol. Biotechnol.* **1997,** *68,* 351-356.

54. Cadena, C.; Anthony, J. L.; Shah, J. K.; Morrow, T. I.; Brennecke, J. F.; Maginn, E. J. Why Is CO_2 So Soluble in Imidazolium-Based Ionic Liquids? *J. Amer. Chem. Soc.* **2004,** *126,* 5300-5308.

55. Camper, D.; Scovazzo, P.; Koval, C.; Noble, R. Gas Solubilities in Room-Temperature Ionic Liquids. *Ind. Eng. Chem. Res.* **2004,** *43,* 3049-3054.

56. Anderson, J. L.; Dixon, J. K.; Brennecke, J. F. Solubility of CO_2, CH_4, C_2H_6, C2H4, O_2, and N_2 in 1-Hexyl-3-methylpyridinium Bis(trifluoromethylsulfonyl)imide: Comparison to Other Ionic Liquids. *Acc. Chem. Res.* **2007,** *40,* 1208-1216.

57. Bara, J. E.; Gabriel, C. J.; Lessmann, S.; Carlisle, T. K.; Finotello, A.; Gin, D. L.; Noble, R. D. Enhanced CO_2 Separation Selectivity in Oligo(ethylene glycol) Functionalized Room-Temperature Ionic Liquids. *Ind. Eng. Chem. Res.* **2007,** *46,* 5380-5386.

58. Bara, J. E.; Carlisle, T. K.; Gabriel, C. J.; Camper, D.; Finotello, A.; Gin, D. L.; Noble, R. D. Guide to CO_2 Separations in Imidazolium-Based Room-Temperature Ionic Liquids. *Ind. Eng. Chem. Res.* **2009,** *48,* 2739-2751.

59. Blanchard, L. A.; Hancu, D.; Beckman, E. J.; Brennecke, J. F. Green Processing Using Ionic Liquids and CO_2. *Nature* **1999,** *399,* 28-29.

60. Earle, M. J.; Seddon, K. R. Ionic Liquids: Green Solvents for the Future. In

61. Perissi, I.; Bardi, U.; Caporali, S.; Lavacchi, A. High Temperature Corrosion Properties of Ionic Liquids. *Corros. Sci.* **2006,** *48,* 2349-2362.

62. Pisarova, L.; Gabler, C.; Dörr, N.; Pittenauer, E.; Allmaier, G. Thermo-oxidative Stability and Corrosion Properties of Ammonium Based Ionic Liquids. *Tribol. Int.* **2012,** *46,* 73-83.

63. Uerdingen, M.; Treber, C.; Balser, M.; Schmitt, G.; Werner, C. Corrosion Behaviour of Ionic Liquids. *Green Chem.* **2005,** *7,* 321-325.

64. Arenas, M.; Reddy, R. Corrosion of Steel in Ionic Liquids. *J. Min. Metall. Sect. B Metall.* **2003,** *39,* 81-91.

65. Maginn, E. J. Molecular Simulation of Ionic Liquids: Current Status and Future Opportunities. *J. Phys. Condens. Matter* **2009,** *21,* 373101.

66. Huang, J.; Rüther, T. Why Are Ionic Liquids Attractive for CO_2 Absorption? An Overview. *Aust. J. Chem.* **2009,** *62,* 298-308.

67. Karadas, F.; Atilhan, M.; Aparicio, S. Review on The Use of Ionic Liquids (ILs) as Alternative Fluids for CO_2 Capture and Natural Gas Sweetening. *Energy Fuels* **2010,** *24,* 5817-5828.

68. Shannon, M. S.; Bara, J. E. Reactive and Reversible Ionic Liquids for CO_2 Capture and Acid Gas Removal. *Separ. Sci. Technol.* **2012,** *47,* 178-188.

69. Zhang, X.; Zhang, X.; Dong, H.; Zhao, Z.; Zhang, S.; Huang, Y. Carbon Capture with Ionic Liquids: Overview and Progress. *Energy Environ. Sci.* **2012,** *5,* 6668-6681.

70. Ramdin, M.; de Loos, T. W.; Vlugt, T. J. State-of-the-Art of CO_2 Capture with Ionic Liquids. *Ind. Eng. Chem. Res.* **2012,** *51,* 8149-8177.

71. Babamohammadi, S.; Shamiri, A.; Aroua, M. K. A Review of CO_2 Capture by Absorption in Ionic Liquid-based Solvents. *Rev. Chem. Eng.* **2015,** *31,* 383-412.

72. Tian, Z.; Dai, S.; Jiang, D. What Can Molecular Simulation Do for Global Warming? *Wiley Interdiscip. Rev. Comput. Mol. Sci.* **2016,** *6,* 173-197.

73. Sarmad, S.; Mikkola, J.; Ji, X. CO_2 Capture with Ionic liquids (ILs) and Deep Eutectic Solvents (DESs): A New Generation of Sorbents. *ChemSusChem* **2016,** .

74. Cui, G.; Wang, J.; Zhang, S. Active Chemisorption Sites in Functionalized Ionic Liquids for Carbon Capture. *Chem. Soc. Rev.* **2016,** 4307-4339.

75. Bhargava, B. L.; Balasubramanian, S. Insights into the Structure and Dynamics of a Room-Temperature Ionic Liquid: Ab Initio Molecular Dynamics Simulation Studies of 1-n-Butyl-3-methylimidazolium Hexafluorophosphate ([bmim][PF_6]) and the [bmim][PF_6]-CO_2 Mixture. *J. Phys. Chem. B* **2007,** *111,* 4477-4487.

76. Bara, J. E.; Camper, D. E.; Gin, D. L.; Noble, R. D. Room-Temperature Ionic Liquids and Composite Materials: Platform Technologies for CO_2 Capture. *Acc. Chem. Res.* **2010,** *43,* 152-159.

77. Bates, E. D.; Mayton, R. D.; Ntai, I.; Davis Jr., J. H. CO_2 Capture by a Task-Specific Ionic Liquid. *J. Amer. Chem. Soc.* **2002,** *124,* 926-927.

78. Yu, G.; Zhang, S.; Zhou, G.; Liu, X.; Chen, X. Structure, Interaction and Property of Amino-functionalized Imidazolium ILs by Molecular Dynamics Simulation and Ab Initio Calculation. *AIChE J.* **2007,** *53,* 3210-3221.

79. Gutowski, K. E.; Maginn, E. J. Amine-Functionalized Task-Specific Ionic Liquids: A Mechanistic Explanation for the Dramatic Increase in Viscosity upon Complexation with CO_2 from Molecular Simulation. *J. Amer. Chem. Soc.* **2008,** *130,* 14690-14704.

80. Camper, D.; Bara, J. E.; Gin, D. L.; Noble, R. D. Room-Temperature Ionic Liquid-Amine Solutions: Tunable Solvents for Efficient and Reversible Capture of CO_2. *Ind. Eng. Chem. Res.* **2008,** *47,* 8496-8498.

81. Yin, Y.; Zhu, C.; Ma, Y. Volumetric and Viscometric Properties of Binary and Ternary Mixtures of 1-Butyl-3-methylimidazolium Tetrafluoroborate, Monoethanolamine and Water. *J. Chem. Thermodyn.* **2016,** *102,* 413-428.

82. Mindrup, E. M.; Schneider, W. F. Computational Comparison of Tethering Strategies for Amine Functionalised Ionic Liquids. In ; ACS Publications: 2010.

83. Ohno, H.; Fukumoto, K. Amino Acid Ionic Liquids. *Acc. Chem. Res.* **2007,** *40,* 1122-1129.

84. Fukumoto, K.; Yoshizawa, M.; Ohno, H. Room Temperature Ionic Liquids from 20 Natural Amino Acids. *J. Amer. Chem. Soc.* **2005,** *127,* 2398-2399.

85. Zhang, J.; Zhang, S.; Dong, K.; Zhang, Y.; Shen, Y.; Lv, X. Supported Absorption of CO_2 by Tetrabutylphosphonium Amino Acid Ionic Liquids. *Chem. Eur. J.* **2006,** *12,* 4021-4026.

86. Luo, X. Y.; Fan, X.; Shi, G. L.; Li, H. R.; Wang, C. M. Decreasing the Viscosity in CO_2 Capture by Amino-Functionalized Ionic Liquids through the Formation of Intramolecular Hydrogen Bond. *J. Phys. Chem. B* **2016,** *120,* 2807-2813.

87. Gurkan, B. E.; Gohndrone, T. R.; McCready, M. J.; Brennecke, J. F. Reaction Kinetics of CO_2 Absorption in to Phosphonium Based Anion-functionalized Ionic Liquids. *Phys. Chem. Chem. Phys.* **2013,** *15,* 7796-7811.

88. Zhang, B.; van Duin, A. C. T.; Johnson, J. K. Development of a ReaxFF Reactive Force Field for Tetrabutylphosphonium Glycinate/CO_2 Mixtures. *J. Phys. Chem. B* **2014,** *118,* 12008-12016.

89. van Duin, A. C.; Dasgupta, S.; Lorant, F.; Goddard, W. A. ReaxFF: A Reactive Force Field for Hydrocarbons. *J. Phys. Chem. A* **2001,** *105,* 9396-9409.

90. Chenoweth, K.; van Duin, A. C.; Goddard, W. A. ReaxFF Reactive Force Field for Molecular Dynamics Simulations of Hydrocarbon Oxidation. *J. Phys. Chem. A* **2008,** *112,* 1040-1053.

91. Zhou, G.; Liu, X.; Zhang, S.; Yu, G.; He, H. A Force Field for Molecular Simulation of Tetrabutylphosphonium Amino Acid Ionic Liquids. *J. Phys. Chem. B* **2007,** *111,* 7078-7084.

92. Maginn, E. J. Design and Evaluation of Ionic Liquids as Novel CO_2 Absorbents, Quarterly Technical Report to DOE. December 31, 2004; January 31, 2005; May 31, 2005; August 16, 2005; November 20, 2005; January 12, 2006.

93. Shiflett, M. B.; Kasprzak, D. J.; Junk, C. P.; Yokozeki, A. Phase Behavior of Carbon Dioxide + [bmim][Ac] Mixtures. *J. Chem. Thermodyn.* **2008,** *40,* 25-31.

94. Shiflett, M. B.; Yokozeki, A. Phase Behavior of Carbon Dioxide in Ionic Liquids: [emim][Acetate], [emim][Trifluoroacetate], and [emim][Acetate] + [emim][Trifluoroacetate] Mixtures. *J. Chem. Eng. Data* **2009,** *54,* 108-114.

95. Gurau, G.; Rodríguez, H.; Kelley, S. P.; Janiczek, P.; Kalb, R. S.; Rogers, R. D. Demonstration of Chemisorption of Carbon Dioxide in 1,3-Dialkylimidazolium Acetate Ionic Liquids. *Ang. Chem. Int. Ed.* **2011,** *50,* 12024-12026.

96. Besnard, M.; Cabaco, M. I.; Vaca Chávez, F.; Pinaud, N.; Sebastião, P. J.; Coutinho, J. A. P.; Mascetti, J.; Danten, Y. CO_2 in 1-Butyl-3-methylimidazolium Acetate. 2. NMR Investigation of Chemical Reactions. *J. Phys. Chem. A* **2012,** *116,* 4890-4901.

97. Cabaco, M. I.; Besnard, M.; Danten, Y.; Coutinho, J. A. P. Carbon Dioxide in 1-Butyl-3-methylimidazolium Acetate. I. Unusual Solubility Investigated by Raman Spectroscopy and DFT Calculations. *J. Phys. Chem. A* **2012,** *116,* 1605-1620.

98. Hollóczki, O.; Kelemen, Z.; Könczöl, L.; Szieberth, D.; Nyulászi, L.; Stark, A.; Kirchner, B. Significant Cation Effects in Carbon Dioxide-Ionic Liquid Systems. *ChemPhysChem* **2013,** *14,* 315-320.

99. Brehm, M.; Weber, H.; Pensado, A. S.; Stark, A.; Kirchner, B. Proton Transfer and Polarity Changes in Ionic Liquid-water Mixtures: A Perspective on Hydrogen Bonds from Ab Initio Molecular Dynamics at the Example of 1-Ethyl-3-methylimidazolium Acetate-water Mixtures-Part 1. *Phys. Chem. Chem. Phys.* **2012,** *14,* 5030-5044.

100. Brehm, M.; Weber, H.; Pensado, A. S.; Stark, A.; Kirchner, B. Liquid Structure and Cluster Formation in Ionic Liquid/Water Mixtures-An Extensive Ab Initio Molecular Dynamics Study on 1-Ethyl-3-Methylimidazolium Acetate/Water Mixtures-Part. *Z. Phys. Chem.* **2013,** *227,* 177-204.

101. Jessop, P. G.; Heldebrant, D. J.; Li, X.; Eckert, C. A.; Liotta, C. L. Green Chemistry: Reversible Nonpolar-to-polar Solvent. *Nature* **2005,** *436,* 1102-1102.

102. Blasucci, V. M.; Hart, R.; Pollet, P.; Liotta, C. L.; Eckert, C. A. Reversible Ionic Liquids Designed for Facile Separations. *Fluid Phase Equilib.* **2010,** *294,* 1-6.

103. Jessop, P. G.; Mercer, S. M.; Heldebrant, D. J. CO_2-triggered Switchable Solvents, Surfactants, and Other Materials. *Energy Environ. Sci.* **2012,** *5,* 7240-7253.

104. Heldebrant, D. J.; Yonker, C. R.; Jessop, P. G.; Phan, L. Organic Liquid CO_2 Capture Agents with High Gravimetric CO_2 Capacity. *Eng. Env. Sci.* **2008,** *1,* 487-493.

105. Blasucci, V.; Dilek, C.; Huttenhower, H.; John, E.; Llopis-Mestre, V.; Pollet, P.; Eckert, C. A.; Liotta, C. L. One-component, Switchable Ionic Liquids Derived from Siloxylated Amines. *Chem. Commun.* **2009,** 116-118.

106. Hart, R.; Pollet, P.; Hahne, D. J.; John, E.; Llopis-Mestre, V.; Blasucci, V.; Huttenhower, H.; Leitner, W.; Eckert, C. A.; Liotta, C. L. Benign Coupling of Reactions and Separations with Reversible Ionic Liquids. *Tetrahedron* **2010,** *66,* 1082-1090.

107. Blasucci, V.; Hart, R.; Mestre, V. L.; Hahne, D. J.; Burlager, M.; Huttenhower, H.; Thio, B. J. R.; Pollet, P.; Liotta, C. L.; Eckert, C. A. Single Component, Reversible Ionic Liquids for Energy Applications. *Fuel* **2010,** *89,* 1315-1319.

108. Völkl, J.; Müller, K.; Mokrushina, L.; Arlt, W. A Priori Property Estimation of Physical and Reactive CO_2 Absorbents. *Chem. Eng. Technol.* **2012,** *35,* 579-583.

109. Gonzalez-Miquel, M.; Talreja, M.; Ethier, A. L.; Flack, K.; Switzer, J. R.; Biddinger, E. J.; Pollet, P.; Palomar, J.; Rodriguez, F.; Eckert, C. A.; *et al.*, COSMO-RS Studies: Structure-Property Relationships for CO_2 Capture by Reversible Ionic Liquids. *Ind. Eng. Chem. Res.* **2012,** *51,* 16066-16073.

110. Carvalho, P.; Kurnia, K.; Coutinho, J. Dispelling Some Myths About the CO_2 Solubility in Ionic Liquids. *PhysChemChemPhys* **2016,** *18,* 14757-14771.

111. Wu, H.; Shah, J. K.; Tenney, C. M.; Rosch, T. W.; Maginn, E. J. Structure and Dynamics of Neat and CO_2-Reacted Ionic Liquid Tetrabutylphosphonium 2-Cyanopyrrolide. *Ind. Eng. Chem. Res.* **2011,** *50,* 8983-8993.

112. Sheridan, Q. R.; Oh, S.; Morales-Collazo, O.; Castner Jr., E. W.; Brennecke, J. F.; Maginn, E. J. Liquid Structure of CO_2-Reactive Aprotic Heterocyclic Anion Ionic Liquids from X-ray Scattering and Molecular Dynamics. *J. Phys. Chem. B* **2016,** *120,* 11951-11960.

113. Gontrani, L.; Russina, O.; Celso, F. L.; Caminiti, R.; Annat, G.; Triolo, A. Liquid Structure of Trihexyltetradecylphosphonium Chloride at Ambient Temperature: An X-ray Scattering and Simulation Study. *J. Phys. Chem. B* **2009,** *113,* 9235-9240.

114. Bhargava, B. L.; Devane, R.; Klein, M. L.; Balasubramanian, S. Nanoscale Organization in Room Temperature Ionic Liquids: A Coarse Grained Molecular Dynamics Simulation Study. *Soft Matter* **2007,** *3,* 1395-1400.

115. Fujii, K.; Soejima, Y.; Kyoshoin, Y.; Fukuda, S.; Kanzaki, R.; Umebayashi, Y.; Yamaguchi, T.; Ishiguro, S.; Takamuku, T. Liquid Structure of Room-Temperature Ionic Liquid, 1-Ethyl-3-methylimidazolium Bis-(trifluoromethanesulfonyl) Imide. *J. Phys. Chem. B* **2008,** *112,* 4329-4336.

116. Fukuda, S.; Takeuchi, M.; Fujii, K.; Kanzaki, R.; Takamuku, T.; Chiba, K.; Yamamoto, H.; Umebayashi, Y.; Ishiguro, S. Liquid Structure of N-butyl-N-methylpyrrolidinium Bis(trifluoromethanesulfonyl) Amide Ionic Liquid Studied by Large Angle X-ray Scattering and Molecular Dynamics Simulations. *J. Mol. Liq.* **2008,** *143,* 2-7.

117. Kanzaki, R.; Mitsugi, T.; Fukuda, S.; Fujii, K.; Takeuchi, M.; Soejima, Y.; Takamuku, T.; Yamaguchi, T.; Umebayashi, Y.; Ishiguro, S. Ion-ion Interaction in Room Temperature Ionic Liquid 1-Ethyl-3-methylimidazolium Tetrafluoroborate Studied by Large Angle X-ray Scattering Experiment and Molecular Dynamics Simulations. *J. Mol. Liq.* **2009,** *147,* 77-82.

118. Hardacre, C.; Holbrey, J. D.; Mullan, C. L.; Youngs, T. G. A.; Bowron, D. T. Small Angle Neutron Scattering from 1-Alkyl-3-methylimidazolium Hexafluorophosphate Ionic Liquids (C(n)mim PF_6 , n=4, 6, and 8). *J. Chem. Phys.* **2010,** *133,* 074510.

119. Kashyap, H. K.; Santos, C. S.; Annapureddy, H. V. R.; Murthy, N. S.; Margulis, C. J.; Castner Jr., E. W. Temperature-dependent Structure of Ionic Liquids: X-ray Scattering and Simulations. *Faraday Discuss.* **2012,** *154,* 133-143.

120. Castner Jr., E. W.; Margulis, C. J.; Maroncelli, M.; Wishart, J. F. Ionic Liquids: Structure and Photochemical Reactions. *Annu. Rev. Phys. Chem.* **2011,** *62,* 85-105.

121. Wang, C.; Luo, H.; Luo, X.; Li, H.; Dai, S. Equimolar CO_2 Capture by Imidazolium-based Ionic Liquids and Superbase Systems. *Green Chem.* **2010,** *12,* 2019-2023.

122. Wang, C.; Mahurin, S. M.; Luo, H.; Baker, G. A.; Li, H.; Dai, S. Reversible and Robust CO_2 Capture by Equimolar Task-specific Ionic Liquid-superbase Mixtures. *Green Chem.* **2010,** *12,* 870-874.

123. Taylor, S. F. R.; McCrellis, C.; McStay, C.; Jacquemin, J.; Hardacre, C.; Mercy, M.; Bell, R. G.; de Leeuw, N. H. CO_2 Capture in Wet and Dry Superbase Ionic Liquids. *J. Solution Chem.* **2015,** *44,* 511-527.

124. Wang, C.; Luo, X.; Luo, H.; Jiang, D.; Li, H.; Dai, S. Tuning the Basicity of Ionic Liquids for Equimolar CO_2 Capture. *Ang. Chem. Int. Ed.* **2011,** *50,* 4918-4922.

125. Wang, C.; Luo, H.; Li, H.; Zhu, X.; Yu, B.; Dai, S. Tuning the Physicochemical Properties of Diverse Phenolic Ionic Liquids for Equimolar CO_2 Capture by the Substituent on the Anion. *Chem. Euro. J.* **2012,** *18,* 2153-2160.

126. Wu, C.; Senftle, T. P.; Schneider, W. F. First-principles-guided Design of Ionic Liquids for CO_2 Capture. *Phys. Chem. Chem. Phys.* **2012,** *14,* 13163-13170.

127. Mercy, M.; de Leeuw, N. H.; Bell, R. G. Mechanisms of CO_2 Capture in Ionic Liquids: A Computational Perspective. *Faraday Discuss.* **2016,** *192,* 479-492.

128. Firaha, D. S.; Hollóczki, O.; Kirchner, B. Computer-Aided Design of Ionic Liquids as CO_2 Absorbents. *Ang. Chem. Int. Ed.* **2015,** *54,* 7805-7809.

129. Gohndrone, T. R.; Lee, T.; DeSilva, M. A.; Quiroz-Guzman, M.; Schneider, W. F.; Brennecke, J. F. Competing Reactions of CO_2 with Cations and Anions in Azolide Ionic Liquids. *ChemSusChem* **2014,** *7,* 1970-1975.

130. Lee, T. B.; Oh, S.; Gohndrone, T. R.; Morales-Collazo, O.; Seo, S.; Brennecke, J. F.; Schneider, W. F. CO_2 Chemistry of Phenolate-Based Ionic Liquids. *J. Phys. Chem. B* **2016,** *120,* 1509-1517.

131. Hanke, C.; Atamas, N.; Lynden-Bell, R. Solvation of Small Molecules in Imidazolium Ionic Liquids: A Simulation Study. *Green Chem.* **2002,** *4,* 107-111.

132. Deschamps, J.; Costa Gomes, M. F.; Pádua, A. A. Molecular Simulation Study of Interactions of Carbon Dioxide and Water with Ionic Liquids. *ChemPhysChem* **2004,** *5,* 1049-1052.

133. Lynden-Bell, R. M.; Atamas, N. A.; Vasilyuk, A.; Hanke, C. G. Chemical Potentials of Water and Organic Solutes in Imidazolium Ionic Liquids: A Simulation Study. *Mol. Phys.* **2002,** *100,* 3225-3229.

134. Bennett, C. H. Efficient Estimation of Free Energy Differences from Monte Carlo Data. *J. Comput. Phys.* **1976,** *22,* 245-268.

135. Shah, J. K.; Maginn, E. J. Monte Carlo Simulations of Gas Solubility in the Ionic Liquid 1-n-Butyl-3-methylimidazolium Hexafluorophosphate. *J. Phys. Chem. B* **2005,** *109,* 10395-10405.

136. Landau, D. P.; Tsai, S.; Exler, M. A New Approach to Monte Carlo Simulations in Statistical Physics: Wang-Landau Sampling. *Am. J. Phys.* **2004,** *72,* 1294-1302.

137. Landau, D. P.; Wang, F. A New Approach to Monte Carlo Simulations in Statistical Physics. *Braz. J. Phys* **2004,** *34,* 354-362.

138. Shi, W.; Maginn, E. J. Molecular Simulation and Regular Solution Theory Modeling of Pure and Mixed Gas Absorption in the Ionic Liquid 1-n-Hexyl-3-methylimidazolium Bis(Trifluoromethylsulfonyl)amide ([hmim][Tf_2N]). *J. Phys. Chem. B* **2008,** *112,* 16710-16720.

139. Hert, D. G.; Anderson, J. L.; Aki, S. N.; Brennecke, J. F. Enhancement of Oxygen and Methane Solubility in 1-Hexyl-3-methylimidazolium Bis (trifluoromethylsulfonyl) Imide Using Carbon Dioxide. *Chem. Commun.* **2005,** 2603-2605.

140. Brennecke, J. F. American Chemical Society Meeting; Philadelphia, PA August 17, **2008**.

141. Shi, W.; Sorescu, D. C.; Luebke, D. R.; Keller, M. J.; Wickramanayake, S. Molecular Simulations and Experimental Studies of Solubility and Diffusivity for Pure and Mixed Gases of H_2, CO_2, and Ar Absorbed in the Ionic Liquid 1-n-Hexyl-3-methylimidazolium Bis(Trifluoromethylsulfonyl)amide ([hmim][Tf_2N]). *J. Phys. Chem. B* **2010,** *114,* 6531-6541.

142. Zhang, X.; Liu, Z.; Wang, W. Screening of Ionic Liquids to Capture CO_2 by COSMO-RS and Experiments. *AIChE J.* **2008,** *54,* 2717-2728.

143. Maiti, A. Theoretical Screening of Ionic Liquid Solvents for Carbon Capture. *ChemSusChem* **2009,** *2,* 628-631.

144. Anthony, J. L.; Maginn, E. J.; Brennecke, J. F. Solution Thermodynamics of Imidazolium-Based Ionic Liquids and Water. *J. Phys. Chem. B* **2001,** *105,* 10942-10949.

145. Tran, C. D.; Lacerda, S. H. D. P.; Oliveira, D. Absorption of Water by Room-temperature Ionic Liquids: Effect of Anions on Concentration and State of Water. *Appl. Spectrosc.* **2003,** *57,* 152-157.

146. Freire, M. G.; Carvalho, P. J.; Gardas, R. L.; Marrucho, I. M.; Santos, L. M. N. B. F.; Coutinho, J. a. A. P. Mutual Solubilities of Water and the [Cnmim][Tf_2N] Hydrophobic Ionic Liquids. *J. Phys. Chem. B* **2008,** *112,* 1604-1610.

147. Seddon, K. R.; Stark, A.; Torres, M. Influence of Chloride, Water, and Organic Solvents on the Physical Properties of Ionic Liquids. *Pure Appl. Chem.* **2000,** *72,* 2275-2287.

148. Rodríguez, H.; Brennecke, J. F. Temperature and Composition Dependence of the Density and Viscosity of Binary Mixtures of Water + Ionic Liquid. *J. Chem. Eng. Data* **2006,** *51,* 2145-2155.

149. Feng, S.; Voth, G. A. Molecular Dynamics Simulations of Imidazolium-based Ionic Liquid/water Mixtures: Alkyl Side Chain Length and Anion Effects. *FFE* **2010,** *294,* 148-156.

150. Kohno, Y.; Ohno, H. Ionic Liquid/water Mixtures: From Hostility to Conciliation. *Chem. Commun.* **2012,** *48,* 7119-7130.

151. Goodrich, B. F.; de la Fuente, J. C.; Gurkan, B. E.; Lopez, Z. K.; Price, E. A.; Huang, Y.; Brennecke, J. F. Effect of Water and Temperature on Absorption of CO_2 by Amine-Functionalized Anion-Tethered Ionic Liquids. *J. Phys. Chem. B* **2011,** *115,* 9140-9150.

152. Seo, S.; DeSilva, M. A.; Brennecke, J. F. Physical Properties and CO_2 Reaction Pathway of 1-Ethyl-3-Methylimidazolium Ionic Liquids with Aprotic Heterocyclic Anions. *J. Phys. Chem. B* **2014,** *118,* 14870-14879.

153. Hanke, C.; Lynden-Bell, R. A Simulation Study of Water-dialkylimidazolium Ionic Liquid Mixtures. *J. Phys. Chem. B* **2003,** *107,* 10873-10878.

154. Bhargava, B.; Yasaka, Y.; Klein, M. L. Computational Studies of Room Temperature Ionic Liquid-Water Mixtures. *Chem. Commun.* **2011,** *47,* 6228-6241.

155. Thompson, R. L.; Shi, W.; Albenze, E.; Kusuma, V. A.; Hopkinson, D.; Damodaran, K.; Lee, A. S.; Kitchin, J. R.; Luebke, D. R.; Nulwala, H. Probing the Effect of Electron Donation on CO_2 Absorbing 1,2,3-Triazolide Ionic Liquids. *RSC Advances* **2014,** *4,* 12748-12755.

156. Jiang, W.; Wang, Y.; Voth, G. A. Molecular Dynamics Simulation of Nanostructural Organization in Ionic Liquid/Water Mixtures. *J. Phys. Chem. B* **2007,** *111,* 4812-4818.

157. Chang, T. M.; Dang, L. X.; Devanathan, R.; Dupuis, M. Structure and Dynamics of N,N-Diethyl-N-methylammonium Triflate Ionic Liquid, Neat and with Water, from Molecular Dynamics Simulations. *J. Phys. Chem. A* **2010,** *114,* 12764-12774.

158. Moreno, M.; Castiglione, F.; Mele, A.; Pasqui, C.; Raos, G. Interaction of Water with the Model Ionic Liquid [bmim][BF_4]: Molecular Dynamics Simulations and Comparison with NMR Data. *J. Phys. Chem. B* **2008,** *112,* 7826-7836.

159. Porter, A. R.; Liem, S. Y.; Popelier, P. L. Room Temperature Ionic Liquids Containing Low Water Concentrations-A Molecular Dynamics Study. *Phys. Chem. Chem. Phys.* **2008,** *10,* 4240-4248.

160. Méndez-Morales, T.; Carrete, J.; Cabeza, O.; Gallego, L. J.; Varela, L. M. Molecular Dynamics Simulation of the Structure and Dynamics of Water-1-Alkyl-3-methylimidazolium Ionic Liquid Mixtures. *J. Phys. Chem. B* **2011,** *115,* 6995-7008.

161. Terranova, Z. L.; Corcelli, S. A. Molecular Dynamics Investigation of the Vibrational Spectroscopy of Isolated Water in an Ionic Liquid. *J. Phys. Chem. B* **2014,** *118,* 8264-8272.

162. Sheridan, Q. R.; Schneider, W. F.; Maginn, E. J. Anion Dependent Dynamics and Water Solubility Explained by Hydrogen Bonding Interactions in Mixtures of Water and Aprotic Heterocyclic Anion Ionic Liquids. *J. Phys. Chem. B* **2016,** *120,* 12679-12686.

163. Scammells, P. J.; Scott, J. L.; Singer, R. D. Ionic Liquids: The Neglected Issues. *Aust. J. Chem.* **2005,** *58,* 155-169.

164. Gathergood, N.; Garcia, M. T.; Scammells, P. J. Biodegradable Ionic Liquids: Part I. Concept, Preliminary Targets and Evaluation. *Green Chem.* **2004,** *6,* 166-175.

165. García Ramón, M. T.; Gathergood, N.; Scammells, P. J. Biodegradable Ionic Liquids. Part II: Effect of the Anion and Toxicology. *Green Chem.* **2005,** .

166. Wells, A. S.; Coombe, V. T. On the Freshwater Ecotoxicity and Biodegradation Properties of Some Common Ionic Liquids. *Org. Process Res. Dev.* **2006,** *10,* 794-798.

167. Matzke, M.; Stolte, S.; Thiele, K.; Juffernholz, T.; Arning, J.; Ranke, J.; Welz-Biermann, U.; Jastorff, B. The Influence of Anion Species on the Toxicity of 1-Alkyl-3-methylimidazolium Ionic Liquids Observed in an (Eco) Toxicological Test Battery. *Green Chemistry* **2007,** *9,* 1198-1207.

168. Docherty, K. M.; Dixon, J. K.; Kulpa, C. F. Biodegradability of Imidazolium and Pyridinium Ionic Liquids by an Activated Sludge Microbial Community. *Biodegradation* **2007,** *18,* 481-493.

169. Harjani, J. R.; Farrell, J.; Garcia, M. T.; Singer, R. D.; Scammells, P. J. Further Investigation of the Biodegradability of Imidazolium Ionic Liquids. *Green Chem.* **2009,** *11,* 821-829.

170. Coleman, D.; Gathergood, N. Biodegradation Studies of Ionic Liquids. *Chem. Soc. Rev.* **2010,** *39,* 600-637.

171. Zhang, C.; Wang, H.; Malhotra, S.; Dodge, C.; Francis, A. Biodegradation of Pyridinium-based Ionic Liquids by an Axenic Culture of Soil Corynebacteria. *Green Chem.* **2010,** *12,* 851-858.

172. Couling, D. J.; Bernot, R. J.; Docherty, K. M.; Dixon, J. K.; Maginn, E. J. Assessing the Factors Responsible for Ionic Liquid Toxicity to Aquatic Organisms via Quantitative Structure-property Relationship Modeling. *Green Chem.* **2006,** *8,* 82-90.

173. Zhao, D.; Liao, Y.; Zhang, Z. Toxicity of Ionic Liquids. *Clean-Soil, Air, Water* **2007,** *35,* 42-48.

174. Pham, T. P. T.; Cho, C.; Yun, Y. Environmental Fate and Toxicity of Ionic Liquids: A Review. *Water Res.* **2010,** *44,* 352-372.

175. Frade, R. F. M.; Afonso, C. A. M. Impact of Ionic Liquids in Environment and Humans: An Overview. *Hum. Exp. Toxicol.* **2010,** *29,* 1038-1054.

176. Klähn, M.; Zacharias, M. Transformations in Plasma Membranes of Cancerous Cells and Resulting Consequences for Cation Insertion Studied with Molecular Dynamics. *Phys. Chem. Chem. Phys.* **2013,** *15,* 14427-14441.

177. Bingham, R. J.; Ballone, P. Computational Study of Room-temperature Ionic Liquids Interacting with a POPC Phospholipid Bilayer. *J. Phys. Chem. B* **2012,** *116,* 11205-11216.

178. Yoo, B.; Jing, B.; Jones, S. E.; Lamberti, G. A.; Zhu, Y.; Shah, J. K.; Maginn, E. J. Molecular Mechanisms of Ionic Liquid Cytotoxicity Probed by an Integrated Experimental and Computational Approach. *Sci. Rep.* **2016,** *6,*.

179. Wang, J.; Wang, W.; Kollman, P. A.; Case, D. A. Automatic Atom Type and Bond Type Perception in Molecular Mechanical Calculations. *J. Mol. Graphics Modell.* **2006,** *25,* 247-260.

180. Wang, J.; Wolf, R. M.; Caldwell, J. W.; Kollman, P. A.; Case, D. A. Development and Testing of a General Amber Force Field. *J. Comp. Chem.* **2004,** *25,* 1157-1174.

181. Sprenger, K. G.; Jaeger, V. W.; Pfaendtner, J. The General AMBER Force Field (GAFF) Can Accurately Predict Thermodynamic and Transport Properties of Many Ionic Liquids. *J. Phys. Chem. B* **2015,** *119,* 5882-5895.

182. Bayly, C. I.; Cieplak, P.; Cornell, W.; Kollman, P. A. A Well-behaved Electrostatic Potential Based Method Using Charge Restraints for Deriving Atomic Charges: The RESP Model. *J. Phys. Chem.* **1993,** *97,* 10269-10280.

183. Frisch, M. J.; Trucks, G. W.; Schlegel, H. B.; Scuseria, G. E.; Robb, M. A.; Cheeseman, J. R.; Scalmani, G.; Barone, V.; Mennucci, B.; Petersson, G. A.; *et. al.*, "Gaussian09 Revision E.01", Gaussian Inc. Wallingford CT 2009.

184. Besler, B. H.; Merz, K. M.; Kollman, P. A. Atomic Charges Derived from Semiempirical Methods. *J. Comput. Chem.* **1990,** *11,* 431-439.

185. Singh, U. C.; Kollman, P. A. An Approach to Computing Electrostatic Charges for Molecules. *J. Comput. Chem.* **1984,** *5,* 129-145.

186. Youngs, T. G. A.; Hardacre, C. Application of Static Charge Transfer within an Ionic-Liquid Force Field and Its Effect on Structure and Dynamics. *ChemPhysChem* **2008,** *9,* 1548-1558.

187. Bhargava, B. L.; Balasubramanian, S. Refined Potential Model for Atomistic Simulations of Ionic Liquid [bmim][PF_6]. *J. Chem. Phys.* **2007,** *127,* 114510-114510.

188. Schroder, C. Comparing Reduced Partial Charge Models with Polarizable Simulations of Ionic Liquids. *Phys. Chem. Chem. Phys.* **2012,** *14,* 3089-3102.

189. Huddleston, J. G.; Visser, A. E.; Reichert, W. M.; Willauer, H. D.; Broker, G. A.; Rogers, R. D. Characterization and Comparison of Hydrophilic and Hydrophobic Room Temperature Ionic Liquids Incorporating the Imidazolium Cation. *Green Chem.* **2001,** *3,* 156-164.

190. Gómez, E.; González, B.; Domínguez, Á.; Tojo, E.; Tojo, J. Dynamic Viscosities of a Series of 1-Alkyl-3-methylimidazolium Chloride Ionic Liquids and Their Binary Mixtures with Water at Several Temperatures. *J.Chem.Eng. Data* **2006,** *51,* 696-701.

191. Jacquemin, J.; Husson, P.; Padua, A. A. H.; Majer, V. Density and Viscosity of Several Pure and Water-saturated Ionic Liquids. *Green Chem.* **2006,** *8,* 172-180.

192. Khan, I.; Kurnia, K. A.; Mutelet, F.; Pinho, S. P.; Coutinho, J. A. P. Probing the Interactions between Ionic Liquids and Water: Experimental and Quantum Chemical Approach. *J. Phys. Chem. B* **2014,** *118,* 1848-1860.

193. Cammarata, L.; Kazarian, S. G.; Salter, P. A.; Welton, T. Molecular States of Water in Room Temperature Ionic Liquids. *Phys. Chem. Chem. Phys.* **2001,** *3,* 5192-5200.

194. Berendsen, H. J. C.; van der Spoel, D.; Drunen, R. V. Gromacs: A Message-passing Parallel Molecular Dynamics Implementation. *Comp. Phys. Comm.* **1995,** *91,* 43-56.

195. Hess, B.; Kutzner, C.; van der Spoel, D.; Lindahl, E. GROMACS 4: Algorithms for Highly Efficient, Load-Balanced, and Scalable Molecular Simulation. *J. Chem. Theory Comput.* **2008,** *4,* 435-447.

196. Pronk, S.; Páll, S.; Schulz, R.; Larsson, P.; Bjelkmar, P.; Apostolov, R.; Shirts, M. R.; Smith, J. C.; Kasson, P. M.; van der Spoel, D.; *et al.*,. *Bioinformatics* **2013,** *29,* 845-854.

197. Darden, T.; York, D.; Pedersen, L. Particle Mesh Ewald: An Nlog(N) Method for Ewald Sums in Large Systems. *J. Chem. Phys.* **1993,** *98,* 10089-10092.

198. Martínez, L.; Andrade, R.; Birgin, E. G.; Martínez, J. M. PACKMOL: A Package for Building Initial Configurations for Molecular Dynamics Simulations. *J. Comput. Chem.* **2009,** *30,* 2157-2164.

199. Berendsen, H. J. C.; Postma, J. P. M.; van Gunsteren, W. F.; DiNola, A.; Haak, J. R. Molecular Dynamics with Coupling to an External Bath. *J. Chem. Phys.* **1984,** *81,* 3684-3690.

200. Nosé, S. A Unified Formulation of the Constant Temperature Molecular Dynamics Methods. *J. Chem. Phys.* **1984,** *81,* 511-519.

201. Hoover, W. G. Canonical Dynamics: Equilibrium Phase-space Distributions. *Phys. Rev. A* **1985,** *31,* 1695-1697.

202. Parrinello, M.; Rahman, A. Polymorphic Transitions in Single Crystals: A New Molecular Dynamics Method. *J. Appl. Phys.* **1981,** *52,* 7182-7190.

203. Hess, B.; Bekker, H.; Berendsen, H. J. C.; Fraaije, J. G. E. M. LINCS: A Linear Constraint Solver for Molecular Simulations. *J. Comput. Chem.* **1997,** *18,* 1463-1472.

204. Hunt, P. A.; Ashworth, C. R.; Matthews, R. P. Hydrogen Bonding in Ionic Liquids. *Chem. Soc. Rev.* **2015,** *44,* 1257-1288.

205. Dong, K.; Song, Y.; Liu, X.; Cheng, W.; Yao, X.; Zhang, S. Understanding Structures and Hydrogen Bonds of Ionic Liquids at the Electronic Level. *J. Phys. Chem. B* **2012,** *116,* 1007-1017.

206. Dong, K.; Zhang, S. Hydrogen Bonds: A Structural Insight into Ionic Liquids. *Chem. Eur. J.* **2012,** *18,* 2748-2761.

207. Izgorodina, E. I.; MacFarlane, D. R. Nature of Hydrogen Bonding in Charged Hydrogen-bonded Complexes and Imidazolium-based Ionic Liquids. *J. Phys. Chem. B* **2011,** *115,* 14659–14667.

208. Matthews, R. P.; Welton, T.; Hunt, P. A. Hydrogen Bonding and π–π Interactions in Imidazolium-chloride Ionic Liquid Clusters. *Phys. Chem. Chem. Phys.* **2015,** *17,* 14437–14453.

209. Zhang, Q.; Wang, N.; Yu, Z. The Hydrogen Bonding Interactions between the Ionic Liquid 1-Ethyl-3-Methylimidazolium Ethyl Sulfate and Water. *J. Phys. Chem. B* **2010,** *114,* 4747-4754.

210. Yoshimura, Y.; Takekiyo, T.; Okamoto, C.; Hatano, N.; Abe, H. Switching of Hydrogen Bonds of Water in Ionic liquid, 1-Butyl-3-methylimidazolium Tetrafluoroborate. *J. Raman Spectrosc.* **2013,** *44,* 475-480.

211. Torshin, I. Y.; Weber, I. T.; Harrison, R. W. Geometric Criteria of Hydrogen Bonds in Proteins and Identification of "Bifurcated" Hydrogen Bonds. *Protein Eng.* **2002,** *15,* 359-363.

212. Chowdhuri, S.; Chandra, A. Hydrogen Bonds in Aqueous Electrolyte Solutions: Statistics and Dynamics Based on Both Geometric and Energetic Criteria. *Phys. Rev. E* **2002,** *66,* 41203-41209.

213. Christ, C. D.; Mark, A. E.; van Gunsteren, W. F. Basic Ingredients of Free Energy Calculations: A Review. *J. Comput. Chem.* **2010,** *31,* 1569-1582.

214. Shirts, M. R.; Mobley, D. L. An Introduction to Best Practices in Free Energy Calculations. In *Biomolecular Simulations*, Vol. 924; Monticelli, L.; Salonen, E., Eds.; Humana Press: 2013.

215. Zhang, Y.; Maginn, E. J. Direct Correlation between Ionic Liquid Transport Properties and Ion Pair Lifetimes: A Molecular Dynamics Study. *J. Phys. Chem. Lett.* **2015,** *6,* 700-705.

216. Bodo, E.; Gontrani, L.; Caminiti, R.; Plechkova, N. V.; Seddon, K. R.; Triolo, A. Structural Properties of 1-Alkyl-3-methylimidazolium Bis(trifluoromethyl)sulfonylamide Ionic Liquids: X-ray Diffraction Data and Molecular Dynamics Simulations. *J. Phys. Chem. B* **2010,** *114,* 16398-16407.

217. Kashyap, H. K.; Santos, C. S.; Murthy, N. S.; Hettige, J. J.; Kerr, K.; Ramati, S.; Gwon, J.; Gohdo, M.; Lall-Ramnarine, S. I.; Wishart, J. F.; *et al.*, Structure of 1-Alkyl-1-methylpyrrolidinium Bis(trifluoromethylsulfonyl)amide Ionic Liquids with Linear, Branched, and Cyclic Alkyl Groups. *J. Phys. Chem. B* **2013,** *117,* 15328-15337.

218. Dhungana, K. B.; Faria, L. F. O.; Wu, B.; Liang, M.; Ribeiro, M. C. C.; Margulis, C. J.; Castner Jr., E. W. Structure of Cyano-anion Ionic Liquids: X-ray Scattering and Simulations. *J. Chem. Phys.* **2016,** *145,* 024503.

219. Santos, C. S.; Murthy, N. S.; Baker, G. A.; Castner Jr., E. W. Communication: X-ray Scattering from Ionic Liquids with Pyrrolidinium Cations. *J. Chem. Phys.* **2011,** *134,* 121101.

220. Fujii, K.; Kanzaki, R.; Takamuku, T.; Kameda, Y.; Kohara, S.; Kanakubo, M.; Shibayama, M.; Ishiguro, S.; Umebayashi, Y. Experimental Evidences for

Molecular Origin of Low-Q Peak in Neutron/x-ray Scattering of 1-Alkyl-3-methylimidazolium Bis(trifluoromethanesulfonyl)amide Ionic Liquids. *J. Chem. Phys.* **2011,** *135,* 244502.

221. Russina, O.; Triolo, A. New Experimental Evidence Supporting the Mesoscopic Segregation Model in Room Temperature Ionic Liquids. *Faraday Discuss.* **2012,** *154,* 97-109.

222. Russina, O.; Triolo, A.; Gontrani, L.; Caminiti, R. Mesoscopic Structural Heterogeneities in Room-Temperature Ionic Liquids. *J. Phys. Chem. Lett.* **2012,** *3,* 27-33.

223. Hayes, R.; Warr, G. G.; Atkin, R. Structure and Nanostructure in Ionic Liquids. *Chemical Reviews* **2015,** *115,* 6357-6426.

224. Urahata, S. M.; Ribeiro, M. C. C. Structure of Ionic Liquids of 1-Alkyl-3-methylimidazolium Cations: A Systematic Computer Simulation Study. *J. Chem. Phys.* **2004,** *120,* 1855-1863.

225. Canongia Lopes, J. N. A.; Pádua, A. A. H. Nanostructural Organization in Ionic Liquids. *J. Phys. Chem. B* **2006,** *110,* 3330-3335.

226. Atkin, R.; Warr, G. G. The Smallest Amphiphiles: Nanostructure in Protic Room-Temperature Ionic Liquids with Short Alkyl Groups. *J. Phys. Chem. B* **2008,** *112,* 4164-4166.

227. Weingärtner, H. Understanding Ionic Liquids at the Molecular Level: Facts, Problems, and Controversies. *Ang. Chem. Int. Ed.* **2008,** *47,* 654-670.

228. Russina, O.; Triolo, A.; Gontrani, L.; Caminiti, R.; Xiao, D.; Hines, L. G.; Bartsch, R. A.; Quitevis, E. L.; Pleckhova, N.; Seddon, K. R. Morphology and Intermolecular Dynamics of 1-Alkyl-3-methylimidazolium Bis(trifluoromethane)sulfonylamide Ionic Liquids: Structural and Dynamic Evidence of Nanoscale Segregation. *J. Phys.: Condens. Matter* **2009,** *21,* 424121.

229. Hayes, R.; Imberti, S.; Warr, G. G.; Atkin, R. Pronounced Sponge-like Nanostructure in Propylammonium Nitrate. *Phys. Chem. Chem. Phys.* **2011,** *13,* 13544-13551.

230. Hettige, J. J.; Kashyap, H. K.; Margulis, C. J. Communication: Anomalous Temperature Dependence of the Intermediate Range Order in Phosphonium Ionic Liquids. *J. Chem. Phys.* **2014,** *140,* 111102.

231. Araque, J. C.; Hettige, J. J.; Margulis, C. J. Modern Room Temperature Ionic Liquids, A Simple Guide to Understanding Their Structure and How It May Relate to Dynamics. *J. Phys. Chem. B* **2015,** *119,* 12727-12740.

232. Hettige, J. J.; Kashyap, H. K.; Annapureddy, H. V. R.; Margulis, C. J. Anions, the Reporters of Structure in Ionic Liquids. *J. Phys. Chem. Lett.* **2013,** *4,* 105-110.

233. Kashyap, H. K.; Santos, C. S.; Daly, R. P.; Hettige, J. J.; Murthy, N. S.; Shirota, H.; Castner Jr., E. W.; Margulis, C. J. How Does the Ionic Liquid Organizational Landscape Change when Nonpolar Cationic Alkyl Groups Are Replaced by Polar Isoelectronic Diethers? *J. Phys. Chem. B* **2013,** *117,* 1130-1135.

234. Kashyap, H. K.; Hettige, J. J.; Annapureddy, H. V. R.; Margulis, C. J. SAXS Anti-peaks Reveal the Length-scales of Dual Positive-negative and Polar-apolar Ordering in Room-temperature Ionic Liquids. *Chem. Commun.* **2012,** *48,* 5103-5105.

235. Santos, C. S.; Annapureddy, H. V. R.; Murthy, N. S.; Kashyap, H. K.; Castner Jr., E. W.; Margulis, C. J. Temperature-dependent Structure of Methyltributylammonium Bis(trifluoromethylsulfonyl)amide: X ray Scattering and Simulations. *J. Chem. Phys.* **2011,** *134,*.

236. Hettige, J. J.; Araque, J. C.; Margulis, C. J. Bicontinuity and Multiple Length Scale Ordering in Triphilic Hydrogen-Bonding Ionic Liquids. *J. Phys. Chem. B* **2014,** *118,* 12706-12716.

237. Hammersley, A. P.; Svensson, S. O.; Hanfland, M.; Fitch, A. N.; Hausermann, D. Two-dimensional Detector Software: From Real Detector to Idealised Image or Two-theta Scan. *High Pressure Res.* **1996,** *14,* 235-248.

238. Hammersley, A. "FIT2D V10.3 Reference Manual V4.0", European Synchrotron Radiation Facility: 1998,.

239. Brown, P. J.; Fox, A. G.; Maslen, E. N.; O'Keefe, M. A.; Willis, B. T. M. *International Tables for Crystallography* **2006,** *C,* 554-595.

240. Qiu, X.; Thompson, J. W.; Billinge, S. J. L. *PDFgetX2*: A GUI-driven Program to Obtain the Pair Distribution Function from X-ray Powder Diffraction Data. *J. Appl. Crystallogr.* **2004,** *37,* 678.

241. Hockney, R. W. Methods in Computational Physics. In ; 1970; Chapter 9, page 136.

242. Potter, D. Computational Physics. In ; Wiley: New York,.

243. Allen, M. P.; Tildesley, D. J. Computer Simulations of Liquids. In ; Oxford University Press: Great Clarendon Street, Oxford, 1987.

244. Luo, X.; Guo, Y.; Ding, F.; Zhao, H.; Cui, G.; Li, H.; Wang, C. Significant Improvements in CO_2 Capture by Pyridine-Containing Anion-Functionalized

Ionic Liquids through Multiple-Site Cooperative Interactions. *Ang. Chem. Int. Ed.* **2014,** *53,* 7053-7057.

245. Zhao, Y.; Zhang, X.; Zhen, Y.; Dong, H.; Zhao, G.; Zeng, S.; Tian, X.; Zhang, S. Novel Alcamines Ionic Liquids Based Solvents: Preparation, Characterization and Applications in Carbon Dioxide Capture. *Int. J. Greenhouse Gas Control* **2011,** *5,* 367-373.

246. Plechkova, N. V.; Seddon, K. R. Applications of Ionic Liquids in the Chemical Industry. *Chem. Soc. Rev.* **2008,** *37,* 123-150.

247. Urukova, I.; Vorholz, J.; Maurer, G. Solubility of CO_2, CO, and H_2 in the Ionic Liquid [bmim][PF_6] from Monte Carlo Simulations. *J. Phys. Chem. B* **2005,** *109,* 12154-12159.

248. Klamt, A.; Jonas, V. Treatment of the Outlying Charge in Continuum Solvation Models. *J. Chem. Phys.* **1996,** *105,* 9972-9981.

249. Roux, B.; Simonson, T. Implicit Solvent Models. *Biophys. Chem.* **1999,** *78,* 1-20.

250. Baker, N. A. Improving Implicit Solvent Simulations: A Poisson-centric View. *Curr. Opin. Struct. Biol.* **2005,** *15,* 137-143.

251. Eilmes, A.; Kubisiak, P. Explicit Solvent Modeling of Solvatochromic Probes in Ionic Liquids: Implications of Solvation Shell Structure. *J. Phys. Chem. B* **2015,** *119,* 13185-13197.

252. Dissanayake, D. P.; Senthilnithy, R. Thermodynamic Cycle for the Calculation of Ab Initio pKa Values for Hydroxamic Acids. *J. Mol. Struct.* **2009,** *910,* 93-98.

253. Sutton, C. C. R.; Franks, G. V.; da Silva, G. First Principles pKa Calculations on Carboxylic Acids Using the SMD Solvation Model: Effect of Thermodynamic Cycle, Model Chemistry, and Explicit Solvent Molecules. *J. Phys. Chem. B* **2012,** *116,* 11999-12006.

254. Guerard, J. J.; Tentscher, P. R.; Seijo, M.; Samuel Arey, J. Explicit Solvent Simulations of the Aqueous Oxidation Potential and Reorganization Energy for Neutral Molecules: Gas Phase, Linear Solvent Response, and Non-linear Response Contributions. *Phys. Chem. Chem. Phys.* **2015,** *17,* 14811-14826.

255. Brown, P.; Gurkan, B. E.; Hatton, T. A. Enhanced Gravimetric CO_2 Capacity and Viscosity for Ionic Liquids with Cyanopyrrolide Anion. *AIChE J.* **2015,** *61,* 2280-2285.

256. Kelkar, M. S.; Maginn, E. J. Calculating the Enthalpy of Vaporization for Ionic Liquid Clusters. *J. Phys. Chem. B* **2007,** *111,* 9424-9427.

257. Verevkin, S. P.; Zaitsau, D. H.; Emel'yanenko, V. N.; Schick, C.; Jayaraman, S.; Maginn, E. J. An Elegant Access to Formation and Vaporization Enthalpies of Ionic Liquids by Indirect DSC Experiment and "In Silico" Calculations. *Chem. Commun.* **2012,** *48,* 6915-6917.

258. Köddermann, T.; Paschek, D.; Ludwig, R. Ionic Liquids: Dissecting the Enthalpies of Vaporization. *ChemPhysChem* **2008,** *9,* 549-555.

259. Wang, J.; Hou, T. Application of Molecular Dynamics Simulations in Molecular Property Prediction. 1. Density and Heat of Vaporization. *J. Chem. Theory. Comput.* **2011,** *7,* 2151-2165.

260. McQuarrie, D. *Statistical Mechanics;* Harper & Row: 1975.

261. Cramer, J. C. Essentials of Computational Chemistry Theories and Models Second Edition. In ; Wiley: The Atrium, Southern Gate, Chichester, West Sussex PO19 8SQ, England, 2004; Chapter Thermodynamic Properties.

262. Timko, J.; Bucher, D.; Kuyucak, S. Dissociation of NaCl in Water from Ab Initio Molecular Dynamics Simulations. *J. Chem. Phys.* **2010,** *132,* 114510.

263. Timko, J.; De Castro, A.; Kuyucak, S. Ab Initio Calculation of the Potential of Mean Force for Dissociation of Aqueous Ca-Cl. *J. Chem. Phys.* **2011,** *134,* 204510.

264. Car, R.; Parrinello, M. Unified Approach for Molecular Dynamics and Density-Functional Theory. *Phys. Rev. Lett.* **1985,** *55,* 2471-2474.

265. Schróder, Bernd, C. J. A. P. Predicting Enthalpies of Vaporization of Aprotic Ionic Liquids with COSMO-RS. *Fluid Phase Equilib.* **2014,** *370,* 24-33.

266. Gurkan, B. E.; Juan, C.; Mindrup, E. M.; Ficke, L. E.; Goodrich, B. F.; Price, E. A.; Schneider, W. F.; Maginn, E. J.; Brennecke, J. F. Chemically Complexing Ionic Liquids for Post-combustion CO_2 Capture. In *Clearwater Clean Coal Conference*; 2010.

This document was prepared & typeset with pdfLaTeX*, and formatted with* NDdiss2$_\varepsilon$ *classfile (v3.2013[2013/04/16]) provided by Sameer Vijay and updated by Megan Patnott.*